Summer 8-15-2015

Solid-State NMR Studies of Carbon Capture and Carbon Mineralization Reactions

Jeremy Moore
Washington University in St. Louis

WASHINGTON UNIVERSITY IN ST. LOUIS

Department of Chemistry

Dissertation Examination Committee:
Sophia E. Hayes, Chair
Joseph Ackerman
Mark S. Conradi
Daniel E. Giammar
Kevin D. Moeller

Solid-State NMR Studies of Carbon Capture and Carbon Mineralization Reactions

by

Jeremy Kent Moore

A dissertation presented to the
Graduate School of Arts & Sciences
of Washington University in
partial fulfillment of the
requirements for the degree
of Doctor of Philosophy

August 2015
St. Louis, Missouri

Table of Contents

List of Figures iv
List of Tables viii
Acknowledgments ix
ABSTRACT OF THE DISSERTATION xiii
Chapter 1: Introduction 1
1.1 Carbon Capture 1
1.1.1 Physisorption of CO_2 3
1.1.2 Chemisorption of CO_2 3
1.2 Carbon Sequestration 4
1.3 Nuclear Magnetic Resonance (NMR) Spectroscopy 4
Chapter 2: Experimental Methods 13
2.1 NMR Pulse Sequences 13
2.1.1 Pulse and Acquire 13
2.1.2 Hahn Echo 15
2.1.3 Cross Polarization Magic Angle Spinning (CPMAS) 17
2.2 NMR Spectrum Fitting 20
2.3 NMR Probe Hardware 20
2.4 Polymers of Intrinsic Microporosity (PIMs) 21
2.5 Supported Amine Adsorbents 22
2.6 Carbon Mineralization Materials 23
Chapter 3: Carbon Capture 24
3.1 Physisorption Studies 25
3.1.1 Introduction to Polymers of Intrinsic Microporosity (PIMs) 25
3.1.2 Tetrazole Functionalize PIM (TZPIM) 27
3.1.3 PIM-1 41
3.1.4 Methylated Tetrazole Functionalize PIM (TZPIM) 43
3.1.5 PIMs Conclusions 46
3.2 Chemisorption Studies 47
3.2.1 Supported Amine Adsorbents 47

3.2.2 Class 1: Polyethyleneimine (PEI) 50
3.2.3 Class 3: Hyperbranched Aminosilica (HAS) 54
3.2.4 Class 2: Primary, Secondary, Tertiary Amines 72
Chapter 4: Carbon Mineralization 74
4.1 Reactions of CO_2 and Forsterite (Mg_2SiO_4) 78
4.2 The Effect of Salt on Carbon Mineralization 82
4.3 The Silica-Rich Passivating Layer 84
4.4 Real Rock Systems: Choosing Systems Wisely 91
4.4.1 Anorthite ($CaAl_2Si_2O_8$) 92
4.4.2 Peridotite 94
4.4.3 Cement Powder 95
4.5 Cement Precursors 97
References 102

List of Figures

Figure 2.1 Pictorial representation of a pulse and acquire NMR pulse sequence..... 14
Figure 2.2 An example of a ^{13}C NMR nutation curve. 15
Figure 2.3 Pictorial representation of a Hahn echo pulse sequence. 16
Figure 2.4 Pictorial representation of a X{^{1}H} CPMAS NMR pulse sequence. 18
Figure 2.5 Pictorial representation of a X{^{1}H} CPMAS echo NMR pulse sequence. 19
Figure 2.6 Pictorial representation of a X{^{1}H} CPMAS dipolar dephasing NMR pulse sequence. 20
Figure 3.1 Depictions of the monomers that make the PIM adsorption materials. 26
Figure 3.2 Depiction of CO_2 adsorbed on a tetrazole group. The dashed line represents the adsorption interaction..... 27
Figure 3.3 ^{13}C NMR resonances of CO_2 adsorbed on TZPIM as compared to CO_2 gas. Both are at a pressure of 1 atm and at 295 K. Each spectrum was acquired with the same number of scans. 29
Figure 3.4 ^{13}C NMR resonances of CO_2 adsorbed on TZPIM. The spectra on the left are from the low loading sample, and the spectra on the right are from the high loading sample. Note: the top spectra have an expanded x-axis to show the narrow resonances at higher temperatures. 100 ppm = 5.08 kHz. 31
Figure 3.5 Depiction of CO_2 adsorbed on a tetrazole group with the θ that defines the librational motion of CO_2. 33
Figure 3.6 Depiction of CO_2 adsorbed on a tetrazole group with a potential translation-reorientation hop from one tetrazole group to another. 34
Figure 3.7 ^{13}C NMR linewidths of CO_2 adsorbed on TZPIM as a function of temperature. 36
Figure 3.8 ^{13}C NMR T_2 relaxation time constant for CO_2 adsorbed on TZPIM as a function of temperature. 38
Figure 3.9 ^{13}C NMR T_1 relaxation time constant for CO_2 adsorbed on TZPIM as a function of temperature. 40
Figure 3.10 Depiction of CO_2 adsorbed on a nitrile group. The dashed line represents the adsorption interaction..... 42
Figure 3.11 ^{13}C NMR resonances of CO_2 adsorbed on PIM-1. The spectra on the left are from the low loading sample, and the spectra on the right are from the high loading sample. 100 ppm = 5.08 kHz..... 43
Figure 3.12 Depiction of CO_2 adsorbed on a methylated tetrazole group. The dashed line represents the adsorption interaction. 44
Figure 3.13 ^{13}C NMR resonances of CO_2 adsorbed on MTZPIM. The spectra on the left are from the low loading sample, and the spectra on the right are from the high loading sample. 100 ppm = 5.08 kHz. 45
Figure 3.14 Representation of the three types of amine sites. 47

Figure 3.15 Depiction of the three classes of amine adsorbents. The blue rectangles represent the SBA-15 support..... 49
Figure 3.16 The reaction pathways for a primary amine and CO_2. The asterisk labels the ^{13}C enriched carbon that was introduced by the $^{13}CO_2$. The listed chemical shifts are solution state chemical shifts.[64]..... 50
Figure 3.17 Static ^{13}C *in situ* NMR at 7 T of SBA-15-PEI reacted with $^{13}CO_2$(g)..... 51
Figure 3.18 ^{13}C NMR T_1 relaxation time constant for the CO_2 adsorption product from reaction with SBA-15-PEI..... 52
Figure 3.19 ^{13}C NMR peak width measured by the FWHM for the CO_2 adsorption product from reaction with SBA-15-PEI..... 53
Figure 3.20 $^{13}C\{^1H\}$ CPMAS NMR recorded *ex situ* at 7 T of reacted SBA-15-PEI solids collected from the *in situ* reactor. (Sample rotation, ν_R= 5 kHz)..... 54
Figure 3.21 A) Static ^{13}C *in situ* NMR at 14 T of SBA-15-HAS reacted with $^{13}CO_2$(g) for 2 hours. B) Expanded scale showing the chemisorbed feature..... 55
Figure 3.22 $^{13}C\{^1H\}$ CPMAS NMR recorded *ex situ* at 14 T of reacted SBA-15-HAS solids collected from the *in situ* reactor. (Sample rotation, ν_R= 10 kHz)..... 56
Figure 3.23 Cross-polarization Hahn spin echo measurements of T_2 (spin-spin) relaxation time curve of the resonance at 164.3 ppm in the $^{13}CO_2$ reacted SBA-15-HAS sample. Lines are fits of two possible linear relaxation regimes with T_2 relaxation times of 14.7 ms and 76.9 ms..... 58
Figure 3.24 ^1H MAS NMR spectra at 7 T of $^{13}CO_2$ reacted SBA-15-HAS. The black curve shows a dry reaction environment and the red curve shows a wet reaction environment. Both spectra were spinning near 5 kHz, though the spinning sidebands are notably offset indicating a small difference in spinning speed..... 59
Figure 3.25 $^{13}C\{^1H\}$ CPMAS NMR recorded *ex situ* at 7 T of reacted SBA-15-HAS solids collected from the *in situ* reactor. The black curve shows a dry reaction environment and the red curve shows a wet reaction environment..... 60
Figure 3.26 $^{13}C\{^1H\}$ CPMAS NMR contact time curve of the dry CO_2 and amine reaction (top) and wet CO_2 and amine reaction (bottom)..... 61
Figure 3.27 $^{13}C\{^1H\}$ CPMAS NMR interrupted decoupling experiment of the dry CO_2 and amine reaction (top) and wet CO_2 and amine reaction (bottom)..... 62
Figure 3.28 $^{13}C\{^1H\}$ CPMAS NMR (ν_R= 3.8 kHz) at 3 T of the single carbon site in ammonium carbamate (NH_4)(H_2NCO_2), showing the splitting and the characteristic peak ratio of the resonance due to ^{13}C-^{14}N dipolar coupling. The experimental spectrum is in black, and the fits of both peaks are in red..... 66
Figure 3.29 $^{13}C\{^1H\}$ CPMAS NMR (ν_R= 3.8 kHz) at 3 T of the reacted SBA-15-HAS. The chemisorbed product resonance has a FWHM of ~5.2 ppm. 1024 transients were recorded..... 66
Figure 3.30 $^{13}C\{^1H\}$ CPMAS NMR at 3 T of the reacted SBA-15-HAS after evacuating the reacted sample for 31 hours. 72,000 transients were recorded (ν_R= 3.8 kHz). The experimental spectrum is in black (top), the overall fit (bottom) is in black, the peak fits for carbamate are blue, and the peak fit for bicarbonate is red..... 68

Figure 3.31 $^{13}C\{^{1}H\}$ CPMAS NMR at 2.35 T $^{13}CO_2$ reacted class 2 adsorbents supported on SBA-15. (ν_R= 4.5 kHz). APS with primary amine is on the left and MAPS with secondary amines is on the right. 72
Figure 4.1 Phase diagram for CO_2. (Source: http://chemwiki.ucdavis.edu/Textbook_Maps/General_Chemistry_Textbook_Maps/Map%3A_Lower's_Chem1/07%3A_Solids_and_Liquids/7.5%3A_Changes_of_State#Phase_map_of_Carbon_dioxide) 76
Figure 4.2 Representation of the *in situ* NMR apparatus..... 77
Figure 4.3 Reactions of CO_2 and Forsterite 78
Figure 4.4 Ternary phase diagram for the composition of magnesium containing minerals separated by the amount of MgO, CO_2, and H_2O in the structure. 79
Figure 4.5 *In situ* static ^{13}C NMR at 8.2 T of a forsterite in water reaction with CO_2. Reaction at conditions of 80 ^{o}C and 95 atm CO_2. Each spectrum is at the time point listed in the key. 80
Figure 4.6 *Ex situ* ^{13}C MAS NMR of slices from the collected, dried forsterite and CO_2 reaction. The top of the reaction vessel is labelled as 0 cm and the depth goes "down into" the vessel..... 81
Figure 4.7 *In situ* static ^{13}C NMR spectra at 8.2 T of carbon mineralization reactions. On the left, a forsterite in water reaction with CO_2. On the right, a forsterite in brine solution reaction with CO_2. Each spectrum is at the time point listed in the key. 83
Figure 4.8 *Ex situ* ^{13}C MAS NMR of slices from the collected, dried carbon mineralization reactions. On the left, a forsterite in water and CO_2 reaction. On the right, a forsterite in brine solution and CO_2 reaction. The top of the reaction vessel is labelled as 0 cm and the depth goes "down into" the vessel. 84
Figure 4.9 Representation of amorphous silica with Q1 through Q4 sites. 85
Figure 4.10 ^{29}Si MAS NMR of a forsterite prior to reaction with CO_2. 86
Figure 4.11 ^{29}Si MAS NMR of a representative slice of the carbon mineralization reactions. The black spectrum is the reaction in water. The red spectrum is the reaction in brine. 87
Figure 4.12 $^{29}Si\{^{1}H\}$ CPMAS NMR of a representative slices of the carbon mineralization reactions. The top spectra are from the reaction in water. The bottom spectra are from the reaction in brine. Spinning speed 5 kHz. 88
Figure 4.13 ^{23}Na MAS NMR of the forsterite in brine solution reaction with CO_2. FWHM = 1.5 ppm 90
Figure 4.14 *In situ* ^{13}C NMR of CO_2 reacting with anorthite in water at 90 ^{o}C and 85 atm of CO_2. Spectrum is after 42 days of reaction. 93
Figure 4.15 *In situ* ^{13}C NMR at 8.2 T of CO_2 gas (left) at 1 atm and CO_2 with peridotite (right) at 50 atm..... 95
Figure 4.16 *In situ* ^{13}C NMR at 8.2 T of CO_2 gas (left) at 1 atm and CO_2 with cement powder (right) at 50 atm. 96
Figure 4.17 $^{13}C\{^{1}H\}$ CPMAS NMR of the cement precursors with a spinning rate of 5 kHz. Sample 1 on top. Sample 2 in the middle. Sample 3 on the bottom. The experimental data is in

black and the overall fit is in red. Fits of vaterite are in green and royal blue. Fit of calcite is in purple. Fits of bicarbonate resonances are in light blue, yellow, and black. Na-containing peak is in red. 98
Figure 4.18 ^{23}Na MAS NMR at 7 T spinning at 5 kHz. Sample 1 on the left, sample 2 in the middle, sample 3 on the right. 100

List of Tables

Table 3.1 ^{13}C NMR chemical shifts and peak widths at 3 T..... 69
Table 3.2 The ^{13}C NMR chemical shift and linewidth of class 2 amine adsorbents 73
Table 4.1 The 13C NMR chemical shift and linewidth of the cement precursor samples. 99

Acknowledgments

First, I would like to thank my wonderful wife for all of her support during my time at Washington University. She has been a constant source of encouragement and motivation that helped me get through the difficulties of graduate school. I could not have done this without her and definitely would not have enjoyed it as much.

I want to thank my parents and brothers for their support growing up and as I have continued through school. My parents have supported me in whatever I chose to do and for that I will be forever grateful. My two younger brothers continue to keep me humble, only how brothers could, and I enjoy learning about their fields as they continue to excel.

I want to thank the friends that have supported me during my graduate studies. Some have been friends for a long time and I thank you for the support. Some are friends I've made in graduate school. I thank you for the times we spent in classes, teaching, and in labs. I've learned a lot from my fellow graduate students and have many good memories of my time. I want to specifically thank the members of the Hayes and Conradi groups with whom I have spent a lot of time over the last few years. I also want to specifically mention Dr. Andy Surface, who spent time teaching me NMR and our daily conversations on CCS research, I truly appreciate our friendship.

I want to thank my advisor, Prof. Sophia Hayes, for bringing me into her research group. I have learned things about my research area but also about the other research projects in our lab, how to effectively communicate scientific ideas, and collaborating.

I want to thank Prof. Mark Conradi who served as a co-advisor during my research. I learned a lot about NMR hardware and how to attack research questions during my time with him. My

ability to build NMR probes and troubleshoot hardware issues was greatly affected by his work with me.

I thank my committee, Prof. Joe Ackerman and Prof. Kevin Moeller, for their time at my annual meetings and reading my thesis. I also thank Prof Dan Giammar for joining my defense committee and reading my thesis.

I would like to thank the Washington University in St. Louis Department of Chemistry staff for all their assistance. The support I received during coursework, teaching, and research was invaluable to my experience.

I would like to acknowledge the collaborators that I was fortunate enough to work with to complete this research. Prof. Chris Jones and his group provided all of the materials used for CO_2 chemisorption studies of amines. He and group member, Miles Sakwa-Novak, also provided insight into the materials and reactions that were invaluable to this research effort. Dr. Michael Guiver provided the PIM materials used in the CO_2 physisorption studies as well as detailed characterization of the materials and their adsorption capabilities. I was able to meet with Prof. Dan Giammar and his group member, Wei Wang, weekly to discuss the carbon mineralization experiments. I truly appreciate those meetings as it gave me the opportunity to see the research from a different perspective and apply that knowledge to the my research questions. Prof. Phil Skemer was always available to lend his expertise in geology to the carbon mineralization research.

I acknowledge all the sources of funding that I received for the work. Research was supported by a grant from Washington University in St. Louis, Consortium for Clean Coal Utilization (CCCU); by the National Science Foundation Chemical, Bioengineering, Environmental and Transport Systems (CBET) under Award # CBET-1403298; by the Center for Understanding &

Control of Acid Gas-Induced Evolution of Materials for Energy (UNCAGE-ME), an Energy Frontier Research Center (EFRC) funded by the U.S. Department of Energy (DOE), Office of Science, Basic Energy Sciences (BES), under Award # DE-SC0012577; and by the U.S. Department of Energy (DOE), National Energy Technology Laboratory (NETL) under Award # DE-FE0023382. Experiments concerning geosequestration of CO_2 were supported by CCCU and DOE NETL. Experiments that address capture of CO_2 onto hyperbranched aminosilicates were supported by NSF CBET, and those preliminary experiments that address the capture of acid gases onto materials other than HAS were supported by DOE EFRC.

I would also like to acknowledge Washington University in St. Louis for the dissertation fellowship which supported me during the writing of this dissertation.

Jeremy Moore

Washington University in St. Louis

August 2015

ABSTRACT OF THE DISSERTATION

Solid-State NMR Studies of Carbon Capture and Carbon Mineralization Reactions

by

Jeremy Kent Moore

Doctor of Philosophy in Chemistry

•

Washington University in St. Louis, 2015

Professor Sophia E. Hayes, Chair

This dissertation presents research on the chemistry of carbon dioxide capture and mineralization which has been accomplished with a variety of solid-state nuclear magnetic resonance (NMR) spectroscopy techniques. Materials used for carbon capture interact with CO_2 through different adsorption mechanisms, physisorption and chemisorption. The physisorption systems studied have shown that adsorbed CO_2 undergoes a hopping mechanism within the material. The studies of chemisorption systems indicate a mixture of adsorption products forms during the adsorption interaction. Carbon mineralization reactions have been studied to better understand the reactions that can occur at underground carbon sequestrations sites that are used for storing CO_2. Here it has been shown that NaCl affects the chemistry in these reacting systems, which can be seen with NMR. The limitations of the ability of NMR to study carbon mineralization reactions have also been investigated. This research shows that solid-state NMR is a useful tool for studying carbon capture and mineralization as well as describing the interactions of CO_2 in these systems.

Chapter 1: Introduction

The increasing awareness of negative effects of CO_2 on the environment, including effects on crop production[1] and rising global temperatures, have brought the attention of researchers and policy makers to mitigating the effects of CO_2.[2–5] A multi-faceted approach will be needed to stop and reverse the trend of rising atmospheric CO_2 concentrations which will include non-carbon containing fuel sources as well as decreasing current carbon emissions. Improving on the effects of carbon emissions will incorporate both the capture[3,6] and sequestration[7] of CO_2, which will be the focus of this thesis, and individually have multiple approaches to accomplish their goals. Carbon capture methods can be developed to remove CO_2 directly from the atmosphere or from high concentration emission sources. The storage of CO_2 can involve methods of geologic sequestration in underground rock formations that include physical trapping of the CO_2 with an impermeable cap rock layer or chemical reaction trapping of the CO_2 with reaction with the minerals in the rock formation.

The work presented within this thesis could not possibly cover all of the possible methods of CO_2 capture and sequestration. The focus of the following studies has been on two types of capture materials and on carbon sequestration through mineralization reactions. Nuclear magnetic resonance (NMR) spectroscopy is the primary research tool used in these studies and will be discussed in depth.

1.1 Carbon Capture

The capture of CO_2 is a strategy for reducing the overall concentration of carbon dioxide in the atmosphere. Research has been done into capturing CO_2 from emission sources, for example automobiles, power plants, and cement factories.[2,6] There have also been materials designed to

capture CO_2 directly from the atmosphere at atmospheric concentrations, which is currently at a level of approximately 400 ppm.[8,9] The research described within refer to materials that would likely be utilized for high concentration sources such as flue gases from power plants that burn hydrocarbon fuels though these have also been shown to have the capability to adsorb CO_2 at low atmospheric concentrations. Current technologies for carbon capture have been applied mostly to power plant emissions.[2] These designs use liquid amine absorption materials to capture CO_2 through absorption and reaction of the CO_2.[2,10] The CO_2 dissolves into the solution and chemically reacts with the amine bearing molecules. These solutions have drawbacks to their widespread use, such as chemical degradation, amine leaching, and high energy consumption for regeneration.[2] New solid adsorbents have been proposed to alleviate some of these issues and more efficiently capture CO_2. Multiple strategies have been proposed for the capture of CO_2 from the flue gas of power plants with solid sorbents. CO_2 undergoes adsorption on chemical groups in a highly porous solid which distinguishes these materials from absorption in liquid sorbents due to the added stability of the solid structure. The strategies for adsorption can be categorized by the type of interaction CO_2 has with the surface of the material, physisorption or chemisorption.

Both physisorption and chemisorption methods are capable of adsorbing CO_2 though they do have distinct characteristics. Physisorption materials tend to have a low energy to regenerate the material because minimal energy is needed to overcome the van der Waals interaction that adsorbs the CO_2. Chemisorption materials typically have a higher energy requirement to remove the CO_2 from the material, as compared to physisorption materials. Though, the selectivity of the chemisorption materials is higher since they rely on chemical reactions that are highly specific for CO_2.

1.1.1 Physisorption of CO_2

Physisorption is an adsorption process where van der Waals interactions attract CO_2 molecules to a surface. This interaction largely does not perturb the electronic structure of the adsorbed molecule, in this case CO_2. Physisorption interactions have been evidenced with CO_2 by metal-organic frameworks (MOFs)[11–13] and PIMs[14–17] which, though not exclusively, can be utilized as materials for membrane capture technologies.[14,18–22] In these membrane materials, CO_2 is separated from the rest of the flue gas by the material attracting CO_2 preferentially over the other gases. The CO_2 is "pulled" through the material while the other gases would have to rely on diffusion to get through the membrane. The flue gas flows through a pipe around the outside of the membrane material and a second pipe is on the inside of the membrane. The CO_2 travels through the membrane to the inside tube while the rest of the flue gas is blocked by the membrane, staying in the original tube. The CO_2 is then collected from the center tube as a pure gas stream. A key, then, to determine the efficiency of a physisorption membrane material is the balance between selectivity and permeability.

1.1.2 Chemisorption of CO_2

Chemisorption is an adsorption process in which CO_2 chemically reacts with the adsorbent material, converting it to another chemical species. For CO_2 capture a typical chemisorption material is amine-bearing materials. In the case of amines and CO_2, the products of these reactions are molecules such as carbamate, urea, and bicarbonate species. The current CO_2 capture technologies are liquid amine absorbents which have analogous chemical reactions. In solid amine adsorbents, the flue gas is flown through the material, and the CO_2 reacts with the surface while the rest of the gases pass through. The material is then treated to remove the CO_2 as a pure gas stream. This treatment typically includes heating the material under the conditions of an inert gas stream or vacuum.[3,23–25] The key to determine the efficiency of a chemisorption

material is the tradeoff between highly selective and more tightly bound CO_2 molecules and the extra heat needed to regenerate the capture agent to receive more CO_2.

1.2 Carbon Sequestration

After CO_2 has been captured and collected as a nearly pure CO_2 stream, the CO_2 must be stored by some method. Many ideas have been proposed but, the studies presented here focus on the sequestration methods that involve CO_2 mineralization which include underground CO_2 storage. Typical strategies for underground storage use a cap rock layer that the CO_2 is sealed beneath.[26] Under this cap rock is a water layer in which the CO_2 is pumped into, typically as a supercritical fluid. Test sites for this type of storage are underway.[27–29] Despite the pilot projects for underground sequestration, there are questions remaining about the permanence of this storage solution and possible implications of CO_2 acidifying the underground water layers.[7,30,31]

A truly permanent storage solution is to select underground storage sites that allow for possible carbon mineralization reactions that convert CO_2 into a carbonate mineral phase.[7] To have carbon mineralization occur, a mineral that can release a divalent cation (such as Mg^{2+}, Ca^{2+}, and Fe^{2+}) must be present. Possible reactants for mineralization reactions include olivine [$(Mg,Fe)_2SiO_4$], pyroxene (for example $Mg_2Si_2O_6$) and feldspar (for example $CaAl_2Si_2O_8$) minerals which contain these cations and can be used to permanently store CO_2 as a solid carbonate. Once CO_2 has been converted into a metal carbonate mineral, the storage is permanent.

1.3 Nuclear Magnetic Resonance (NMR) Spectroscopy

The NMR spectroscopy is a useful analytical technique due to its wide range of applications and is the primary tool used in this research to study carbon capture and sequestration. NMR's

ability to detect both crystalline and amorphous phases of materials gives it an advantage over other analytical techniques, such as pXRD, that are only able to characterize crystalline samples. This feature allows NMR to study multi-phase reactions such as gas/solid CO_2 capture reactions or aqueous/solid CO_2 mineralization reactions. NMR is also able to study reactions at relevant temperatures and pressures for carbon capture and sequestration reactions. This allows monitoring of the reaction at conditions other than STP. To explain how NMR is used in these studies, a technical description of the technique follows.

NMR is an analytical technique that investigates atomic nuclei by the intrinsic physical property called spin. Spin is related to the magnetic moment, μ, of a nucleus by the gyromagnetic ratio, γ. Spin and magnetic moment are collinear vector quantities which mean they are parallel vectors.

$$\hat{\mu} = \gamma \hat{I} \qquad (1.1)$$

Since both spin and the magnetic moment are intrinsic to a specific nucleus, each nucleus has a unique gyromagnetic ratio.

When a nuclear spin is placed in an external magnetic field, which will be denoted by B_o, the spin vector precesses about the external field. The frequency of this precession is proportional to the applied magnetic field.

$$\omega_o = -\gamma B_o \quad (1.2)$$

As we can see it is again the gyromagnetic ratio of the atomic nucleus that relates these quantities. The frequency, ω_o, is called the nuclear Larmor frequency. Since the gyromagnetic ratio is unique to each nucleus, the Larmor frequency is used to distinguish the spin of different

nuclei. The Larmor frequency is dependent on the strength of the applied magnetic field, such that a larger field leads to faster precession.

In quantum mechanics, the property of spin is quantized into $2I + 1$ states, where I is the spin quantum number (for ^{13}C, I=1/2). The spin states are degenerate in energy with no external magnetic field. When an external magnetic field is applied, the degeneracy is lifted and the nuclear spin states have an energy splitting, called the nuclear Zeeman splitting. A spin-1/2 system has two states, called the "spin-up" and the "spin-down" states, which refers to the spins orientation relative to the z-axis. The state that is aligned with B_o, spin-up, is the lower energy state. The spin states have a larger Zeeman splitting for increasing size of the applied magnetic field. It is this energy splitting that makes NMR a spectroscopic technique, where matter is studied via the interaction of the nuclear spin and radiofrequency waves.

$$\Delta E_{Zeeman} = \left|\bar{h}\gamma B_o\right| \quad (1.3)$$

The introduction of an external magnetic field induces both the Zeeman splitting of the quantized spin states and the precession of the spins. The Larmor frequency can thus be used to define the Zeeman energy splitting.

$$\Delta E_{Zeeman} = \left|\bar{h}\gamma B_o\right| = \left|\bar{h}\omega_o\right| \quad (1.4)$$

Thus, the difference in Zeeman energy is dependent on the nucleus and the strength of the magnetic field.

Since the energy states are quantized, the spins must exist in one of the energy states. In the absence of the external magnetic field, the spins can exist equally in the available energy states.

The application of an external magnetic field creates the Zeeman energy splitting of the spin states, in which the lower energy levels to be preferentially populated, though not exclusively.

$$\Delta population = e^{\bar{h}\gamma B_o/kT} = e^{\Delta E_{Zeeman}/kT} \quad (1.5)$$

This population difference determines the spin polarization which is used as the source for the NMR signal. When the system is at thermal equilibrium, the population difference is called the Boltzmann population, where k in the equation is the Boltzmann constant.

Nuclear spins and electrons spins induce small magnetic fields inside the sample. These small fields are "felt" by nearby spins which are summed together with B_o to determine the magnitude of the local magnetic field for each spin. Therefore, individual spins, in the same external magnetic field, experience a slightly different local magnetic field. Each spin precesses according to its local field, which means that each spin in an ensemble of spins precesses at a slightly different frequency. This small difference in precession frequency does not affect the spin polarization along the z-axis but only the spin polarization in the x-y plane. This is undetectable over a few rotations but over many rotations the spins will point in all directions of the x-y plane. NMR is sensitive to these small changes in local environment, which makes the technique such a powerful tool.

An ensemble of spins, in the absence of a magnetic field, has spins pointing in all directions and has no precessional motion. When a magnetic field is turned on suddenly, there is a time constant associated with the build-up of the spin polarization, called the spin-lattice relaxation time, T_1. This time constant describes the rate of energy transfer from the spin system to the lattice surrounding the nuclei to establish the Boltzmann population. T_1 can thus be monitored by the growth of the spin polarization along the z-axis, which restores the Boltzmann distribution

of spins. M_Z is the magnetization along the z-axis at a given time, τ, and M_Z^{∞} is the magnetization at the Boltzmann equilibrium.

$$M_Z = M_Z^{\infty}(1 - e^{\tau/T_1}) \qquad (1.6)$$

When the Boltzmann population of an ensemble of spins has been established along the axis of the external magnetic field, there is a net magnetization along that axis which we will set as the z-axis. The spins are all precessing about the z-axis and are pointing in all directions of the x-y plane such that there is no net magnetization along the x- or y- axes. If we then suddenly rotate the spins about the x-axis, the spins will have a net magnetization on the y-axis but no net magnetization in the x-z plane (the mechanism to cause this rotation will be discussed in Chapter 2). The spins now will precess about B_o which causes the net magnetization to precess around the z-axis. The small differences in the precession frequency, due to the local magnet fields, cause the spin polarization that initially existed along the y-axis to decay over time while it precesses about B_o. This process is called the spin-spin relaxation process and is governed by the time constant T_2. T_2 can thus be monitored by the decay of the spin polarization in the x-y plane after the spins are rotated into the plane. M_{XY} is the magnetization in the xy-plane at a given time, τ, and M_{XY}^0 is the full magnetization as soon as the spins are rotated.

$$M_{XY} = M_{XY}^0(e^{\tau/T_2}) \quad (1.7)$$

Now that spin precession and relaxation has been discussed, we can move to detecting NMR signal. The NMR signal is the report of any spin polarization in the x-y plane. The NMR signal is detected in a similar manner to which we discussed measuring T_2. The spins are rotated from aligned with B_o into the x-y plane. Then the precession of spins around the external magnetic

field is recorded versus time. Parameters such as the magnitude of polarization and frequency of precession are encoded in the NMR signal.

The typical NMR spectra, which most are familiar with, are presented in the frequency domain, with signal versus frequency. The time domain and frequency domain are related by a mathematical operation, a Fourier transform. Since a Fourier transform is only a mathematical operation, all of the information from the NMR signal is contained in both domains. So the magnitude and frequency of the signal is contained within the NMR spectrum. The initial height of the free induction decay (FID) in the time domain is proportional to the area under the curve in the frequency domain. The width of the resonance in the frequency domain, typically defined as the full width at half maximum (FWHM), is proportional to the length, in time, of the FID. The shift away from 0 Hz in frequency can be determined by the frequency of the beats in the time domain.

In the NMR spectrum the center of mass of the resonance is the isotropic chemical shift which can be calculated by the average of the spin principal values.

$$\delta^{iso} = \frac{1}{3}(\delta_{XX} + \delta_{YY} + \delta_{ZZ}) \quad (1.8)$$

Each nuclear spin has three principal values, δ_{XX}, δ_{YY}, and δ_{ZZ}, which correlate to the orientation of the anisotropy. By knowing the three principal values the features of the NMR spectrum can be calculated.

When all three principle values are equal, the NMR spectrum has a Gaussian peak and is called isotropic. This indicates that the nucleus of interest has only one unique symmetry axis. For NMR resonances that do not have principal values that are equal, the principal values are termed

anisotropic. The chemical shift anisotropy (CSA) is derived from the interaction of a spin with a fixed orientation to the external magnetic field. When a spin is fixed in space, the frequency of the NMR signal from this spin is dependent on its orientation in the magnetic field. When there is a powder sample, there is a distribution of spin orientations due to the random nature of the powder. The sum of the NMR resonances from the individual orientations forms a powder pattern. The shape of the NMR resonance when the principal values are unequal is called the CSA powder pattern. The isotropic chemical shift is still calculated with the equation above and other parameters of the NMR spectrum can also be calculated.

$$\delta^{aniso} = \delta_{ZZ} - \delta^{iso} \quad (1.9)$$

$$\eta = \frac{\delta_{YY} - \delta_{XX}}{\delta^{aniso}} \quad (1.10)$$

The principal values are assigned to a CSA lineshape by assigning the δ_{YY} to the value closest to the isotropic chemical shift. Then the principal value furthest from the isotropic shift is the δ_{ZZ} and the δ_{XX} is the remaining value. The anisotropic shift is related to the breadth of the powder pattern. The asymmetry parameter, η, ranges from 0 to 1 and determines the shape of powder pattern, which is informative about the symmetry of the nucleus. When the δ_{XX} and δ_{YY} principal values are equal, η is equal to zero and the powder pattern is considered axially-symmetric. This indicates that the nucleus of interest has only two unique symmetry axes. When η is greater than zero, each principal value is unique and the powder pattern is considered asymmetric.

NMR is capable at detecting signals from all phases of matter, solid, liquid, gas, and supercritical fluid. This allows us to study multi-phase reactions which are not possible in other analytical techniques. NMR can also distinguish the phases of matter by their NMR spectrum. A primary

reason for the ability to distinguish phases is the differences in motion between solids, liquids, and gases. Solids have little motion compared to liquids and gases. Motion of nuclei allows spins to average out the small fluctuations in local magnetic fields because they are moving through all possible variations of the magnetic field on the NMR time scale. This causes the T_2 relaxation time to be longer which makes the peak in the NMR spectrum to be narrower. Solids on the other hand typically stay in a single local magnetic field which means the spins spread out in frequency making broader NMR resonances.

The discussion up to this point has ignored the ability of spins to interact with each other, which referred to as dipole-dipole coupling, with the interaction strength represented by H_d. Spins can couple to every other spin in the sample with a coupling strength inversely proportional to the distance between the nuclei, r. In liquid samples this dipole interaction averages to zero due to the motion, while in solids, the NMR resonances are broadened due to these couplings.

$$H_d \, \alpha \, \frac{\gamma_1 \gamma_2}{r^3} \qquad (1.11)$$

The rest of the dipolar coupling term is constants and terms that relate to the orientation of the spins to each other and their spin state. From this proportionality it is clear that, the larger the gyromagnetic ratio of the spin and the closer the spins are together, the greater the dipolar coupling. The dipolar coupling can be removed with decoupling pulses. By pulsing on the nuclei that are coupled to the spin being detected, the effects of the coupling can be removed. The simplest decoupling pulse simply continuously rotates the coupled spin which does not allow it to couple to the nuclei being detected.

Magic angle spinning (MAS) NMR is now a common technique in solid-state NMR laboratories to average out broadening mechanisms, such as the dipole-dipole coupling, to give solid-state

NMR narrow linewidths similar to liquids NMR. Due to broadening interactions in solid samples, the NMR resonances in solid-state NMR are difficult to assign. The equations that can derive these broadening mechanisms contain the following component.

$$1 - 3\cos^2\theta \quad (1.12)$$

When θ is equal to 54.7°, the magic angle, the component goes to zero. This means that the interaction is averaged to zero and the broadening does not affect the NMR resonance. This makes MAS NMR a powerful tool for assigning the isotropic chemical shift and thus the local environment of the nucleus.

The following chapters will discuss the use of NMR to study carbon dioxide capture and mineralization reactions. NMR is a powerful tool for this application because of its ability to investigate crystalline and amorphous materials while reactions are occurring at conditions other than STP. The multi-phase reactions that occur in both carbon capture and sequestration are important to study for the mitigation of carbon emission and its environmental effects.

Chapter 2: Experimental Methods

2.1 NMR Pulse Sequences

NMR spectroscopy is the primary tool used in the research presented here to investigate carbon capture and sequestration materials. NMR is an analytical technique that observes radiofrequency signals from atomic nuclei to investigate and understand the material of interest. As discussed in Chapter 1, the nuclear spins are detected as spin polarization in the x-y plane, but the mechanism for how to rotate the spins into the x-y plane was overlooked. Rotating the spins into the x-y plane is accomplished by radiofrequency (RF) pulses that are of the correct energy to allow spins to change from one Zeeman energy state to another. The pulses are brought to the sample through the NMR coil which creates a rotating current which induces a magnetic field, B_1, which a spin can align with creating a rotation of the spin. The NMR signal is then detected by the coupling of the spins back to the NMR coil. The spins emit energy that can be detected as a radiofrequency signal which becomes the recorded NMR signal. The RF pulses and signal detection make up the NMR pulse sequence.

2.1.1 Pulse and Acquire

The pulse and acquire sequence, described pictorially in Figure 2.1, is the simplest of the NMR pulse sequences, where a RF pulse is applied to the spins and the signal is detected.

Figure 2 Error! No text of specified style in document.**.1 Pictorial representation of a pulse and acquire NMR pulse sequence.**

The signal is proportional to the angle, θ, in which the spin is rotated from the z-axis. Therefore, a small angle pulse will give a small amount of signal, 90^o pulse will give the largest possible signal, and an 180^o pulse will give no signal. The angle of the pulse is determined by the gyromagnetic ratio of the nuclei being detected, pulse length, t_p, and pulse strength, B_1.

$$\theta = \gamma t_p B_1 \qquad (2.1)$$

To find the pulse that gives the most signal, typically, the pulse length is varied and a nutation curve is measured. This is called a nutation curve because the NMR resonance nutates as a sine wave when the pulse length is varied. Figure 2.2 shows an example of a nutation curve on ^{13}C nuclei of a CO_2 sample.

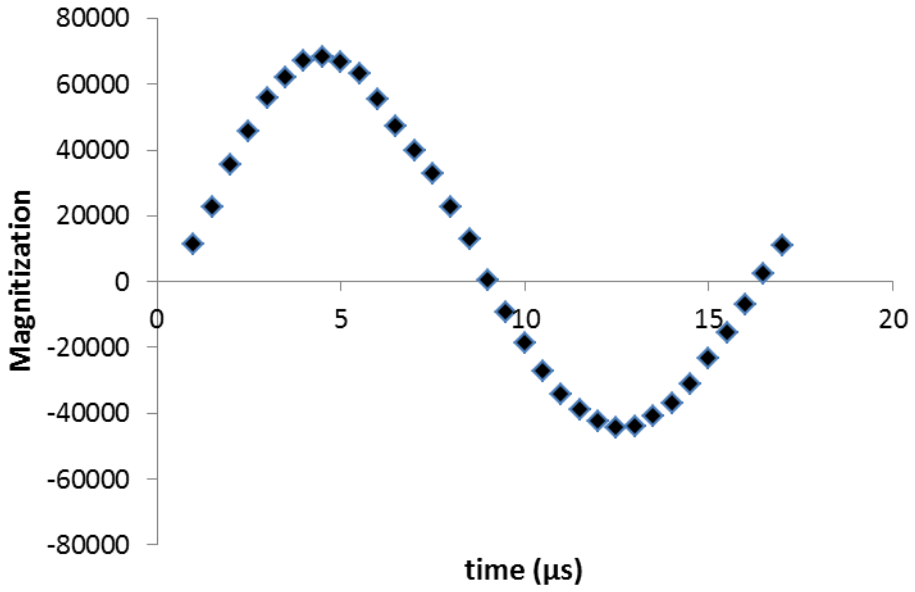

Figure 2.2 An example of a ^{13}C NMR nutation curve.

2.1.2 Hahn Echo

Though, the pulse acquire sequence is often used for data acquisition, other pulses can be used on the spins while they are perturbed from their thermal equilibrium state with radiofrequency pulses. After a 90^o pulse, an echo of the NMR signal can be created with an 180^o pulse that is analogous to an echo that occurs when talking towards a building. This sequence is called the Hahn echo sequence. In our example, the source makes a sound toward a building and the sound wave reflects off of the building and returns to source. In an echo NMR experiment, the pulses create our signal with a 90^o pulse and reflect the signal with an 180^o pulse, before "hearing" the signal with the detector, seen in Figure 2.3. In both examples, the time the sound or signal takes to get to the reflection point, is the same time it takes to get back to the source or detector.

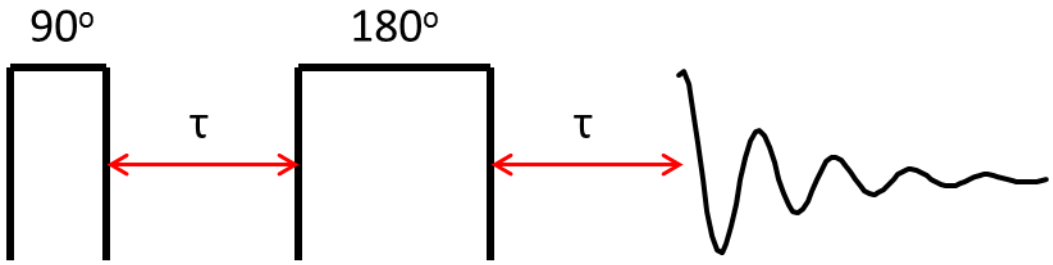

Figure 2.3 Pictorial representation of a Hahn echo pulse sequence.

In a spin system that includes relaxation, the picture gets more complicated since the spins are dephasing with time. To understand the effects of relaxation on an echo experiment imagine two spins, one is precessing slightly faster than the other due to small differences in their local magnetic field. After the 90^{o} pulse, the spins both start at the same point in the xy-plane. Then the precession takes over and the faster spin begins to precess ahead of the other spin. The 180^{o} pulse rotates the spin around the x-y plane, which puts the faster rotating spin behind the slower spin. The spins then precess until the faster spin catches up to the slower spin, creating an echo. The classic example is to describe spins as two runners on a track; the faster runner gets ahead and even laps the slower runner. When the 180^{o} pulse is applied, the runners turn 180^{o}, sending them back in the direction they came from. On the way back now, the faster spin will catch up to the slower spin and after the same amount of time it took to apply the 180^{o} pulse, the spins will be back in the same location in the xy-plane, thus creating an echo.

As the pulse spacing, τ, is increased, the signal decreases at the characteristic T_2 relaxation time of the observed nuclei. Therefore, by acquiring echoes at various values of τ, the T_2 can be measured with a Hahn echo sequence.

2.1.3 Cross Polarization Magic Angle Spinning (CPMAS)

Another pulse sequence that has become common in solid-state NMR is cross polarization magic angle spinning (CPMAS).[32] This pulse sequence can be seen in Figure 2.4 and uses pulses on two different nuclei, the most common pair being ^{1}H and ^{13}C. The purpose of using this sequence is to utilize the spin polarization that can be created on the abundant nuclei, ^{1}H, to enhance the signal of the low abundance nuclei, ^{13}C. The first step in the pulse sequence is to apply a 90^{o} pulse to the abundant spin. Then the spin polarization created with the first pulse is transferred to the low abundance nuclei during the contact time. This is done by applying a pulse on both nuclei, in which the pulses are energy matched by the Hartman-Hahn matching condition. The spin polarization on the low abundance nuclei is then detected. The parameters within the sequence are dependent upon the dipolar coupling between the two nuclei. This is typically performed with decoupling to remove the coupling of abundant nuclei to the detected nuclei during acquisition.

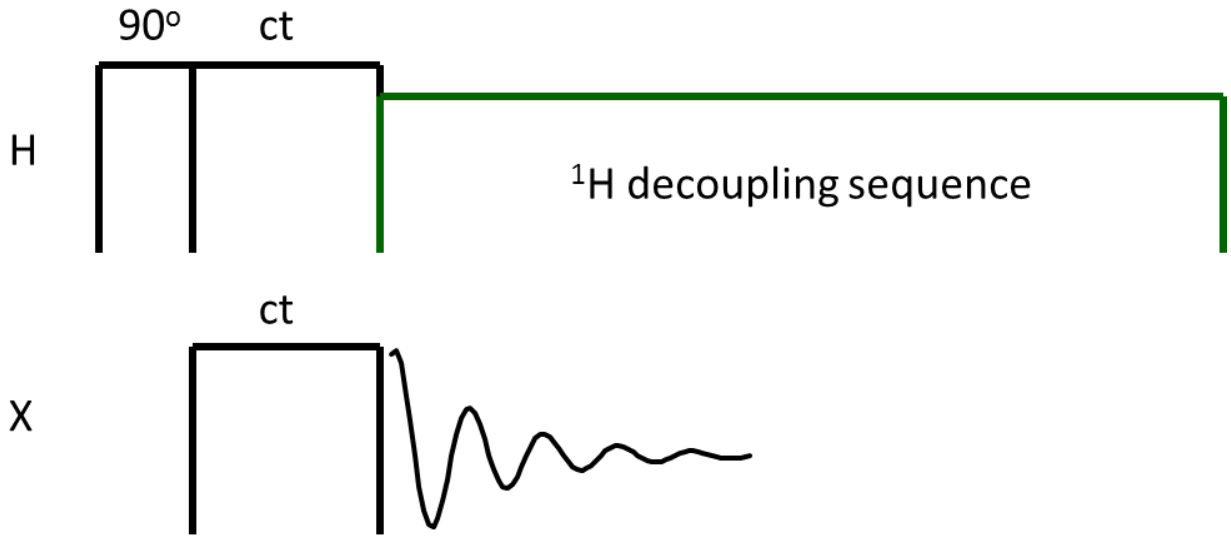

Figure 2.4 Pictorial representation of a X{^{1}H} CPMAS NMR pulse sequence.

The signal acquired with CPMAS can also be echoed with an 180^o pulse, giving the ability to use a CPMAS echo, depicted in Figure 2.5. As with the Hahn echo, by varying the pulse spacing (τ), the T_2 relaxation time can be measured with the CPMAS echo.

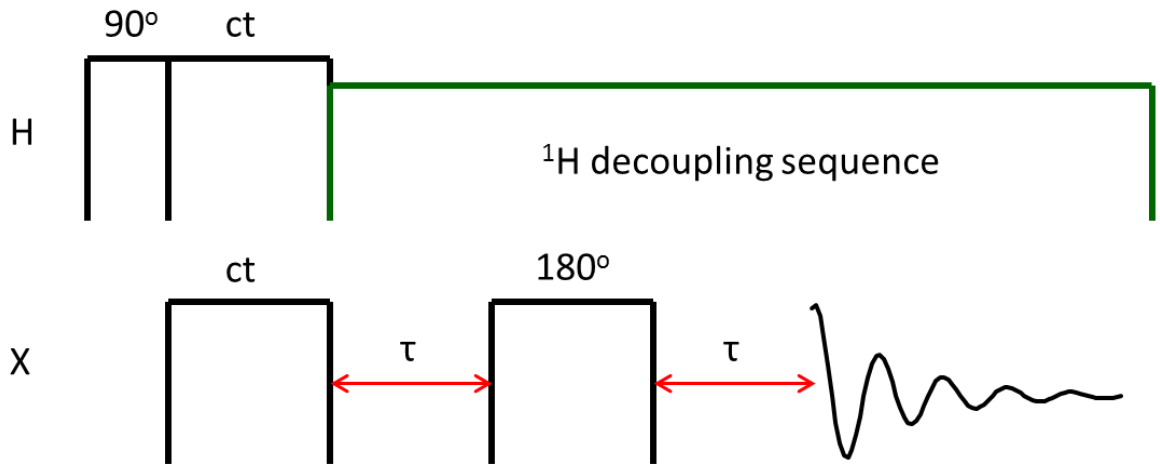

Figure 2.5 Pictorial representation of a X{^{1}H} CPMAS echo NMR pulse sequence.

The ^{1}H decoupling can also be paused for one rotor period which allows the protons to couple with the X nucleus for a time before turning the decoupling pulses on. This is called a CPMAS dipolar dephasing experiment and is shown in Figure 2.6. This pulse sequence can be used to distinguish nuclei that are directly bonded to protons, which will show significant signal attenuation when allowed to couple during the coupling time (τ), from nuclei that have no protons nearby, which will show nearly no signal loss during the time τ.

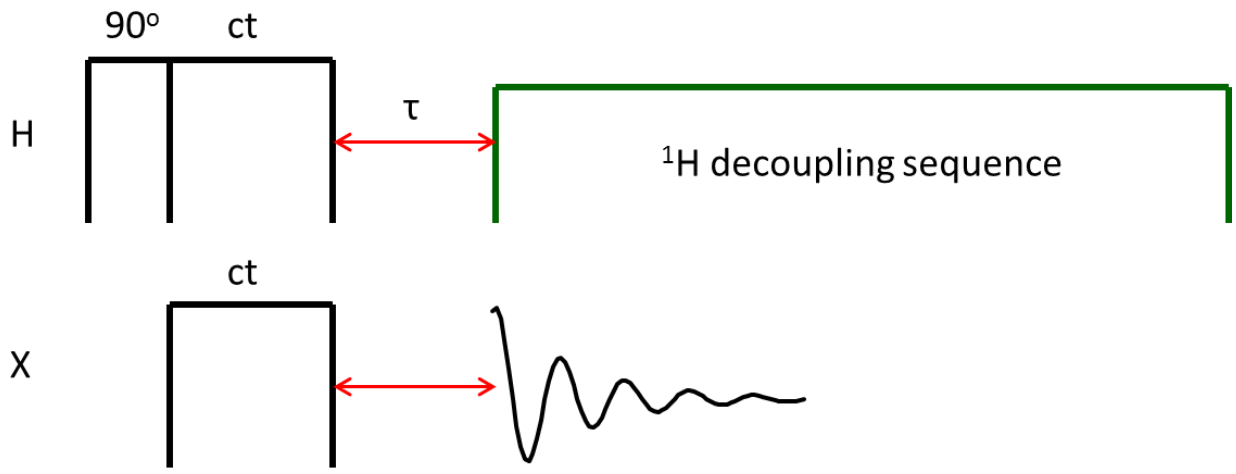

Figure 2.6 Pictorial representation of a X{^{1}H} CPMAS dipolar dephasing NMR pulse sequence.

2.2 NMR Spectrum Fitting

All of the NMR spectra were fit using DMFIT.[33] This program defines the isotropic chemical shift (δ^{iso}), the anisotropic chemical shift (δ^{aniso}), and the asymmetry parameter (η) as were defined in Equations 1.8 through 1.10. The principal values of the CSA powder pattern are defined by the following relationship.

$$\left|\delta_{ZZ} - \delta^{iso}\right| > \left|\delta_{XX} - \delta^{iso}\right| > \left|\delta_{YY} - \delta^{iso}\right| \quad (2.2)$$

2.3 NMR Probe Hardware

Two NMR probes were developed to allow the study of CO_2 capture reactions *in situ*. One probe was used in a narrow bore 14 T magnet and the other could be used in multiple wide bore magnets, at 7 T and 4.7 T. The probes were designed with a tank circuit to be used as the NMR circuit. The circuits were made to allow for easy exchange of the coil, to allow for multiple

sample sizes, and capacitors, to allow many nuclei to be studied. Over the course of the work presented here, these probes have been used to study ^{13}C, ^{23}Na, ^{29}Si, ^{2}H, and ^{195}Pt, as well as other nuclei.

The *in situ* capabilities of the probe utilize a L-shaped glass tube with a small tube, typically 1/16 in, connecting the glass vessel to the probe and a larger glass tube, typically ¼ in, used to hold the sample. The larger tube was made with one end connected to the small diameter tube and the other end open for sample loading. The sample space was first loaded with glass wool to ensure that no sample went into the small diameter tubing. Then the sample was loaded and glass wool was again loaded, this time to ensure that the sample stayed in the center of the sample space. The open end of the sample tube was then flame sealed before attaching the glass reaction vessel to the probe, where the sample was evacuated and the CO_2 gas was introduced. The small diameter tubing was connected to the probe with an O-ring that was within a threaded nut.

2.4 Polymers of Intrinsic Microporosity (PIMs)

A series of polymers of intrinsic microporosity (PIMs), have been studied with solid-state NMR as adsorption materials. These materials have micropores within the polymer due to the combination of a rigid backbone and sites of contortion in the polymers that does not allow efficient chain packing. These pores allow gas to flow through the material, allowing gas capture interactions to occur with the electron rich nitrogen. There are two adsorbing groups per repeat unit of the polymer which has a nitrile groups as the adsorbing unit. The polymer can be functionalized with CO_2-philic groups to enhance adsorption, for example tetrazole (TZPIM) or methyltetrazol (MTZPIM). As a result of the inefficient packing, the adsorbing groups are randomly oriented within the polymer. TZPIM is synthesized by [2+3] cycloaddition post-

polymerization reaction that has been described previously.[14] MTZPIM is synthesized by methylating the tetrazole group after synthesizing TZPIM.[17]

NMR experiments were performed with approximately 100 mg of PIM sample powder. The sample underwent a bake out procedure at 80 ^{o}C under vacuum for 24 hrs for degassing the polymer. A known quantity of ^{13}C-enriched CO_2 was introduced to the samples along with 0.9 atm of He gas for thermal contact during low temperature experiments. The amount of CO_2 was determined from known isotherms.[14,17] The sample tubes were then flamed sealed. The variable temperature ^{13}C NMR studies performed on these materials below 150 K were performed in a Kadel helium research dewar that was coupled to a home-built NMR probe. The studies above 150 K were performed with a stream of evaporated liquid nitrogen with a home-built NMR probe. Data were acquired with a Hahn echo sequence with π pulse lengths of 12 μs.

2.5 Supported Amine Adsorbents

Amine adsorbents studied here are all contained within a SBA-15 mesoporous silica support. Polyethyleneimine (PEI) adsorbent is prepared by impregnating a porous silica support with pre-synthesized PEI.[24] 3-aminopropyltrimethoxysilane (APS), (N-methylaminopropyl)-trimethyoxysilane (MAPS), and (N,N-dimethylaminopropyl)-trimethoxysilane (DMAPS) were synthesized by grafting the amine bearing molecules to the silica surface.[24] The hyperbranched aminosilica (HAS) materials were synthesized by reacting aziridine monomers with the silica surface of SBA-15, as described previously.[34,35]

The amine adsorbents were heated at 95 ^{o}C under vacuum for 8 hours to degas the polymers. The oven is then allowed to return to room temperature under vacuum and is backfilled with nitrogen gas. The sample is then packed into a NMR rotor and placed in the reaction chamber

where the nitrogen gas is evacuated. The samples were then reacted with 1 atm of 99% enriched $^{13}CO_2$ for greater than 2 hours.

In situ ^{13}C NMR experiments of amine adsorbents were performed at 14 T with a home-built single-channel NMR probe. Low field $^{13}C\{^{1}H\}$ CPMAS NMR was conducted at 3 T with a modified commercial HX Chemagnetics probe. ^{13}C NMR T_2 relaxation data of amine samples was collected with $^{13}C\{^{1}H\}$ CPMAS NMR with rotor synchronized ^{13}C π pulses during the tau time.

2.6 Carbon Mineralization Materials

Carbon mineralization reactions were prepared by adding about 1.6 g of forsterite, Mg_2SiO_4, powder and 2.8 mL DI water or brine solution to the reaction vessel. The high pressure vessel was then pressurized with $^{13}CO_2$ (between 90 atm and 120 atm) through cryogenic pressure intensification and heated to 80 ^{o}C to 100 ^{o}C. The reactions were then studied via NMR for 21 days to 60 days. NMR was recorded on a 8.2 T magnet with a home-built single-channel NMR probe that is designed for high pressures and temperatures.[36]

Chapter 3: Carbon Capture

The goal of carbon capture is to reduce the concentration of CO_2 in the atmosphere from CO_2 emissions. A current example of carbon capture technology is amine-bearing solutions used for power plant emissions.[2,10,37,38] The gas mixture is bubbled through the amine solution, typically monoethanolamine (MEA), and CO_2 is able to dissolve and react with the amine compounds in the solution. Advances need to be made in the physical stability of the sorbent material, the regenerability lifetime of the sorbent, and the energy necessary for regeneration.[2] Future carbon capture technologies will include solid adsorbents that improve upon the current solution-state technologies.

The focus of applications in this work is the waste gas that is produced at fossil-fuel burning power plants, or other high CO_2 concentration sources, which are referred to as flue gas. Typical flue gas is a mixture of gases, but here only a few components will be focused on, N_2, H_2O and CO_2. There can be trace amounts of other gases such as O_2, SO_x and NO_x gases in the flue gas, though scrubbers to remove the acid gases can be used in-line prior to any CO_2 capture technology. That leaves the flue gas composition as primarily ~70% N_2, ~15% CO_2, and ~10% H_2O; with other trace gases making up less than 5% of the mixture.[2]

Carbon capture can be accomplished through two main mechanisms, physisorption and chemisorption. The technological strategies are different for each but the goal is the same, to remove CO_2 from a mixed gas stream and ideally separate out a pure CO_2 gas stream. Both mechanisms are also adsorption techniques, where the CO_2 will interact with the surface of the material. Factors such as the selectivity, permeability, and energy requirement for CO_2

desorption are important in determining the efficiency of the specific adsorbent material. This chapter will discuss materials that physisorb and materials that chemisorb CO_2.

3.1 Physisorption Studies

Physisorption uses van der Waals interactions to adsorb CO_2 to the surface of the sorbent material. A strong interaction between an electron-rich adsorbing group and the electron-deficient carbon in CO_2 acts to attract the gas molecule. This interaction will at least restrict the motion (sometimes stopping the motion) of the CO_2 molecule, but does not perturb the electronic structure around the molecule. For CO_2 capture, physisorption interactions are typically used in membrane materials in post-combustion capture from large CO_2 emission point sources. Membrane capture materials can be efficient CO_2 separation technologies that can allow selective gas permeation that allows the preferential passage of CO_2. To efficiently use physisorption interactions as a membrane adsorption material, the relationship of selectivity and permeability must be balanced.

3.1.1 Introduction to Polymers of Intrinsic Microporosity (PIMs)

Polymers of intrinsic microporosity (PIMs) can be used for CO_2 capture and have exhibited ultrahigh CO_2 permeability which is suitable for the large volumes of CO_2 emissions from flue gas. Each PIM material has two electron-rich adsorbing groups per repeat unit of the polymer, seen in Figure 3.1. This structure allows for adsorption of CO_2 through van der Waals interactions with the electron-deficient carbon in CO_2. PIM-1 has a nitrile group as the repeating adsorbing unit and can be functionalized with more electron-rich groups to enhance the adsorption properties of the material. Tetrazole functionalized PIMs (TZPIM) and the

methylated PIM derivative (MTZPIM) have demonstrated enhanced CO_2 capture abilities compared to PIM-1. These PIM materials show high CO_2 permeability and a good CO_2/N_2 selectivity to allow for efficient mixed gas separation.[14,18,19]

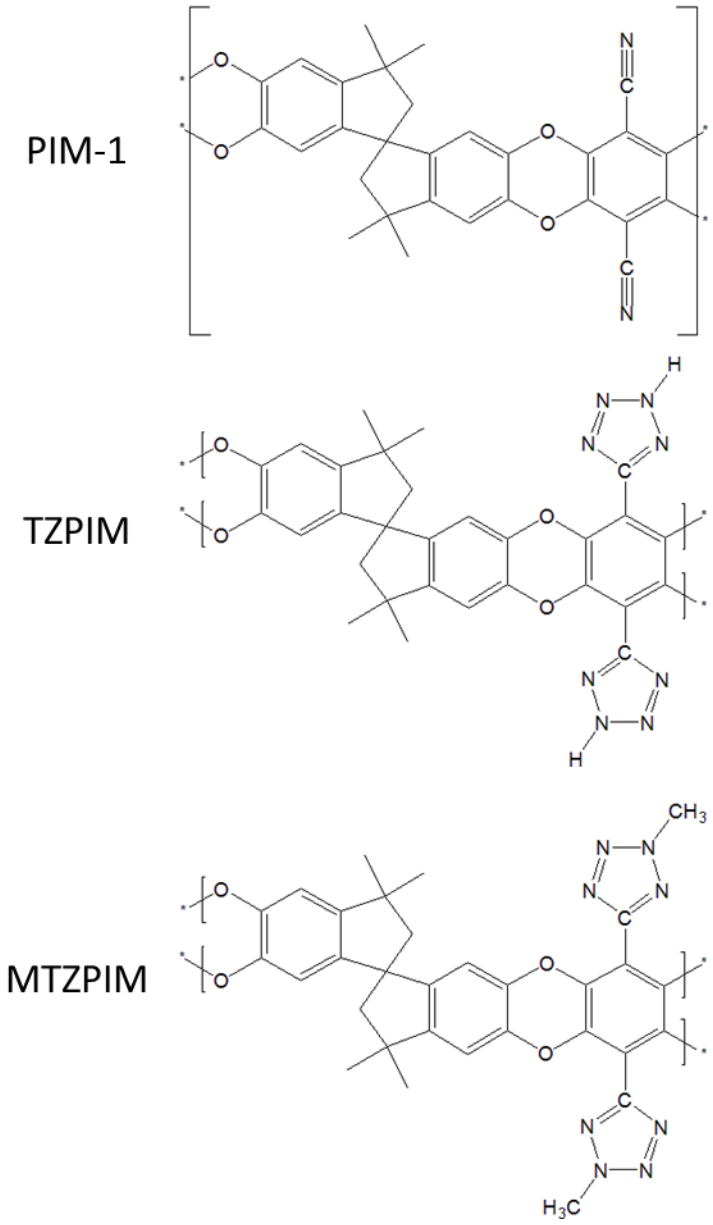

Figure 3.1 Depictions of the monomers that make the PIM adsorption materials.

In situ $^{13}CO_2$ NMR spectroscopy over variable temperature range and multiple loadings of $^{13}CO_2$, allows the study of the adsorption process of CO_2 on PIMs. This technique can distinguish the CO_2 gas from the adsorbed species within the material at the same time. The ^{13}C NMR resonance lineshapes and relaxation times were analyzed to give insights into the distinct characteristics of the adsorption interaction. The dynamics of CO_2 adsorbed on PIMs at the molecular level was studied with NMR to better understand the adsorption properties of the material. Combining this information with macroscopic studies of the permeability and selectivity will provide insight into the CO_2 sorption process and assist in forming better CO_2 separation technologies.

Each of the three PIM samples were prepared with two loadings of $^{13}CO_2$, high and low. These loadings are to simulate a scenario where every CO_2 has an adsorbing unit with which to interact and a scenario where there is an excess of CO_2 as compared to adsorbing sites. To describe the physisorption interaction of CO_2 with PIMs, the TZPIM samples will be discussed first, in detail.[39] Then comparisons will be made to the PIM-1 and MTZPIM samples.

3.1.2 Tetrazole Functionalize PIM (TZPIM)

Figure 3.2 depicts CO_2 adsorbed on a tetrazole group that could be part of TZPIM.

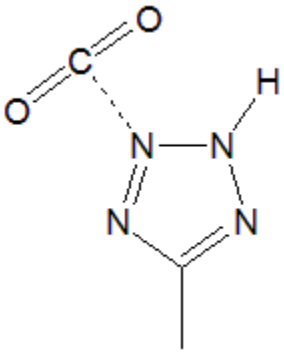

Figure 3.2 Depiction of CO_2 adsorbed on a tetrazole group. The dashed line represents the adsorption interaction.

Figure 3.3 shows representative ^{13}C NMR spectra of a CO_2 gas-only spectrum and a CO_2 spectrum in the presence of TZPIM. Both of these measurements were conducted at room temperature, with 1 atm of $^{13}CO_2$ overpressure, the same number of scans, and in quantitative conditions ($5*T_1$). The spectrum of CO_2 gas is asymmetric in appearance here due to inhomogeneity in the static magnetic field, B_o, arising from the absence of room temperature shims that could potentially correct it. The indications of physisorption include signal enhancement, a broadening of the peak, no chemical shift change, and an increase in spin-lattice (T_1) relaxation. The CO_2 resonance with TZPIM has an integrated ^{13}C signal intensity enhancement of a factor of 9.3. The CO_2 signal intensity increase shows that CO_2 is concentrated by TZPIM in the same region, even when the polymer takes up some of the volume within the NMR coil. The width of the adsorbed gas resonance increases due to the restricted motion of the CO_2 molecules and possibly some broadening due to small magnetic susceptibility differences introduced by TZPIM. The chemical shift is unaffected because the electronic environment of the ^{13}C atom is unperturbed by the van der Waals interaction with TZPIM, an insulating solid material. The T_1 of the CO_2 gas alone is 43.5 ms while the CO_2 adsorbed on TZPIM has a T_1 of 419 ms which reflects the faster intrinsic relaxation in the gas phase as compared to the adsorbed phase.

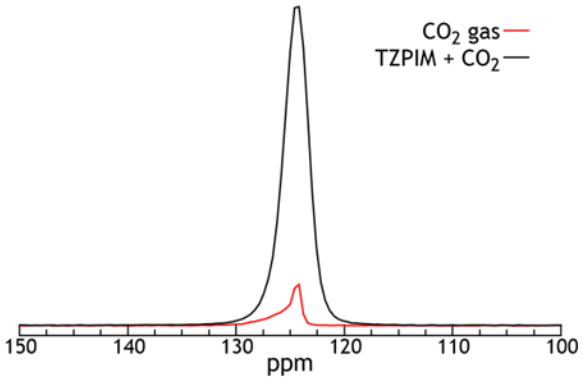

Figure 3.3 ^{13}C NMR resonances of CO_2 adsorbed on TZPIM as compared to CO_2 gas. Both are at a pressure of 1 atm and at 295 K. Each spectrum was acquired with the same number of scans.

Further investigation of the adsorption of CO_2 on TZPIM was conducted by variable temperature studies with ^{13}C NMR with the two previously discussed, high and low CO_2-loaded polymer samples. The samples were studied in the temperature range 8 K and 385 K. It can be assumed that a near-constant amount of CO_2 is adsorbed on the polymer over most of this temperature range. Deviations from this assumption only occur at the higher temperatures and will be discussed when apparent in the ^{13}C NMR T_1 data. This assumption is possible because the samples are made such that there is a minimal gas-phase volume, forcing the loaded $^{13}CO_2$ to be within the polymer region. This system will allow the study of the dynamics of adsorbed CO_2 species, though it does not model an applicable system since the CO_2 is not allowed to be released from the polymer.

The first TZPIM sample was loaded with $^{13}CO_2$ gas that corresponds to 0.30 CO_2 molecules per tetrazole moiety in the sample, which is the" low loading" sample. In this sample, every CO_2 molecule should have access to a tetrazole adsorbing unit. The second TZPIM sample is the "high loading" sample where there is an excess of CO_2 as compared to tetrazole sites; the loading was 0.88 CO_2 molecules per tetrazole. Due to the crowded pore space, some tetrazole units are

sterically hindered making them inaccessible to CO_2 molecules. Therefore, this loading can be used to study the case where there is an excess of CO_2 present. The extra CO_2 molecules will be forced to adsorb at less favorable adsorption sites.

Figure 3.4 depicts ^{13}C NMR resonances for representative temperatures from the variable temperature range. Each spectrum was observed via a Hahn echo sequence with a pulse spacing (τ delay) of 50 μs. Overall, the ^{13}C NMR lineshape is seen to narrow as the temperature is increased from 8 K to 385 K. Note, that the low loading sample has a lower signal-to-noise ratio since there are fewer ^{13}C nuclei as compared to the high loading sample.

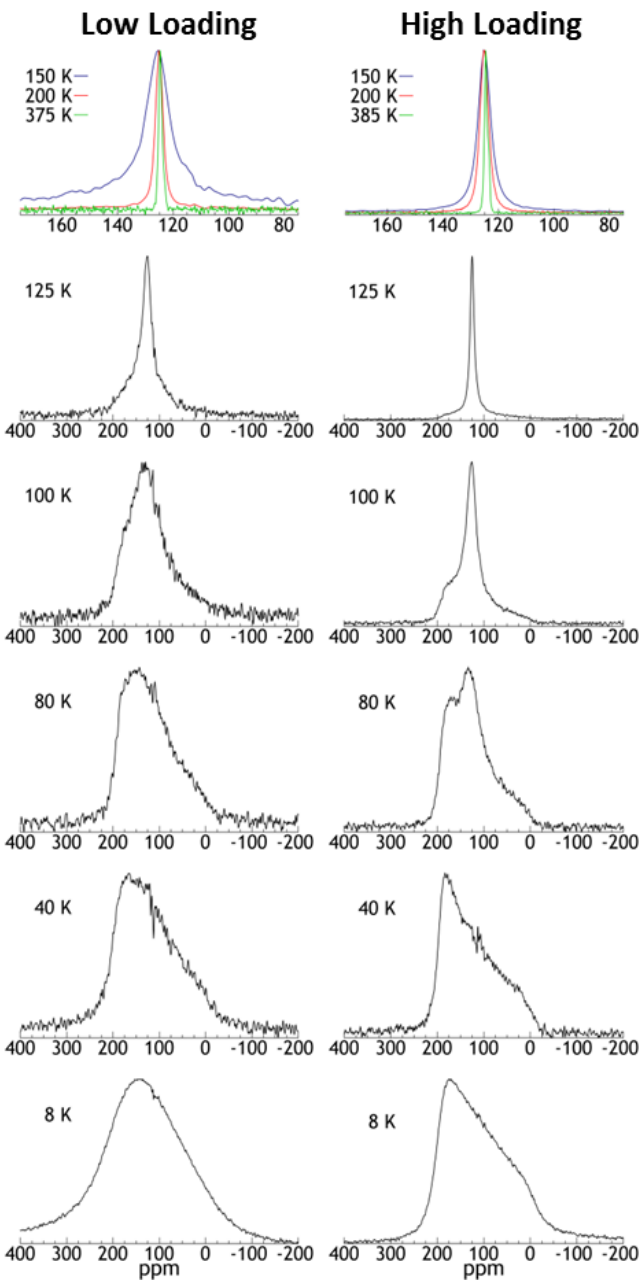

Figure 3.4 ^{13}C NMR resonances of CO_2 adsorbed on TZPIM. The spectra on the left are from the low loading sample, and the spectra on the right are from the high loading sample. Note: the top spectra have an expanded x-axis to show the narrow resonances at higher temperatures. 100 ppm = 5.08 kHz.

In order to analyze the ^{13}C NMR lineshapes, the interactions that broaden the adsorbed $^{13}CO_2$ spectra must be discussed. There are three dominant line broadening interactions in the adsorbed

$^{13}CO_2$ on TZPIM surface: chemical shift anisotropy (CSA),[40] which is characteristic of linear CO_2 molecules; ^{13}C-^{1}H dipolar coupling between the adsorbed $^{13}CO_2$ and the TZPIM polymer hydrogen atoms; and ^{13}C-^{13}C homonuclear dipolar coupling between two $^{13}CO_2$ molecules. As expected, at low temperatures (below 80 K), the dominant line broadening mechanism is due to the CSA, which is seen easily in the 40 K spectra. The spectra at 8 K have an extra broadening mechanism that will be discussed later. In both samples an axially-symmetric powder pattern is observed by ^{13}C NMR for the $^{13}CO_2$ molecules adsorbed to the TZPIM polymer. The lineshape is axially symmetric because there are only two unique principal values, one along the O-C-O bond and two perpendicular to this bond. The lineshape is similar to the characteristic powder pattern exhibited for the CSA of randomly oriented solid $^{13}CO_2$.[41,42] This indicates that on the NMR timescale (10^{-4} seconds), the adsorbed CO_2 molecules have a nearly fixed orientation with respect to the magnetic field. The random orientation of the $^{13}CO_2$ molecules arises because the tetrazole units have a fixed orientation with respect to the external magnetic field. The random nature of the PIM polymer means that the overall orientation distribution of the tetrazole units is isotropic. This means that the adsorbed CO_2 molecules, which have a fixed molecular orientation, have an isotropic distribution within the polymer and gives rise to the axially symmetric CSA powder pattern.

At the low temperatures (below 80 K), the spectra are best described by the width of the powder pattern, $\Delta\sigma_{eff}$. At 40 K, the spectra have $\Delta\sigma_{eff}$ = 290 ppm, which is close to previously reported values found in solid CO_2 (325 ppm)[41] and another adsorbed system (315.3 ppm).[12,13] As the temperature increases in this regime, the lineshape keeps the axially symmetric pattern but narrows slightly. This narrowing is due to librational motions which constitutes "orientational rocking" in the bottom of the adsorption potential well.[43] This motion can be defined by an

angle, θ, which is the angle between the $^{13}CO_2$ axis and the minimum energy CO_2 adsorption axis. A representation of librational motion is depicted in Figure 3.5.

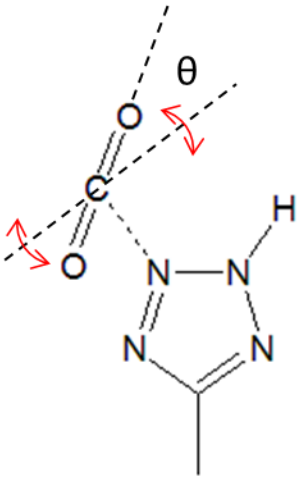

Figure 3.5 Depiction of CO_2 adsorbed on a tetrazole group with the θ that defines the librational motion of CO_2.

As the temperature is increased, the adsorbed molecules oscillate torsionally, creating a distribution of θ values. This distribution of angles decreases the time-averaged CSA, resulting in a slightly narrower CSA powder pattern. The oscillation can be visualized as a linear CO_2 molecule rocking about the binding axis with the carbon fixed at the adsorption site, like a teeter-totter. The width of the CSA lineshape with librational motion can be determined by the following equation, when the broadening is dominated by the CSA interaction.[44]

$$\Delta\sigma_{eff} = \Delta\sigma\left(\frac{3}{2}\overline{\cos^2\theta} - \frac{1}{2}\right) \quad (3.1)$$

The term Δσ is the width of the CSA powder pattern when the orientationally static CO_2 has the full broadening from the CSA. At the lowest temperatures, the CO_2 molecules are completely static and θ = 0. As the temperature is increased, the distribution of θ values increases which leads to a decrease of the $\cos^2\theta$ term and the slight narrowing of $\Delta\sigma_{eff}$. It should be noted here that if the CO_2 molecule undergoes a "head-to-tail" flip where the oxygen molecules switch

places exactly, there is no effect on the width of the CSA. This motion would add π to the angle θ which does not affect the $\cos^2\theta$ term.

At the middle temperatures (80 K to 100 K), the CO_2 molecules reorient due to site-to-site translational hopping. Each adsorption site has a different orientation with respect to the magnetic field, therefore when the CO_2 molecule hops from one site to another; it is accompanied with a change in orientation. The reorientation of the CO_2 molecules with respect to the magnetic field results in a motional averaging of the CSA interaction. The line narrowing that is evident in the spectra, at 80 K in the high loading sample and 100 K in the low loading sample, are due to this translational hopping. This type of translation-reorientation motion has been found in other materials such as solid CO_2,[41] α-CO,[45] N_2O[46] and benzene[47] as well as CO_2 adsorbed onto a MOF material.[12,13] A depiction of this hopping motion is shown in Figure 3.6.

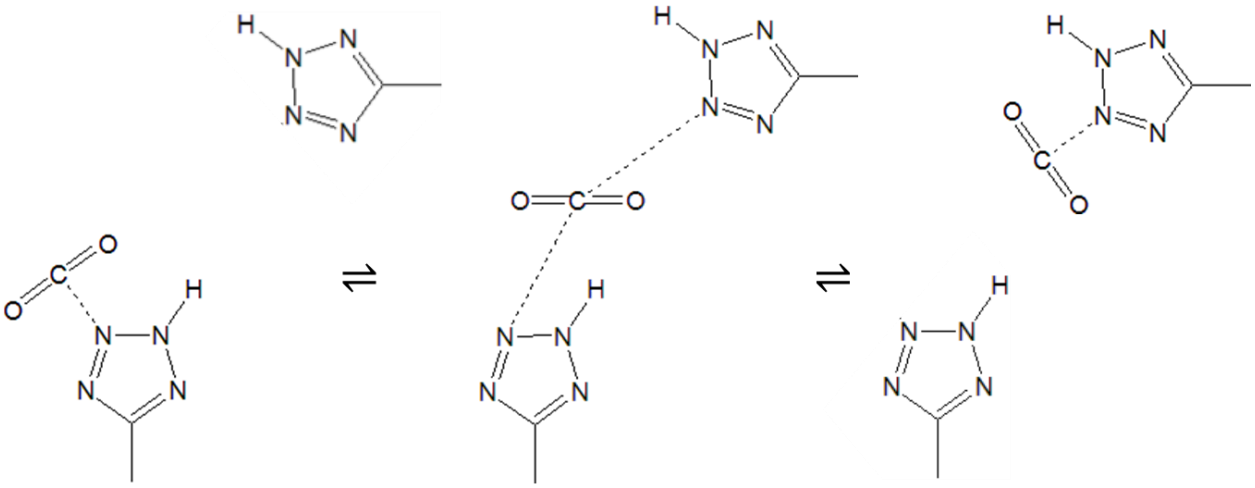

Figure 3.6 Depiction of CO_2 adsorbed on a tetrazole group with a potential translation-reorientation hop from one tetrazole group to another.

At the higher temperatures, the translational hopping of CO_2 molecules between randomly-oriented adsorption sites and the resulting reorientations lead to a single, symmetric ^{13}C NMR resonance at 125 ppm. That is, the CSA interaction is time-averaged to zero on the NMR timescale. The resonance continues to narrow as the temperature is increased from 125 K to 385 K. This indicates that the CO_2 molecules are hopping and reorienting more rapidly as the van der Waals interactions between the adsorbed CO_2 and the tetrazole units becomes small relative to the thermal energy, k_BT. In comparison to the materials that also undergo translation-reorientation hopping, the bulk solids (CO_2, α-CO, and N_2O) have high crystal symmetry and have similarly time-averaged CSA interactions at high temperatures. In contrast, the CO_2 adsorbed on Mg-MOF-74 does not show this time averaged CSA, because the MOF confines the CO_2 into long hexagonal channels.[11,12] The CSA is time-averaged to a non-zero value because the CO_2 molecules are not able to access every possible orientation to the external magnetic field within a single channel. The $^{13}CO_2$ NMR resonance in the MOF will continue to show an axially symmetric powder pattern, though with a reduced width, at high temperatures.[12,13]

In Figure 3.4, the temperature-dependent linewidth shows that the narrowing due to translation-rotational hopping in the low loading sample occurs in a single temperature step starting near 100 K. In the high loading sample, the narrowing occurs in two steps. The narrowing begins near 80 K with a subset of the CO_2 molecules beginning to hop at this temperature. A second subset of molecules is more tightly adsorbed to TZPIM and persists as an axially symmetric powder pattern up to 100 K. These two subsets of CO_2 molecules are presumed to access different adsorption sites that have different adsorption affinities for CO_2. In the low loading sample, every CO_2 molecule seems to have a similar adsorption site since the line narrowing occurs over the same temperature range.

The FWHM of the ^{13}C NMR resonance in Hz is plotted versus temperature in Figure 3.7. The linewidth is inversely proportional to the time constant T_2^*, which is defined by the time necessary for the signal to decay into the noise. At low temperatures, when the CO_2 molecule is tightly adsorbed and the CSA powder pattern is apparent, the linewidth is nearly constant. The torsional libration motions cause a small amount of narrowing in this temperature range. As the temperature increases about 100 K, the CO_2 molecules reorient faster due to the onset of the site-to-site hopping, which causes the ^{13}C linewidth to rapidly decrease. In the cases where two subsets of CO_2 molecules exist, the linewidth for each signal is plotted separately. In the high loading sample, the linewidth between 80 K and 175 K is smaller due to the more weakly adsorbed molecules reorienting more rapidly. It is also evident in the NMR linewidths that the onset of line narrowing occurs at a lower temperature for the high loading sample, due to the weakly-adsorbed molecules.

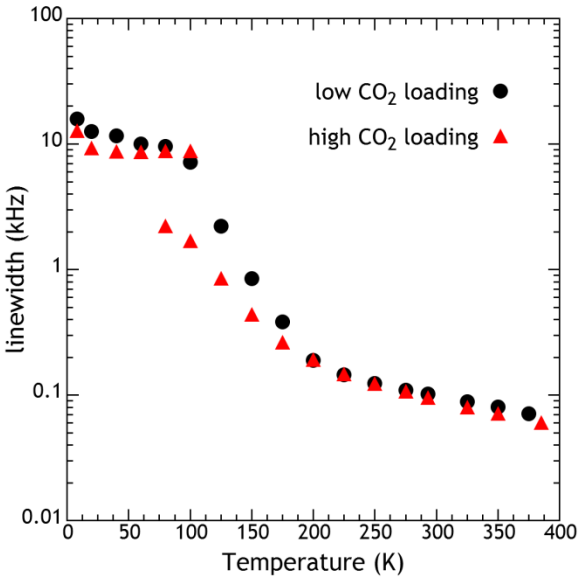

Figure 3.7 ^{13}C NMR linewidths of CO_2 adsorbed on TZPIM as a function of temperature.

Figure 3.8 is a plot of the temperature dependence of the ^{13}C spin-spin relaxation time, T_2, which was determined from spin echoes. This relaxation data can assist in differentiating the mechanisms of line narrowing that occur with temperature.[41,48] At low temperatures, when there are no CO_2 reorientations, T_2 is determined by a combination of the ^{13}C-^{13}C dipolar coupling between nearby $^{13}CO_2$ molecules and ^{13}C-^{1}H dipolar coupling between the adsorbed CO_2 molecule and the hydrogen from the adsorbing tetrazole units. The dipolar couplings that occur during the NMR experiment will contribute to attenuation of the echo signal, leading to a shorter T_2. Coupling that can be reversed by RF pulses, or are time-averaged to zero, lead to a longer T_2. The ^{13}C-^{13}C dipolar coupling will not be reversed by the ^{13}C π pulse, which is responsible for the echo signal, because both spins will be inverted. The ^{13}C-^{1}H dipolar coupling will not be refocused due to ^{1}H-^{1}H spin flips that are driven by the ^{1}H-^{1}H dipolar coupling. Therefore, both ^{13}C-^{13}C and ^{13}C-^{1}H dipolar couplings will lead to the attenuation of the echo signal at low temperatures. These interactions are temperature independent in the range where all the CO_2 hopping motion is frozen out, as evidenced by the T_2 plateau from 8 K to 40 K. Both samples have the same value for the relaxation plateau, which indicates that the relaxation is dominated by the ^{13}C-^{1}H dipolar coupling that is present equally in both samples.

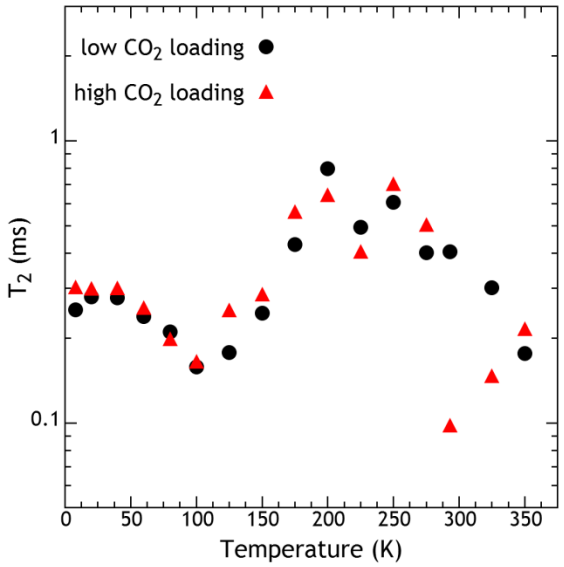

Figure 3.8 ^{13}C NMR T_2 relaxation time constant for CO_2 adsorbed on TZPIM as a function of temperature.

In the intermediate temperature range, 40 K to 100 K, the T_2 decreases due to the onset of the reorientational motion.[41,45] In this strong collision regime,[45,49] a single hop of a CO_2 molecule causes the ^{13}C frequency of the molecule to change sufficiently to dephase the spin before the spin echo. Every hop results in a spin reorientation, but the hops do not happen frequently enough for the resonance to be motionally narrowed. Therefore, the T_2 is approximately the mean time between hopping events in this temperature regime. The T_2 minimum occurs near the onset of the line narrowing,[41] where the CO_2 molecular hops occur at approximately one time per the rigid-lattice free induction decay (FID), approximately 100 μs. The high loading sample does not have as deep of a T_2 minimum because the subsets of CO_2 molecules narrow at different temperatures. In the high temperature regime (above 100 K), T_2, seen in Figure 3.8, and T_2^*, seen as the inverse of Figure 3.7 as discussed above, increase together due to rapid reorientation of the CO_2 molecules caused by fast translational hopping. Above 150 K, the T_2 is longer than the low temperature plateau value (which was determined by the ^{13}C-^{1}H and ^{13}C-^{13}C dipolar

coupling). Thus, above 150 K, the dipolar couplings are being averaged to zero due to the motion of the CO_2 molecules, confirming the mechanism of site-to-site hopping at higher temperatures. Once the temperature is raised about 250 K, the T_2 values are not well understood. A fraction of the CO_2 may be exchanging between an adsorbed phase and the gas phase, which would break the assumption of a constant amount of adsorbed CO_2 and could lead to the observed T_2 behavior.

At very low temperature, such as 8 K, the $^{13}CO_2$ resonance is broadened by additional mechanisms than just CSA, which can be seen in Figure 3.4. These broadening effects are particularly evident in the low loading sample. The T_2 relaxation shows little change over the low temperature range, from 8 K to 40 K. This demonstrates that the broadening is inhomogeneous since the additional line broadening is refocused by the ^{13}C π pulse. Also, the additional broadening can not be attributed to molecular motions since all motion is frozen out below 80 K. We propose that this broadening seen at 8 K is due to the magnetic moment of the electrons and their contribution to the magnetic susceptibility of the material. For free electron spins, the contribution will decrease as 1/T at high temperature, following Curie's Law, which leads to the lack of this broadening mechanism except at the lowest temperatures. At 8 K, in an external magnetic field of 4.7 T, the electron spin polarization should be nearly 40%. With this large spin polarization, the electron spins would cause a line broadening in the ^{13}C NMR at 8 K. A low temperature similar broadening was also present for CO_2 adsorbed on Mg-MOF-74.[12,13]

The ^{13}C spin-lattice relaxation time, T_1, is plotted versus temperature in Figure 3.9.[50] Both the low and high loading samples follow the same trend in T_1, though their values are offset from one another. The T_1 relaxation time decreases from 40 K to 125 K due to the onset of translational hopping of the CO_2 molecules.

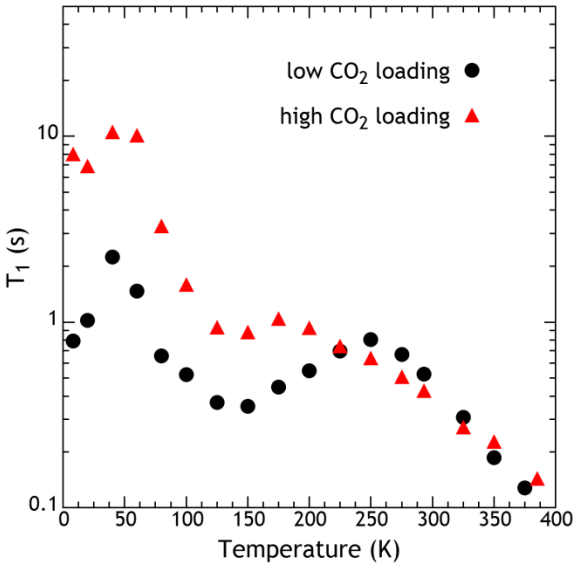

Figure 3.9 ^{13}C NMR T_1 relaxation time constant for CO_2 adsorbed on TZPIM as a function of temperature.

The T_1 again decreases for the low loading sample above 250 K and for the high loading sample above 175 K. These decreases can be attributed to CO_2 exchange between adsorbed and gas phases. To fully model this exchange system, the intrinsic gas phase[51] and adsorbed phase relaxation rates as well as the exchange rate between the CO_2 phases need to be known. Despite not fully modelling this complicated exchange system, we can extract some insights. First, the T_1 of $^{13}CO_2$ gas at 1 atm and 298 K has been measured as 0.06 seconds, which is much faster than the relaxation of adsorbed CO_2 molecules. Thus, the presence of a small amount of CO_2 in the gas phase could account for the faster T_1 relaxation observed above 250 K since the CO_2 will exchange between the gas phase and adsorbed phase. When a CO_2 molecule undergoes exchange, the measured T_1 relaxation time for the molecule will be an average of the gas phase relaxation and the adsorbed phase relaxation. Second, the exchange rate between adsorbed CO_2 and CO_2 gas will naturally increase as the temperature increases. Combined, these two facts

broadly fit the exchange model to the high-temperature T_1 data where the T_1 relaxation becomes increasingly rapid with increasing temperature.

The difference in T_1 relaxation between the two samples, besides the offset at low temperatures, is the temperature at which the onset of T_1 decrease is observed at high temperature (greater than 150 K). The low loading sample decreases at a higher temperature (250 K) than the high loading sample (175 K) because all of the CO_2 molecules are adsorbed to the best adsorption sites, the tetrazoles. In the high loading sample, the subset of CO_2 molecules that are adsorbed on less favorable sites exchange with the gas phase at a lower temperature, which causes the overall T_1 to begin to decrease at a lower temperature.

Site-to-site hopping of the CO_2 molecules adsorbed on tetrazole groups in TZPIM is evident from the variable temperature ^{13}C NMR study. When an excess of CO_2 molecules are present, a second adsorption site becomes obvious. The CO_2 molecules are only weakly adsorbed on the second site which is apparent by the indication of hopping at lower temperatures. While the dynamics of CO_2 adsorbed on TZPIM can be well understood from this data, little can be determined about the second adsorption site. The other PIM materials were able to yield details of the second adsorption site.

3.1.3 PIM-1

PIM-1 uses the electron rich nitrogen in the nitrile group to adsorb CO_2 with an interaction with the electron deficient carbon, depicted in Figure 3.10.

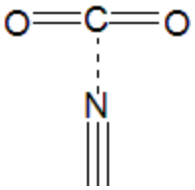

Figure 3.10 Depiction of CO_2 adsorbed on a nitrile group. The dashed line represents the adsorption interaction.

The ^{13}C NMR resonance for adsorbed CO_2 was recorded over variable temperatures with a Hahn echo sequence with a 50 μs pulse spacing (τ), shown in Figure 3.11. CO_2 adsorbed on PIM-1 has a similar CSA lineshape as observed in TZPIM. The onset of site-to-site hopping is seen in the low loading PIM-1 sample at 80 K, and these translational-reorientation jumps are occurring rapidly by 125 K. The signs of hopping occur at a lower temperature for PIM-1 than for TZPIM, indicating that the tetrazole group more strongly adsorbs CO_2 compared to the nitrile group. The high loading PIM-1 sample also shows evidence of two adsorbing sites. The more weakly adsorbed CO_2 molecules are hopping rapidly by 100 K, while the strongly adsorbed molecules exhibit a time-averaged CSA by 125 K.

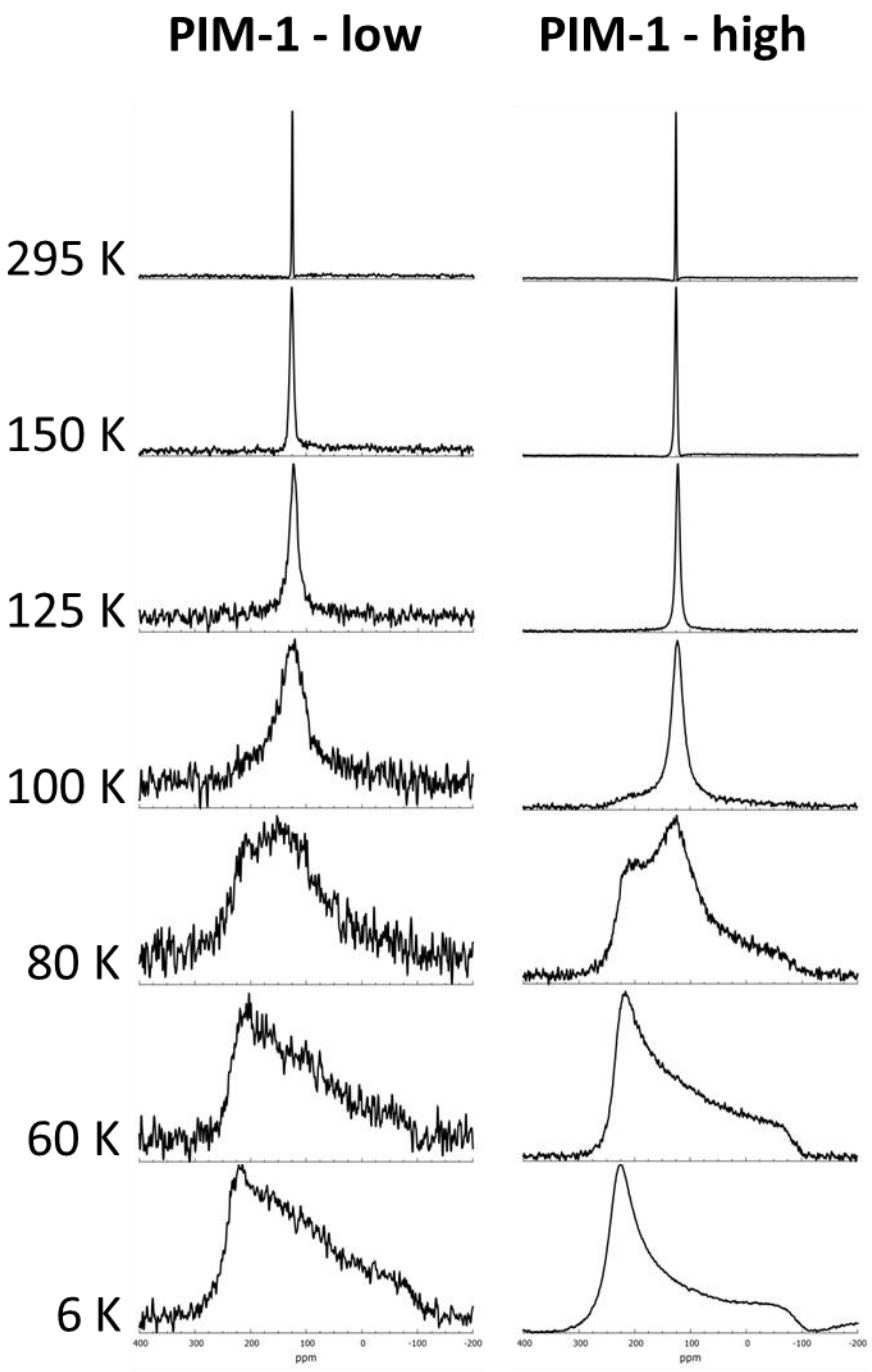

Figure 3.11 ^{13}C NMR resonances of CO_2 adsorbed on PIM-1. The spectra on the left are from the low loading sample, and the spectra on the right are from the high loading sample. 100 ppm = 5.08 kHz.

3.1.4 Methylated Tetrazole Functionalize PIM (TZPIM)

MTZPIM adsorbs CO_2 by the electron rich methylated tetrazole group, depicted in Figure 3.12.

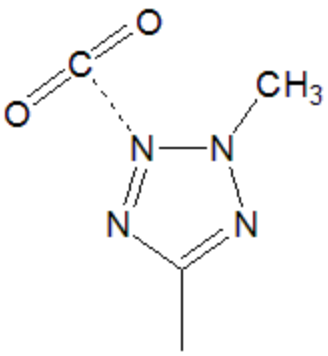

Figure 3.12 Depiction of CO_2 adsorbed on a methylated tetrazole group. The dashed line represents the adsorption interaction.

This PIM sample was also studied at low temperatures with the spectra shown in Figure 3.13. The low loading MTZPIM sample, like the first two samples, shows the onset of hopping in a single process beginning at 100 K. This indicates that the site-to-site hopping in MTZPIM begins at a similar temperature to TZPIM and therefore adsorbs CO_2 as strongly as TZPIM. In the high loading MTZPIM sample, the weakly adsorbed CO_2 molecules begin hopping around 80 K while the more strongly adsorbed molecules stay at a single type of site on the NMR timescale.

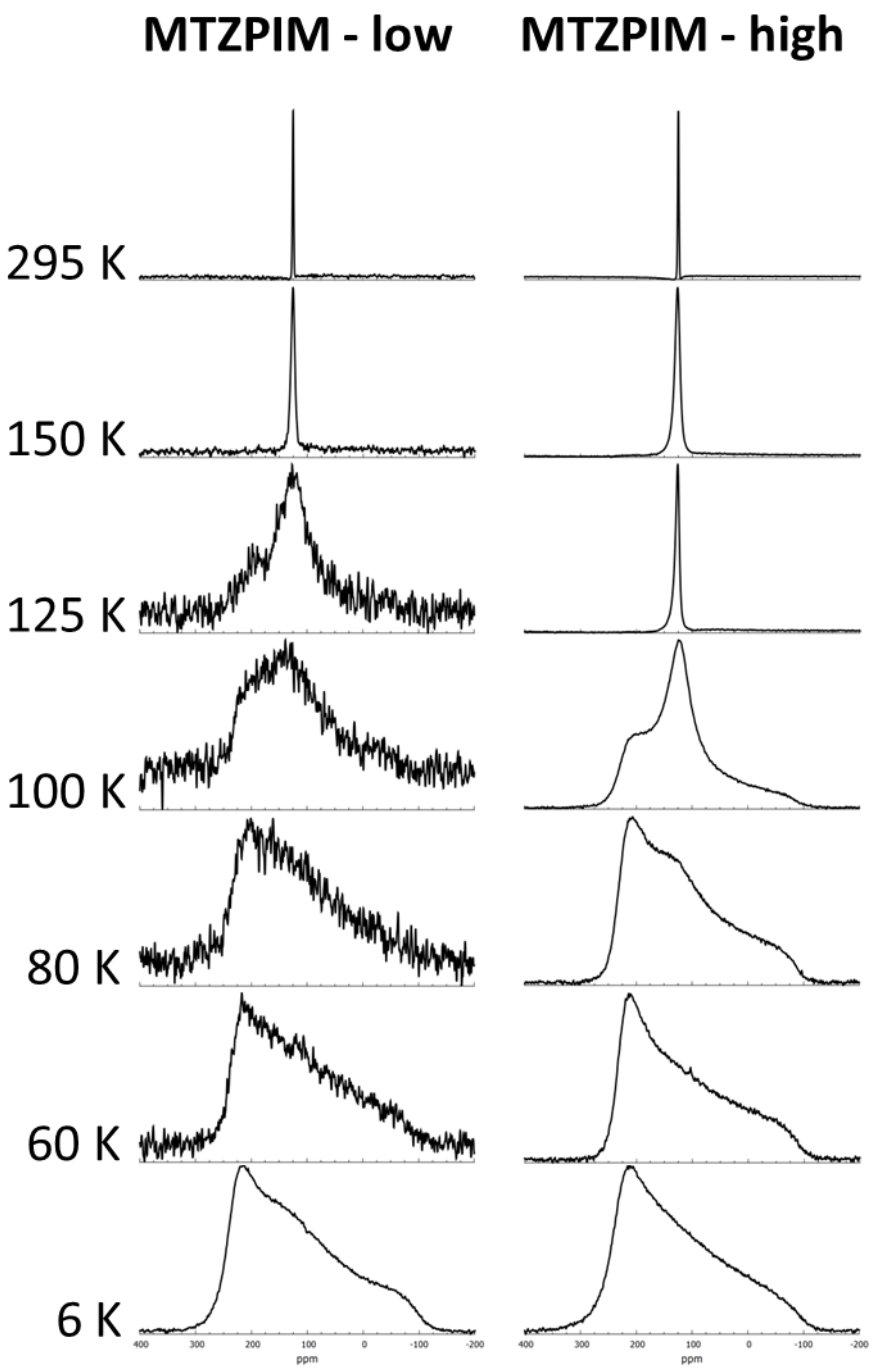

Figure 3.13 ^{13}C NMR resonances of CO_2 adsorbed on MTZPIM. The spectra on the left are from the low loading sample, and the spectra on the right are from the high loading sample. 100 ppm = 5.08 kHz.

3.1.5 PIMs Conclusions

CO_2 has been seen to undergo translation-reorientation hopping between adsorption sites on PIM-1, TZPIM, and MTZPIM. This process has infrequent jumps starting by 50 K, which is first evidenced in the spin-echo T_2. The hopping becomes rapid above 100 K, which can be seen by the time-averaged CSA powder pattern. By 250 K, the adsorbed CO_2 has significant exchanged with the gas phase. When there is an excess of CO_2 as compared to the adsorbing unit, a second adsorption site becomes apparent.

The analysis of the ^{13}C NMR lineshapes of CO_2 adsorbed on PIMs shows similar adsorption profiles for TZPIM and MTZPIM while PIM-1 does not adsorb CO_2 as strongly. In the low loading samples, each PIM shows the onset of site-to-site hopping in a single step, which indicates that every CO_2 molecule was adsorbed on the more favorable adsorbing sites. In the high loading samples, the CO_2 molecules that are adsorbed on the electron rich adsorbing sites begin hopping at the same temperatures that they did on the low loading sample. Weakly adsorbed CO_2 molecules became evident when there was an excess of CO_2 in the PIM samples. In each PIM sample, the weakly adsorbed CO_2 began hopping around 80 K and rapid hopping was observed by 100 K, where the CSA powder pattern was averaged to zero. This observation indicates that the second adsorption site is similar in each of the PIM samples. Since the adsorbing site changes on each sample, especially for the PIM-1 nitrile group, this functional group is not responsible for providing the secondary adsorption site. Consequently, the weak adsorption site is likely on the polymer itself, which is a consistent moiety between the three PIMs.

3.2 Chemisorption Studies

Chemisorption is a process in which the adsorbed gas forms a chemical bond with the surface of the adsorbent. For solid supported adsorbents, the CO_2-rich flue gas is passed through the porous material. The CO_2 is chemisorbed by the sorbent, and the rest of the flue gas ideally passes through the pores, separating the CO_2 from the rest of the gas. The CO_2 is then collected as a pure gas stream by some combination of temperature and pressure treatment. Since the chemisorption process is based on chemical reactions, the process has a naturally high selectivity for CO_2 over other parts of the flue gas. Attention then is needed for the energy required to heat and evacuate the sample in order to regenerate the adsorbent material when releasing the CO_2 gas.

3.2.1 Supported Amine Adsorbents

Carbon capture materials can use amine functional groups as sites for chemisorption. Amines are Lewis bases with a lone pair on the nitrogen and one or more bonds to the carbons making up the polymer. Amines are then categorized by the number of carbon side-chains, depicted in Figure 3.14. Primary amines contain one side chain and two hydrogens, secondary amines have two side chains and one hydrogen, and tertiary amines have three side chains.

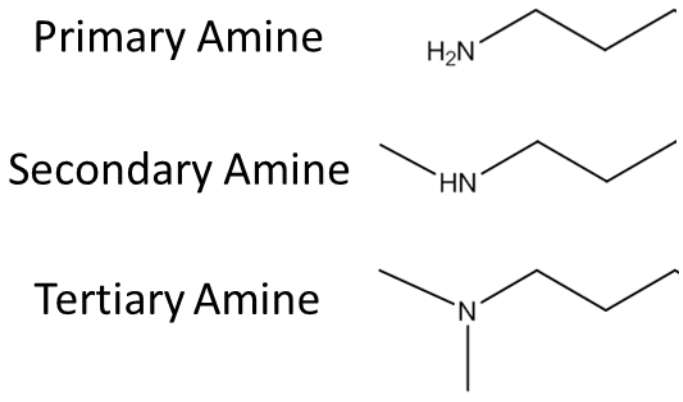

Figure 3.14 Representation of the three types of amine sites.

The materials studied contained amine-bearing molecules or polymers on SBA-15 mesoporous silica. The amorphous silica support structure has an ordered pore structure. The amine-bearing polymers are broken up into three classes. **Class 1** materials have a hyperbranched amine bearing polymer, typically polyethyleneimine (PEI), that is physically impregnated into the support structure.[52] PEI, used in these studies, contains primary, secondary, and tertiary amine groups. The tertiary amines create "branches" within the polymer by allowing polymerization in three directions because each bond is to a carbon. When multiple "branches" are present, the polymer is considered hyperbranched. **Class 2** materials have an amine-bearing compound that is covalently bound to the surface of the support structure.[53,54] Amine compounds can be selected that contain a single type of amine or a mixture of amine types. For example 3-aminopropyltrimethoxysilane (APS) is a compound with a primary amine site. **Class 3** materials have a hyperbranched aminosilica polymer (HAS) that is covalently bonded to the surface of the silica support.[9,34] This class of materials contains all three types of amines, like class 1, as well as the covalently-bound structure, like class 2. This combines the high amine density of a class 1 material with the structural integrity of the covalent bond found in class 2 materials. Figure 3.15 shows a representation of the three classes of amine adsorbents.

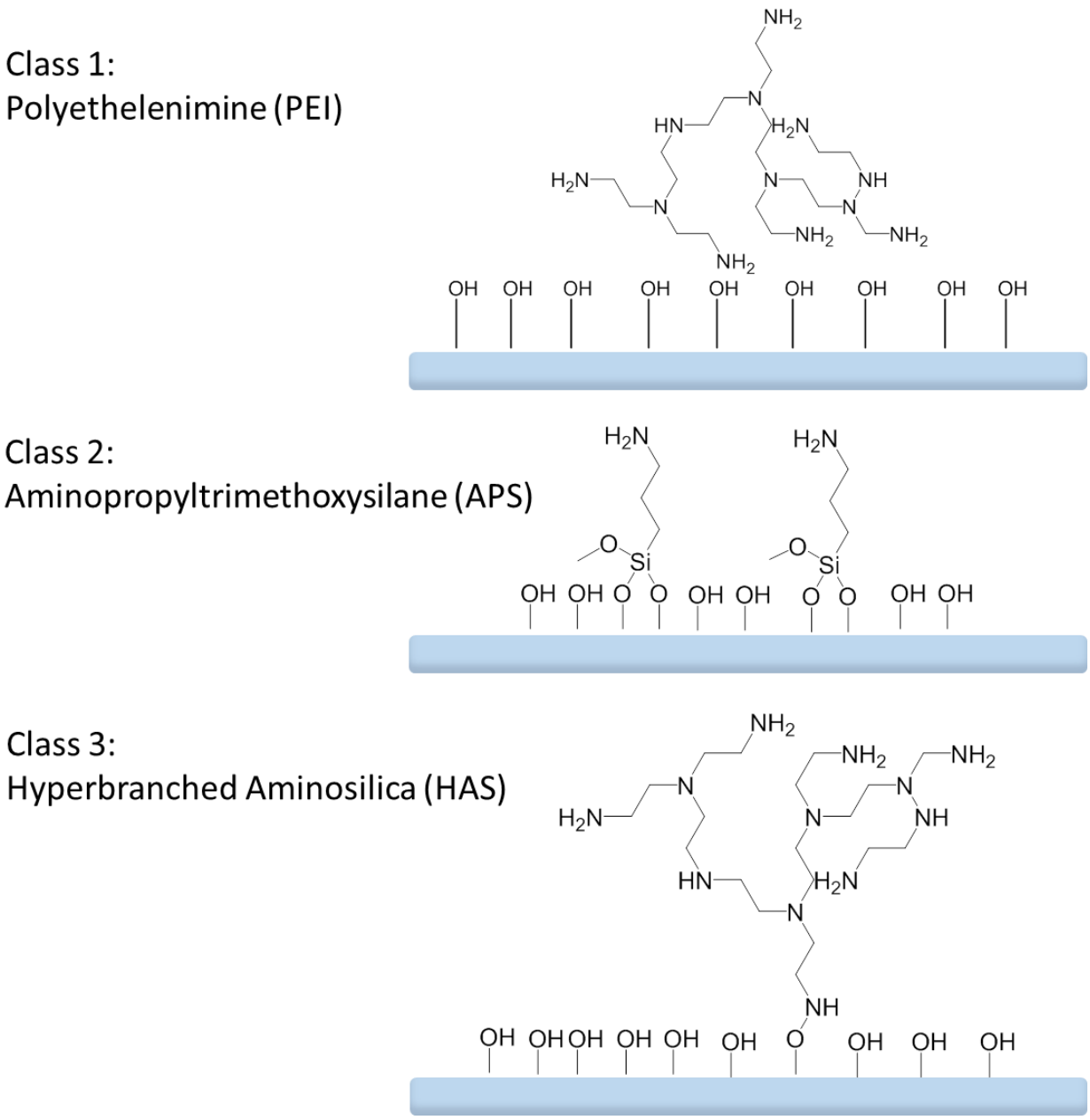

Figure 3.15 Depiction of the three classes of amine adsorbents. The blue rectangles represent the SBA-15 support.

When CO_2 and the amine groups react, there are four important possible reaction pathways, with the reactions for a primary shown in Figure 3.16.[4,24,55–63] The ^{13}C NMR chemical shifts listed in Figure 3.16 are solution phase chemical shifts for aqueous species that do not include the R groups.[64]

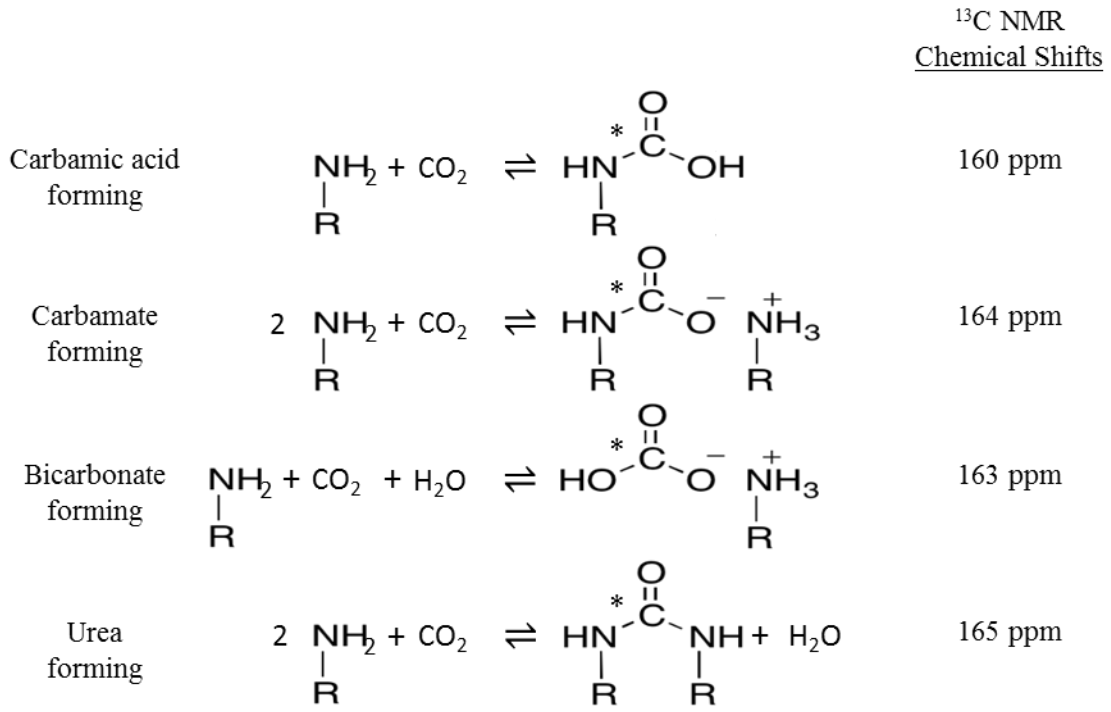

Figure 3.16 The reaction pathways for a primary amine and CO_2. The asterisk labels the ^{13}C enriched carbon that was introduced by the $^{13}CO_2$. The listed chemical shifts are solution state chemical shifts.[64]

The reaction pathways, in Figure 3.16, are analogous for primary and secondary amines, with exchanging an H atom on the nitrogen for an R group. Amine and CO_2 under dry conditions will react to form carbamate, carbamic acid, or urea; but urea will only form when the reaction is heated to 135 ^{o}C or higher under dry conditions.[65] When water is present, it is possible for the bicarbonate product to form. The tertiary amines can only react with CO_2 to form bicarbonate since there is no hydrogen atom to displace.

3.2.2 Class 1: Polyethyleneimine (PEI)

The class 1 PEI sample was reacted with 1 atm of $^{13}CO_2$ and monitored with *in situ* ^{13}C NMR. A representative spectrum is shown in Figure 3.17 and shows the $^{13}CO_2$ gas resonance and a broad resonance from chemisorbed CO_2.

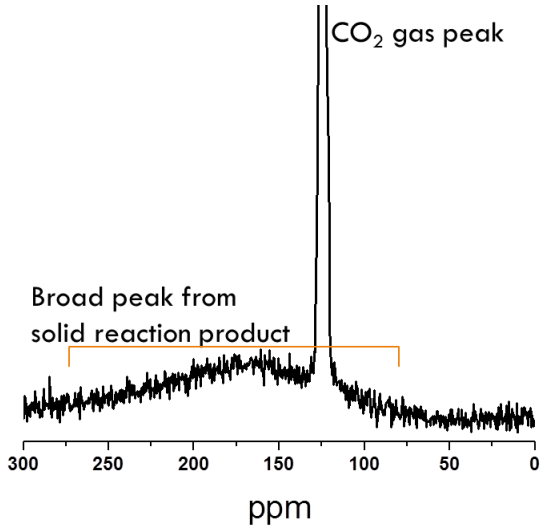

Figure 3.17 Static ^{13}C *in situ* NMR at 7 T of SBA-15-PEI reacted with $^{13}CO_2$(g).

This chemisorbed resonance is difficult to characterize in this static NMR probe since the dipolar interactions are not averaged to zero as in MAS experiments, and the sample has disorder in the polymer and support structure. The characteristic CSA pattern that was evident for other static ^{13}C NMR spectra is not observable due to the multiple interactions including: dipolar coupling to ^{1}H, ^{13}C, and ^{14}N; chemical shift anisotropy (CSA); and a dispersion of chemical environments. This means that identifying the chemisorbed product by its isotropic chemical shift would require either fitting to a structural model and/or MAS NMR techniques.

There are other ways to gain information about the adsorbed species than its isotropic chemical shift. In order to better understand the *in situ* chemisorbed species, spin lattice relaxation measurements were recorded with static ^{13}C NMR at a few different temperatures, seen in Figure 3.18.

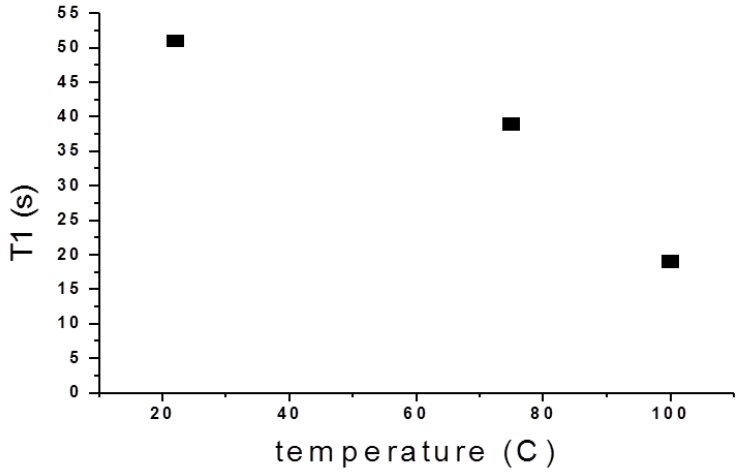

Figure 3.18 ^{13}C NMR T_1 relaxation time constant for the CO_2 adsorption product from reaction with SBA-15-PEI.

A single relaxation time was measured with static ^{13}C NMR for the broad resonance. The T_1 relaxation time of the broad resonance is more rapid at high temperatures, likely due to polymer mobility increasing with increasing temperature. This is corroborated by the linewidth decrease of the broad resonance with increasing temperature measured with static ^{13}C NMR, seen in Figure 3.19.

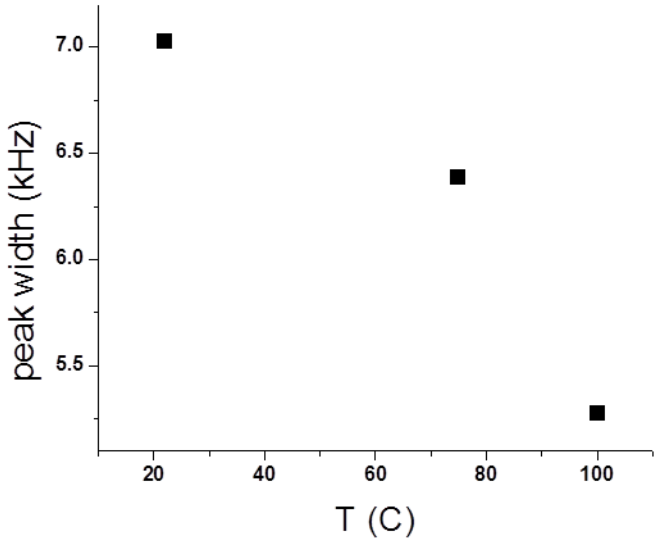

Figure 3.19 ^{13}C NMR peak width measured by the FWHM for the CO_2 adsorption product from reaction with SBA-15-PEI.

It is clear that in the *in situ* NMR probe, a chemisorbed species is present up to 95 ^{o}C which shows faster T_1 relaxation than the chemisorbed species at room temperature. Regardless of the temperature, the shape of the broad resonance was not able to be characterized only by traditional CSA broadening effects. The adsorbed product was not completely characterized by the *in situ* static ^{13}C NMR, though more studies on the temperature dependence of adsorption need to be done.

The product of the *in situ* chemisorption reaction is able to be studied *ex situ* with $^{13}C\{^{1}H\}$ CPMAS NMR, which can be seen in Figure 3.20, to identify the adsorption product by its isotropic chemical shift. Here the chemisorbed spectrum has a chemical shift of 163.2 ppm, and resonances for the polymer can be seen just below 50 ppm.

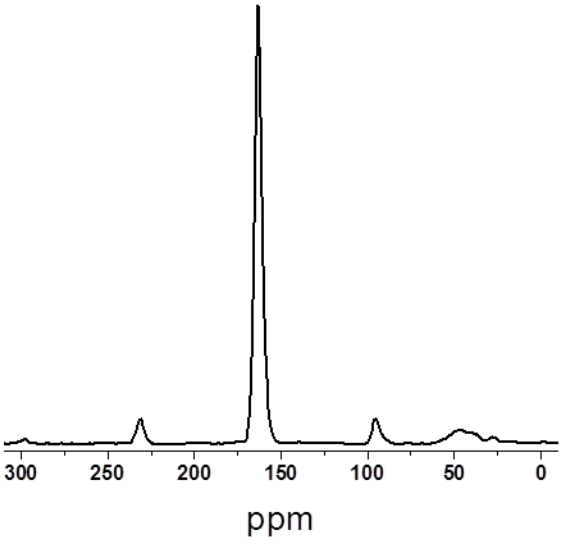

Figure 3.20 $^{13}C\{^{1}H\}$ CPMAS NMR recorded *ex situ* at 7 T of reacted SBA-15-PEI solids collected from the *in situ* reactor. (Sample rotation, ν_R= 5 kHz).

It is of note here that the peak assigned to CO_2 gas at 125 ppm is not in this spectrum since the CO_2 gas not adsorbed is released from the material during the transfer of the sample from the *in situ* reactor to an NMR rotor. The class 1 SBA-15-PEI material has a mixture of primary, secondary, and tertiary amines. The $^{13}C\{^{1}H\}$ CPMAS NMR shows a single resonance that is near bicarbonates aqueous chemical shift (reference in Figure 3.16), though the literature precedent for this reaction is for a carbamate product.[55–60,66–69] Further studies of amine adsorption materials with a hyperbranched structure were conducted on the class 3 material, SBA-15-HAS to try to elucidate the chemisorption product composition.

3.2.3 Class 3: Hyperbranched Aminosilica (HAS)

The class 3 HAS polymer was also studied with ^{13}C NMR *in situ* with 1 atm of $^{13}CO_2$ and is shown in Figure 3.21. In SBA-15-HAS, the *in situ* ^{13}C NMR data show a broad peak, assigned

to a chemisorbed CO_2, and a narrow resonance, assigned to a mixture of physisorbed CO_2 and gaseous CO_2.[9] The chemisorbed peak is similar to the broad peak seen in the class 1 PEI adsorbent material with characterization made difficult by the same factors (dipolar coupling, CSA, and structural variability of sites). The narrow resonance shows indications of physisorbed CO_2, as discussed in section 3.1, evidenced by a signal increase by a factor of 1.8 compared to CO_2 gas alone at the same pressure. The T_1 relaxation of the $^{13}CO_2$ resonance at 125 ppm is four times that of CO_2 gas alone which is another indicator of physisorption. There is an excess of CO_2 in the adsorption system, thus the narrow resonance must be a mixture of physisorbed CO_2 and gaseous CO_2. This indicates that SBA-15-HAS has multiple adsorption mechanisms, chemisorption and physisorption, with which to capture CO_2.

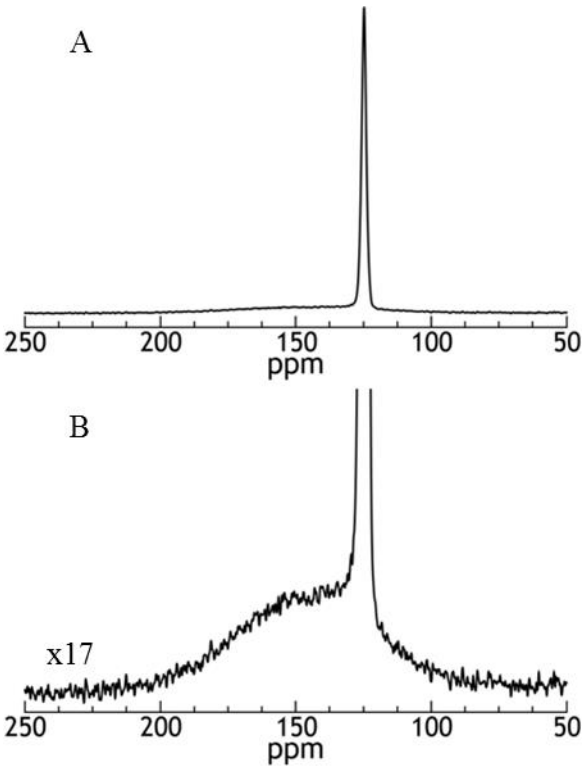

Figure 3.21 A) Static ^{13}C *in situ* NMR at 14 T of SBA-15-HAS reacted with $^{13}CO_2$(g) for 2 hours. B) Expanded scale showing the chemisorbed feature.

$^{13}C\{^{1}H\}$ CPMAS NMR, at 14 T, was used to observe the chemisorbed peak *ex situ*; this spectrum can be seen in Figure 3.22. In this spectrum, two ^{13}C NMR resonances are observed, one at 164.3 ppm with a width of 3.4 ppm and the other, a shoulder at 160.3 ppm with a width of 4.2 ppm.

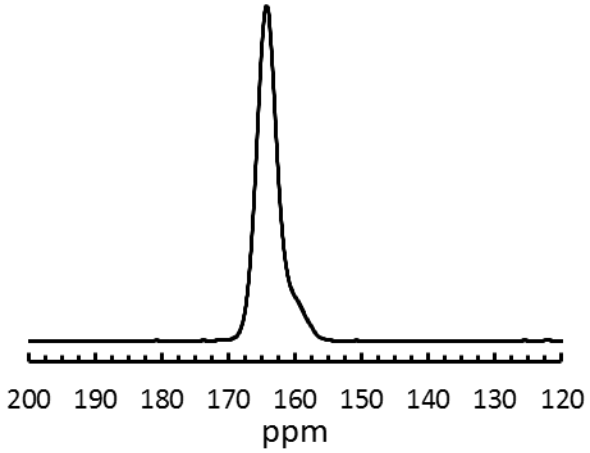

Figure 3.22 $^{13}C\{^{1}H\}$ CPMAS NMR recorded *ex situ* at 14 T of reacted SBA-15-HAS solids collected from the *in situ* reactor. (Sample rotation, ν_R= 10 kHz).

The resonance at 164.3 ppm lies near the same chemical shift of the adsorbed product from the PEI adsorption reaction. It is of note that this peak is broader than the chemical shift distribution of the possible products. The resonance at 160.3 ppm is a weaker shoulder and is assigned to carbamic acid, which is known to be minor adsorption product in solid sorbents.[55] This assignment was corroborated by the disappearance of this resonance from the NMR spectrum[55] when the sample was evacuated or allowed to "age" (the motivation for evacuating the sample will be discussed later), before subsequent spectra were acquired. The "aged" sample was allowed to sit in the atmosphere before recording the NMR spectrum. Carbamic acid does not persist under these conditions because it can convert to carbamate or desorb. The resonance at 164.3 ppm is more challenging to fully assign. Complicating matters is that the width of the

peak is such that multiple products could exist at the site of the observed resonance. Its linewidth of 3.4 ppm is greater than the chemical shift separation of the resonances of the possible products, even at high field (14 T). The presence of two resonances in this range already indicates that the adsorption process of CO_2 on HAS forms a mixture of products that can be distinguished with $^{13}C\{^1H\}$ CPMAS NMR.

Another method used to understand the reaction product at 164.3 ppm was the ^{13}C T_2relaxation acquired with a CPMAS echo, as discussed in Chapter 2.1.3, at 14 T of the "aged" sample. Figure 3.23 shows the decay of the ^{13}C NMR signal, as the natural log of the integrated signal intensity, due to T_2 relaxation. The decay of the signal intensity is plotted on a log scale which gives a linear decay for a single relaxation time, T_2. It is evident that there is a non-linear decay in the T_2 relaxation curve, which indicates multiple values for T_2, 14.7 ms and 76.9 ms, for the resonance. This result suggests that multiple species are present in the peak that appears at this chemical shift. The value for T_2 is dependent on the chemical environment of the ^{13}C nuclei. This means that it is expected that a quadrupolar ^{14}N nucleus bonded to the carbonyl carbon in carbamate will shorten the T_2 relaxation time compared to carbon species bonded to oxygen only (since 99.9% of oxygen is ^{18}O, which is "NMR-silent" since I = 0), as found in bicarbonate.

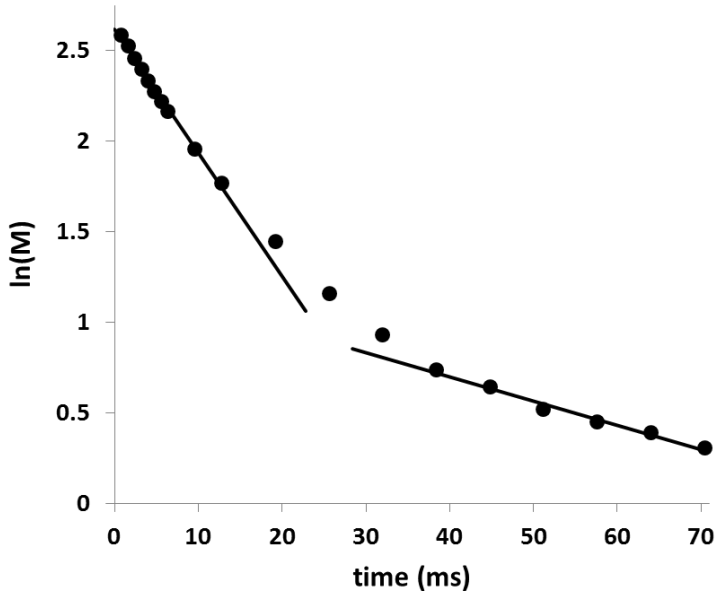

Figure 3.23 Cross-polarization Hahn spin echo measurements of T_2 (spin-spin) relaxation time curve of the resonance at 164.3 ppm in the $^{13}CO_2$ reacted SBA-15-HAS sample. Lines are fits of two possible linear relaxation regimes with T_2 relaxation times of 14.7 ms and 76.9 ms.

The $^{13}CO_2$ reacted SBA-15-HAS sample shows carbamic acid at 160.3 ppm in the spectrum and at least two other products contained within the resonance at 164.3 ppm that can be distinguished from the T_2 relaxation data. One possible way to differentiate the mixture of products, observed at 14 T, is to force the reaction down a given pathway. As seen in Figure 3.16, the carbamate reaction is a reaction pathway that is favored in dry conditions as opposed to the reaction pathway to bicarbonate which requires the presence of water. It is possible to run a "wet" reaction by bubbling the $^{13}CO_2$ through water prior to introducing it to the sample. Figure 3.24 shows the comparison of ^1H MAS NMR spectra, taken at 7 T, after a dry reaction and after a wet reaction.

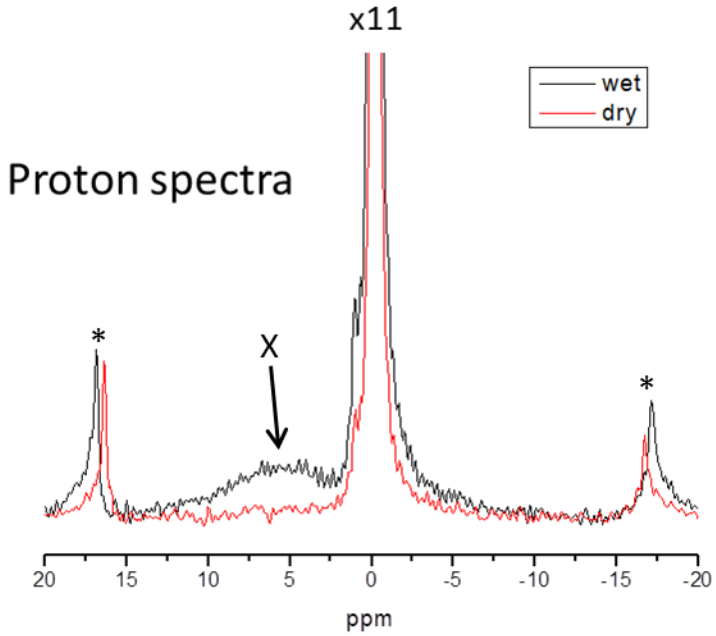

Figure 3.24 ^{1}H MAS NMR spectra at 7 T of $^{13}CO_2$ reacted SBA-15-HAS. The black curve shows a dry reaction environment and the red curve shows a wet reaction environment. Both spectra were spinning near 5 kHz, though the spinning sidebands are notably offset indicating a small difference in spinning speed.

There is an evident change in the proton spectrum due to the addition of water to the sample given by the additional feature centered at 6 ppm, noted with an "x", which is assigned to the added water. Figure 3.25 shows a comparison of a dry CO_2 reaction and a wet CO_2 reaction with $^{13}C\{^{1}H\}$ CPMAS NMR.

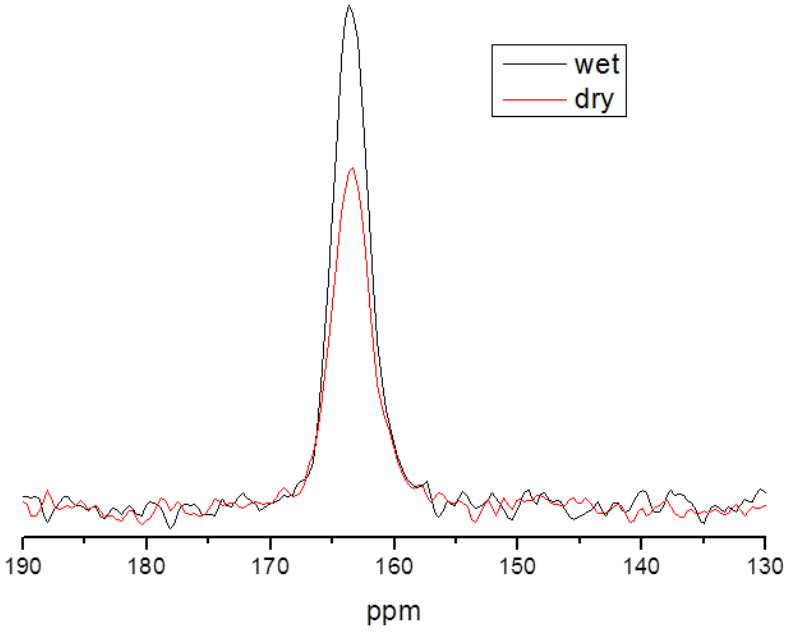

Figure 3.25 $^{13}C\{^{1}H\}$ CPMAS NMR recorded *ex situ* at 7 T of reacted SBA-15-HAS solids collected from the *in situ* reactor. The black curve shows a dry reaction environment and the red curve shows a wet reaction environment.

These reactions should force the adsorption reaction to go down specific pathways. The wet reaction shows slightly more ^{13}C NMR signal intensity from the adsorbed resonance for identical experimental conditions, though the ^{13}C chemical shift is almost the same. The contact time curves with CPMAS for the chemisorbed $^{13}CO_2$ shown in Figure 3.25 were recorded and shown in Figure 3.26; these also show little difference between the dry and wet reactions. This data leads to the conclusion that the carbon sites being probed and their surroundings are nearly identical.

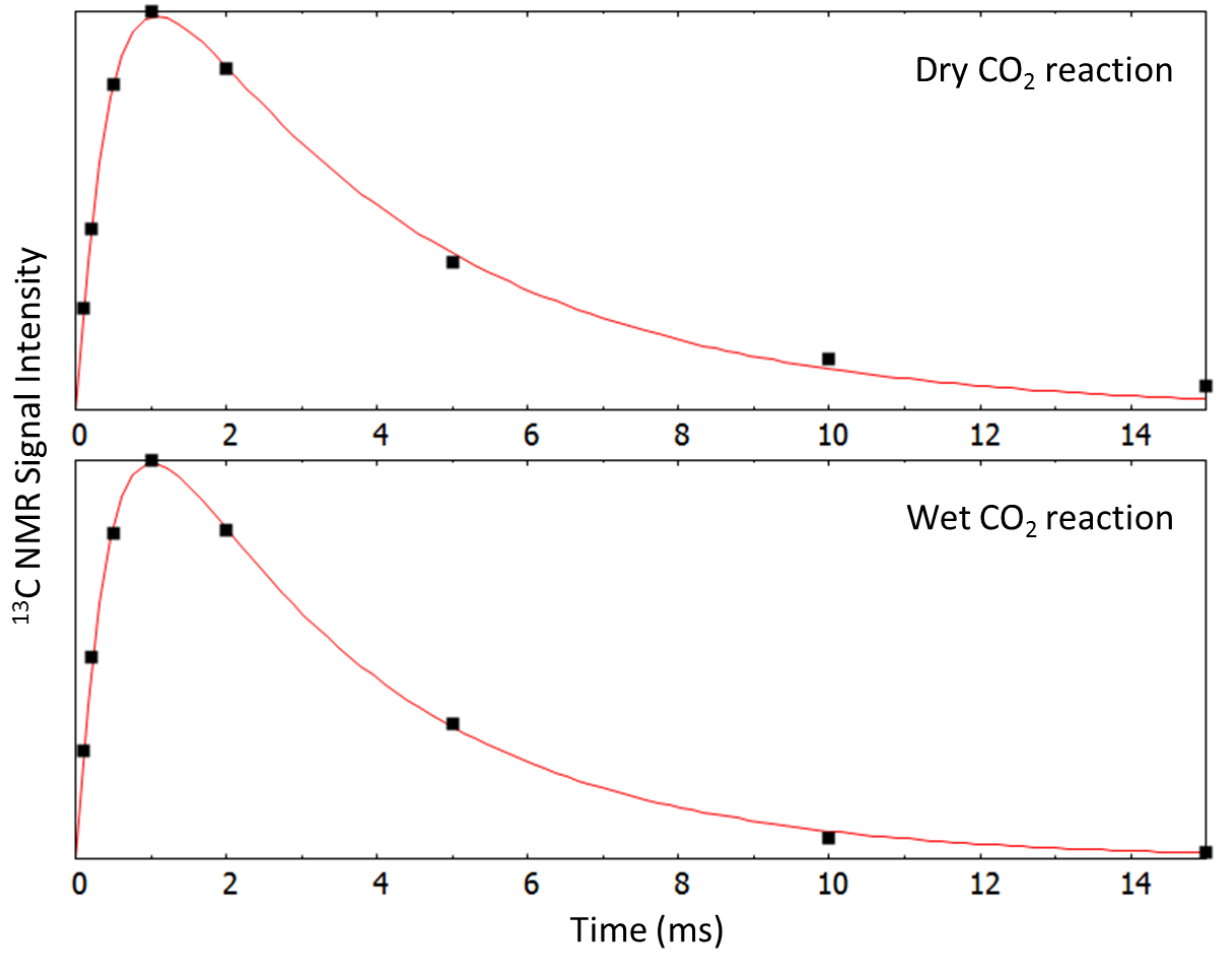

Figure 3.26 $^{13}C\{^1H\}$ CPMAS NMR contact time curve of the dry CO_2 and amine reaction (top) and wet CO_2 and amine reaction (bottom)

The dipolar dephasing CPMAS experiments, described in Chapter 2.1.3, were measured on the wet reaction sample and the dry reaction sample. These spectra are shown in Figure 3.27.

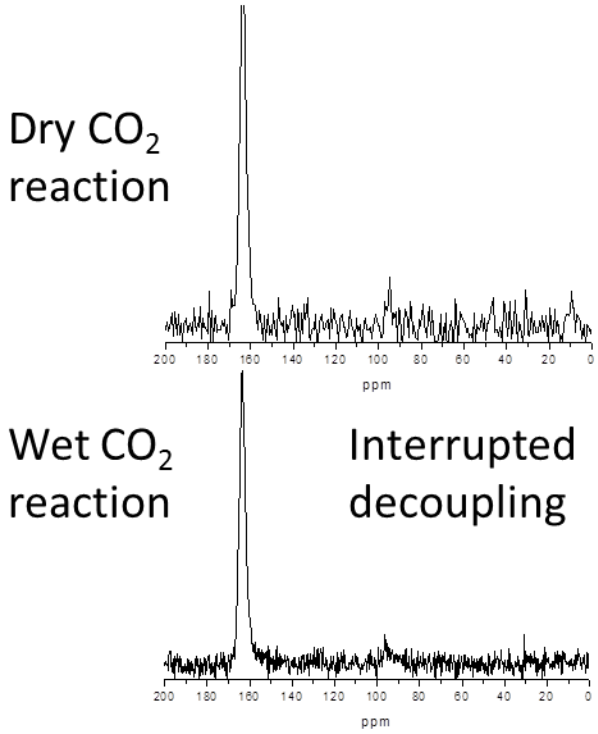

Figure 3.27 $^{13}C\{^1H\}$ CPMAS NMR interrupted decoupling experiment of the dry CO_2 and amine reaction (top) and wet CO_2 and amine reaction (bottom)

Here both signals decay at approximately the same rate. Since the contact time curves and dipolar dephasing experiments are similar, both indicate that the proton bath around the ^{13}C nuclei is relatively equivalent. For our possible products, this is unsurprising, as both carbamate and bicarbonate have a closest proton at 2 bond lengths away.

The data acquired on the reaction products of the wet reaction and the dry reaction show little differences between the two. It is known that SBA-15-HAS is hydrophilic,[8] so there is the possibility that water is present on the polymer and support structure which would cause the same products to be formed even after the bake out process. It is also possible that techniques used are not capable of distinguishing the various products that can form. The data have all been acquired from $^{13}C\{^1H\}$ CPMAS techniques that rely on the ^{13}C-^1H dipolar coupling to nearby

protons. Therefore, the distance of the $^{13}CO_2$ reaction product to the nearby protons is relevant in the analysis of these data. When looking at the structure of carbamate and bicarbonate, it is clear that each product has no directly-bonded protons, and each has the closest hydrogen two bonds away. Thus, the ^{13}C-^{1}H dipolar coupling will be similar in these two products and will not allow CPMAS techniques based on this coupling to easily distinguish between the structures. As seen above, it is difficult to differentiate the possible products of the amine chemisorption reactions by traditional methods. Low field NMR is a possible technique that can give extra information about the chemisorption products in order to identify which reaction pathways are preferred. The low field NMR experiments take advantage of dipolar coupling between ^{13}C, dominantly from the carbon dioxide, and ^{14}N, from the amine.[70–75] As discussed in the NMR introduction, every spin is dipolar coupled to every other non-zero spin in the system. The pulse sequence utilizes the coupling between ^{13}C and ^{1}H with a typical $^{13}C\{^{1}H\}$ CPMAS NMR experiment. The ^{13}C atoms are also coupled to the ^{14}N atoms within the sample, and this coupling has an effect on the ^{13}C NMR spectrum, which will be discussed below.

The samples are reacted with $^{13}CO_2$ which ensures that the carbon atoms of interest are all ^{13}C instead of ^{12}C. On the other side of this coupling, the ^{14}N isotope of nitrogen is 99.6% abundant. Therefore, in our chemisorbed system, we can assume that every CO_2-amine pair has a ^{13}C-^{14}N dipolar coupled pair of spins. The pairs will likely exist as either a carbamate species or bicarbonate species, which have different ^{13}C-^{14}N dipolar coupling due to the bonding environment around the carbonyl carbon. The carbonyl carbon of the carbamate species has a directly bonded nitrogen while the bicarbonate carbonyl carbon has three directly bonded oxygen atoms.

The ^{13}C-^{14}N dipolar coupling induces a splitting in the ^{13}C NMR resonance. [70–75] When there is only one magnetically-equivalent carbon site in the sample, a single peak is expected in the ^{13}C NMR spectrum. However, when the single magnetically-equivalent carbon site is bonded to a ^{14}N nucleus, the ^{13}C-^{14}N dipolar coupling exhibits as a splitting in the ^{13}C NMR resonance. The dipolar interaction allows the second-order quadrupolar effects from the I=1 ^{14}N nucleus to be transferred to the coupled I= $\frac{1}{2}$ ^{13}C nucleus.[70] Typically, MAS is utilized in solid-state NMR to average to zero the dipolar interactions, which works well for systems such as a ^{13}C coupled to another spin-1/2 nucleus. In this ^{13}C-^{14}N system, the ^{14}N electric field gradient (EFG), which is determined by the electron distribution around the quadrupolar nucleus, does not allow the dipolar coupling to average to zero. The quantization axis of the ^{14}N is only partially aligned with the EFG, which is fixed relative to the sample spinning axis. It is also partially aligned with the magnetic field axis, which is fixed in the laboratory frame. Due to this partial alignment, as the sample rotates with MAS, the ^{14}N quantization axis wobbles which prevents the ^{13}C-^{14}N dipolar coupling from averaging to zero.[70] The ^{13}C-^{14}N dipolar coupling is thus present in the ^{13}C NMR spectrum as a splitting in the ^{13}C resonance. To take advantage of the dipolar coupling, this experiment needs to occur at low magnetic fields (typically less than 4.7 T) because the interaction is inversely proportional to B_o.[70] Therefore, at high magnetic fields, a single carbon site will be observed as a single ^{13}C resonance (but broader than other ^{13}C resonances) while at low magnetic fields the splitting is observable.

As was discussed above, the extent of splitting is inversely proportional with B_o. The extent of splitting is also dependent on the strength of the ^{13}C-^{14}N dipolar coupling and the ^{14}N EFG. The dipolar coupling strength (as discussed in Chapter 1) is dependent on the ^{13}C-^{14}N internuclear distance. The ^{14}N EFG is defined by the quadrupolar asymmetry parameter (η) and the Euler

angles (α and β) which will dependent on the electronic environment of the ^{14}N nucleus.[70,72] Therefore, the atoms directly bonded to the nitrogen, that help determine its EFG, will also affect the extent of splitting in the ^{13}C NMR spectrum.

To be able to assign two NMR peaks to a single ^{13}C site with detectable ^{13}C-^{14}N dipolar coupling, the relative intensities of the split peaks can aid in the assignment. The split peaks are known to exhibit a 2:1 area ratio with the center of mass of the two peaks being equal to the isotropic chemical shift.[70] This interaction is not specific to ^{13}C-^{14}N, but can be seen in other I= $\frac{1}{2}$ spins that are coupled to quadrupolar nuclei such as the ^{119}Sn and $^{35/37}Cl$ pairs, a ^{29}Si and ^{14}N pair, and the ^{31}P and $^{63/65}Cu$ pairs.[70]

It is known that carbamate can form as the adsorption product on both primary and secondary amines. Based on unpublished work from our lab, it was calculated that a primary amine carbamate and a secondary amine carbamate have different Euler angles from the ^{14}N EFG. This means that even different carbamate groups will give a different NMR spectrum at low fields. The change in extent of ^{13}C-^{14}N dipolar interaction could cause the two sites to split differently due to the alignment of the ^{14}N EFG. Further studies will need to be done to determine if the class of amine polymer also affects the dipolar coupling of ^{13}C-^{14}N.

Figure 3.28 shows an example of the splitting that results from ^{13}C-^{14}N dipolar coupling for a reference sample of ammonium carbamate, $(NH_4)(H_2NCO_2)$, at 3 T. This molecule has a single carbon moiety that is covalently bonded to the nitrogen, giving the opportunity to probe the coupling. The chemically-unique carbon site in ammonium carbamate yields two peaks in the ^{13}C NMR spectrum that are split by 5.6 ppm and have approximately the expected 2:1 area ratio.

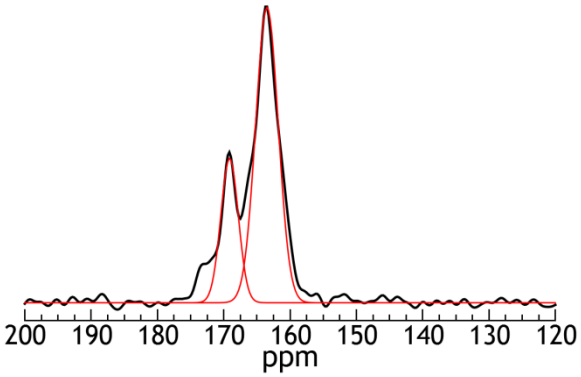

Figure 3.28 $^{13}C\{^{1}H\}$ CPMAS NMR (ν_R= 3.8 kHz) at 3 T of the single carbon site in ammonium carbamate ($(NH_4)(H_2NCO_2)$), showing the splitting and the characteristic peak ratio of the resonance due to ^{13}C-^{14}N dipolar coupling. The experimental spectrum is in black, and the fits of both peaks are in red.

The $^{13}C\{^{1}H\}$ CPMAS NMR experiment at 3 T has also been recorded on the $^{13}CO_2$ reacted Class 3 SBA-15-HAS sample, shown in Figure 3.29. If the adsorption product is only carbamate, the expected resonance should exhibit a splitting from the ^{13}C-^{14}N dipolar coupling, like ammonium carbamate. If the product is only bicarbonate, a single resonance is expected.

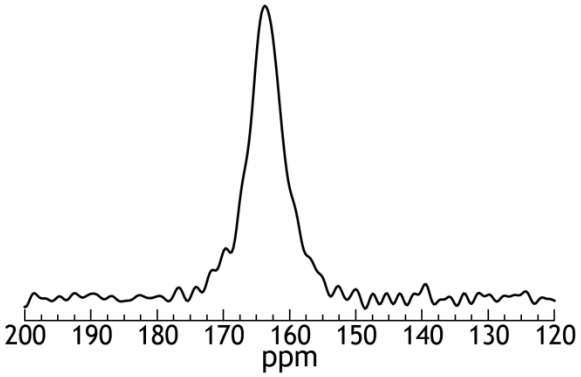

Figure 3.29 $^{13}C\{^{1}H\}$ CPMAS NMR (ν_R= 3.8 kHz) at 3 T of the reacted SBA-15-HAS. The chemisorbed product resonance has a FWHM of ~5.2 ppm. 1024 transients were recorded.

This spectrum has a resonance centered at 163.6 ppm and a FWHM of 5.2 ppm. Upon closer inspection, it appears that the central peak is flanked by two small shoulders, one on each side. Carbamic acid (~160 ppm) has been ruled out because this sample was allowed to age before the

data were acquired. It is of note that the two shoulders are spread by approximately the same amount as the split peaks in ammonium carbamate, which suggests that they are due to a carbamate species. The center of this spectrum, though, has the appearance of an unsplit signal that obscures the presence of the split peak arising from carbamate. This dominant, unsplit resonance is attributable to a second adsorption product that could be a bicarbonate species or a second carbamate species that has a different set of Euler angles and a different EFG. As before, the linewidths of all of the peaks are large enough to possibly obscure multiple peaks if present in this spectrum.

The literature precedent for adsorption reactions between CO_2 and supported amines suggests that the dominant product should be carbamate over bicarbonate.[55–60,66–69] Some of these studies used analytical techniques that required a vacuum (such as NEXAFS),[69] and some utilized a vacuum to study desorption.[23–25,65,76–80] A common technique for understanding amine adsorption reactions is FTIR, where reports on the extinction coefficients of carbamate and bicarbonate which can affect its ability to detect both products equally have been scarcely reported. Due to this literature precedent, a reacted SBA-15-HAS sample was evacuated to ~10 mTorr at 23 ^{o}C prior to recording the NMR spectrum. Figure 3.30 shows the $^{13}C\{^{1}H\}$ CPMAS spectrum of the CO_2 reacted SBA-15-HAS material at 3 T.

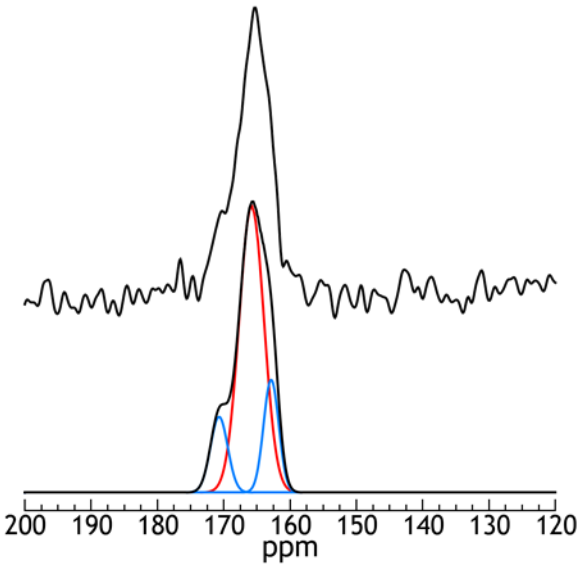

Figure 3.30 $^{13}C\{^{1}H\}$ CPMAS NMR at 3 T of the reacted SBA-15-HAS after evacuating the reacted sample for 31 hours. 72,000 transients were recorded (ν_R= 3.8 kHz). The experimental spectrum is in black (top), the overall fit (bottom) is in black, the peak fits for carbamate are blue, and the peak fit for bicarbonate is red.

The evacuation of the sample caused a significant diminution of the NMR signal, specifically the central resonance centered at 163.6 ppm, despite acquiring 70 times more transients. The spectrum still shows the presence of multiple peaks, a central peak with more prominent shoulders, that must be tightly bound adsorption products.[59] The central resonance is centered at 165.8 ppm, which is at a higher frequency than previous spectra, and the shoulders are separated by 4.9 ppm. This obvious shoulder in the spectrum confirms the findings of a mixture of products in this adsorption reaction. Table 3.1 has the chemical shifts and linewidths of the peaks observed with $^{13}C\{^{1}H\}$ CPMAS NMR at 3 T.

Table 3.1 ^{13}C NMR chemical shifts and peak widths at 3 T.

	^{13}C δ_{iso} (ppm)	FWHM (ppm)	Assignment
ammonium carbamate	169.1	3.1	carbamate
	163.5	4.0	
SBA-15-HAS reacted with CO_2	163.6	5.2	mixture
SBA-15-HAS reacted with CO_2 and evacuated	170.7	3.1	mixture
	162.9	2.7	
	165.8	4.4	

Previous reports indicate that carbamate is the favored products in dry conditions and will form with primary and secondary amine groups through a zwitterionic mechanism.[34] To form a bicarbonate product, the reaction requires the presence of water to act as a free base and can form on all three types of amine groups including tertiary.[34] The HAS polymer contains a mixture of primary, secondary, and tertiary amine sites that are able to adsorb CO_2. This allows the adsorption reaction to progress down any possible reaction pathway. To form a mixture of products, it is specifically useful to have tertiary amines present which are known to catalyze the formation of bicarbonate species.[61,81] Water is expected to be present on the surface of these solid adsorbents because SBA-15 and the aminosilica polymer are typically hydrophilic.[8] Even after the routine evacuation of the sample at 95 ^{o}C, the hydrophilic materials could keep some

water within the pores. It is known that the mesoporous SBA-15 retains some water due to the abundant hydroxyl groups on the silicate surface. The mixture of amine units and the likely presence of water indicates that all of the possible reaction pathways are available in this CO_2 adsorption system.

Furthermore, it is thought that bicarbonate forms much more slowly than carbamate in the adsorption reactions.[4] It was recently reported that with long exposure times of humid CO_2, an APS modified SBA-15 adsorbent gave evidence for a bicarbonate adsorption product with FTIR.[82] Most of the previous literature reports adsorption times on the order of several hours, which could be long enough to only form carbamate species.[57,83] Even under humid conditions, the formation of bicarbonate could take longer, especially in materials that have a high density of amines. Previous studies on amine adsorbents also typically use low partial pressures of CO_2 during the adsorption. It is possible that when a low partial pressure of CO_2 is used, carbamate is the preferred product due to its 2:1 amine:CO_2 ratio. When higher partial pressures are used during the adsorption time, the reaction will shift to form more bicarbonate and carbamic acid which both have a 1:1 amine:CO_2 ratio.[24,61] So, when high CO_2 concentrations and long reaction times are used, as was done in the studies presented here, adsorption species other than carbamate become possible on the SBA-15-HAS material.

The adsorption reactions discussed here are likely to form a mixture of adsorption products since the process used a mixture of amines, likely have the presence of water, used high CO_2 concentrations, and used long reaction times. The data support that a mixture of adsorption products was formed on the sorbent surface, though the exact identification of this mixture has not been concluded. As discussed above, the mixture could consist of carbamate species and bicarbonate species. In this case, the low field $^{13}C\{^1H\}$ CPMAS NMR data would be assigned

as a central resonance from bicarbonate with the two shoulders assigned to the carbamate species. It can also not be ruled out that the adsorption products are a mixture of carbamate species. In this scenario, the NMR data at 3 T would have the central resonance and the pair of split peaks both assigned to separate carbamate species. The NMR resonances could arise from a carbamate that formed on a primary amine and a carbamate formed on a secondary amine. From preliminary modeling, these two types of amines have a different set of Euler angles which would change the extent of the splitting of the NMR resonance due to ^{13}C-^{14}N dipolar coupling. There have also been reports of a surface bound carbamate species in which the carbamate is charge balanced by a surface Si-OH_2^+ group instead of a second amine group.[57,59] This carbamate species has been found to be very stable and able to persist under vacuum. The surface bound carbamate forms in a 1:1 amine:CO_2 ratio which would give the opportunity for a significant amount of this species to form as a second carbamate structure in the adsorption product mixture. Since the surface-bound carbamate species is so stable under vacuum, this could explain why the shoulders present in the unevacuated 3 T NMR spectrum become more pronounced after the sample has been evacuated. It is possible that this carbamate species also has a different orientation of the ^{14}N EFG, which would lead to a different extent of splitting in the ^{13}C NMR spectrum.

Irrespective of the exact scenario which produces the product mixture, it is clear that a mixture of CO_2 adsorption products forms on the SBA-15-HAS material. Upon evacuation, the more stable chemisorption products remain, which seems to favor carbamate products. To fully identify the mixture of adsorption products on this material, more experimental and computational work needs to be done. Nevertheless, $^{13}C\{^1H\}$ CPMAS NMR techniques, including T_2relaxation data and low field NMR, are able to distinguish a mixture of adsorption products.

3.2.4 Class 2: Primary, Secondary, Tertiary Amines

The class 2 amine adsorbents each possess a single type of amine, giving an opportunity to deconvolute some of the differences that can be seen in the hyperbranched polymers. 3-aminopropyltrimethoxysilane (APS) is used as a class 2 adsorbent and has only primary amines. (N-methylaminopropyl)-trimethyoxysilane (MAPS) is the secondary amine-only class 2 adsorbent, and (N,N-dimethylaminopropyl)-trimethoxysilane (DMAPS) is a tertiary amine-only class 2 adsorbent.

Preliminary studies on these materials have been done with $^{13}C\{^{1}H\}$ CPMAS NMR at low field (2.4 T). The tertiary amine, DMAPS, gave no signal for adsorbed CO_2 because there was no water present during the reaction. The primary amine and secondary amine materials show no identifiable splitting due to the ^{13}C-^{14}N dipolar coupling; the spectra can be seen in Figure 3.31.

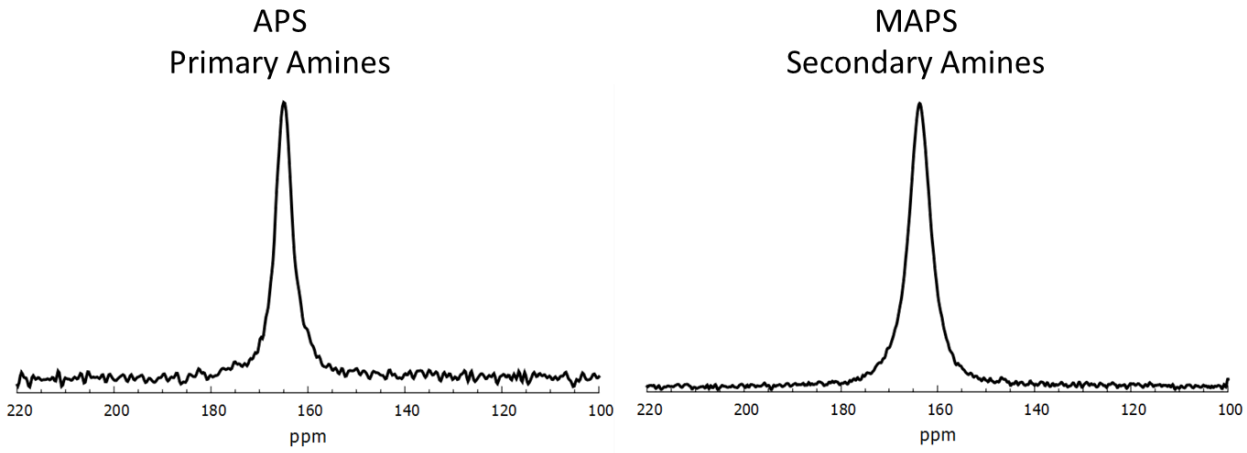

Figure 3.31 $^{13}C\{^{1}H\}$ CPMAS NMR at 2.35 T $^{13}CO_2$ reacted class 2 adsorbents supported on SBA-15. (ν_R= 4.5 kHz). APS with primary amine is on the left and MAPS with secondary amines is on the right.

The key difference in these two spectra is the FWHM, which is different for each as seen in Table 3.2. With no change in coupling, it would be expected that these samples would have a

similar FWHM when recorded with the same conditions, as evidenced in the FWHM at high field (7 T). The change in linewidth at low field must then be due to the change in the ^{13}C-^{14}N dipolar coupling even if not observed as a peak splitting.

Table 3.2 The ^{13}C NMR chemical shift and linewidth of class 2 amine adsorbents

	^{13}C NMR Chemical shift (ppm)	FWHM (ppm) Low Field (2.4 T)	FWHM (ppm) High Field (7 T)
Primary amine (APS)	164.9	3.5	3.8
Secondary amine (MAPS)	163.7	5.2	4.0

As mentioned previously, preliminary simulation results from our lab indicate that the splitting of the individual carbamate sites that form on primary or secondary amines are different. The data here indicate that the splittings are small due to the Euler angles of the ^{14}N EFG. This means it is possible that the effect of the dipolar coupling is only observed as a broadening of the NMR resonance for the class 2 adsorbents. This broadening then shows that the different amine sites indeed show a different splitting due to the dipolar coupling and are able to be differentiated by $^{13}C\{^{1}H\}$ CPMAS NMR at low field.

Chapter 4: Carbon Mineralization

Carbon sequestration is one solution for storage of captured CO_2. One possible way to sequester CO_2 is underground storage, where the CO_2 is buried as a supercritical fluid in the brine layer resevoir.[7] This layer is underneath impermeable rocks, known as "caprocks", which includes sandstones and ultramafic rocks in the earth's mantle.[26] The key to this storage method is the permanency of which the CO_2 stays in the dissolved supercritical state and location it was originally injected.[26,31,84,85] As long as the CO_2 is not able to break through the caprock layer or migrate underground to another location, underground storage can be a solution for carbon sequestration. Another similar method to sequester CO_2 is to introduce the supercritical fluid to a site that, while also containing a caprock layer, has minerals available for carbon mineralization reactions to occur with the CO_2.[7,30,36,84,86–93] In this scenario, the carbon dioxide acidifies the brine solution, which dissolves the reactive minerals present. The CO_2 and divalent cations (i.e. Mg^{2+}, Fe^{2+}, Ca^{2+}) released from the dissolved mineral react in the solution to form carbonate minerals that precipitate out of solution.[7,90,94] Once the CO_2 has reacted to form a carbonate mineral, it is not possible for the CO_2 to escape or migrate, making carbon mineralization a truly permanent storage solution.

Most underground sites have little of the reactive minerals necessary for carbon mineralization, therefore, selecting sites wisely is important. Olivine, pyroxene, and feldspar are examples of the minerals found at carbon sequestration sites that could be utilized as a source for carbon mineralization.[30,95] These minerals are candidates because they have divalent cations such as Mg^{2+}, Fe^{2+}, and Ca^{2+} in their crystal structures. Olivine, $(Mg,Fe)_2SiO_4$, contains a mixture of magnesium and iron, as the source for divalent cations, and can be characterized by the ratio of the magnesium endmember (forsterite, Mg_2SiO_4) to the iron endmember (fayalite, Fe_2SiO_4) in

the mineral. Feldspar minerals ($KAlSi_3O_8$ – $NaAlSi_3O_8$ – $CaAl_2Si_2O_8$) are characterized by the amount of each mineral endmember (listed in parentheses), such as anorthite ($CaAl_2Si_2O_8$) which has Ca^{2+} and Al^{3+} as the cations. Pyroxene minerals [$XY(Si,Al)_2O_6$] can be characterized by the X and Y ions. X typically includes calcium, sodium, iron (II), and magnesium. Y is a smaller ion, which typically includes aluminum, iron (III), magnesium, or manganese.

The reaction conditions at carbon mineralization sites are far from STP conditions since the sequestration sites are far underground, typical depths greater than 500 m.[29,96] Typical sites will have temperatures between 50 and 100 ^oC and pressures of up to 100 atm. CO_2 has a critical point of 31 ^oC and 72 atm, thus at these conditions, CO_2 will exist as a supercritical fluid, as seen in Figure 4.1. The pressure and temperature conditions as well as the pH will change the mixture of product minerals.[88,90–92,94,97]

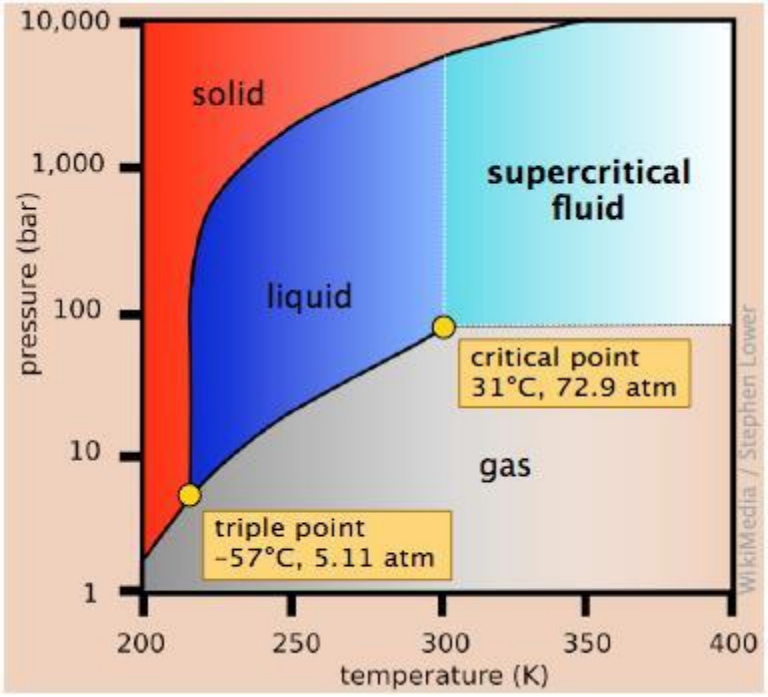

Figure 4.1 Phase diagram for CO_2. (Source: http://chemwiki.ucdavis.edu/Textbook_Maps/General_Chemistry_Textbook_Maps/Map%3A_Lower's_Chem1/07%3A_Solids_and_Liquids/7.5%3A_Changes_of_State#Phase_map_of_Carbon_dioxide)

In our lab, we have developed specialized NMR hardware to study reactions *in situ* at the conditions relevant to CO_2 mineralization.[36,98] The technique allows the observation of solid, liquid, gas, and supercritical phase CO_2 signals simultaneously while the reaction is at sequestration-relevant temperature and pressure. In order to replicate carbon mineralization reactions in this *in situ* system, a slurry of reactant mineral powder in water is made to model the underground system, as depicted in Figure 4.2.

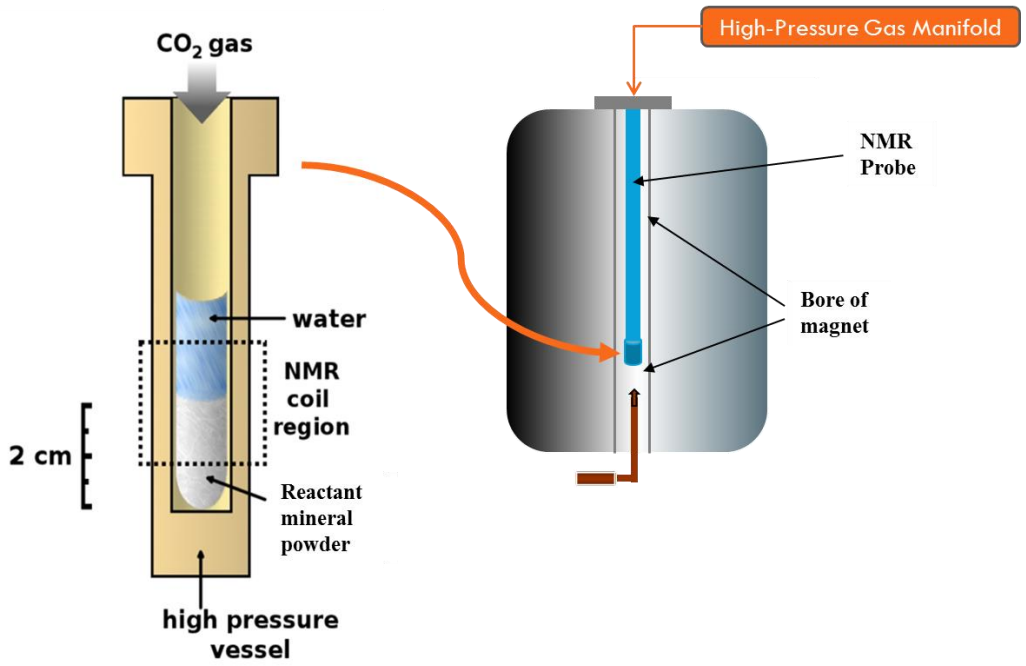

Figure 4.2 Representation of the *in situ* NMR apparatus.

The slurry is allowed to settle, such that the reaction vessel contains the wet mineral with a layer of water on top; the vessel is in the NMR probe and surrounded by a NMR coil for RF signals. The probehead is then heated and pressurized with CO_2 in the reaction chamber to mimic the underground sequestration conditions. The reactions in the specialized NMR hardware have typically been conducted with forsterite as the reactant mineral. Forsterite is the magnesium endmember of olivine, which is a good candidate for NMR studies because paramagnetic iron (Fe^{2+}) species are not present. NMR is a powerful technique to study carbon mineralization reactions because of its ability to distinguish relatively small structural differences.[36,99–105] The products of mineralization reactions are typically a mixture of products as well as a mixture of amorphous and crystalline species.[100,106,107]

4.1 Reactions of CO_2 and Forsterite (Mg_2SiO_4)

The carbon mineralization reactions contain a series of reaction equilibria seen in Figure 4.3.

$$CO_{2(sc)} \rightleftharpoons CO_{2(aq)} \quad (1)$$

$$CO_{2(aq)} + H_2O \rightleftharpoons HCO_3^- + H^+ \rightleftharpoons CO_3^{2-} + 2\,H^+ \quad (2)$$

$$Mg_2SiO_{4(s)} + 4\,H^+ \rightleftharpoons 2Mg^{2+} + SiO_{2(aq)} + 2\,H_2O \quad (3)$$

$$Mg^{2+} + CO_3^{2-} \rightleftharpoons MgCO_{3\,(s)} \quad (4)$$

Figure 4.3 Reactions of CO_2 and Forsterite

This series of reactions starts with the supercritical CO_2 dissolving into water (1), which sets up the well-known equilibrium between CO_2, HCO_3^-, and CO_3^{2-} (2). As the equilibrium progresses, the acidified solution can dissolve minerals that are surrounding the solution which frees the necessary divalent cations for carbon mineralization (3). In Scheme 4.1, the mineral is forsterite which has the reactive Mg^{2+} cation. Once the solution contains sufficient carbonate and magnesium ions, and the pH increases to at least 6, these precipitate out of solution as magnesium carbonates (4). Magnesite, $MgCO_3$, is the thermodynamic minimum product and is shown in Figure 4.3. This is a complicated set of reaction equilibria where the pH, temperature, time, and concentration affect the results of the extent of reaction for each step.[88,98,108–110]

The magnesium carbonate product can precipitate as other metastable magnesium carbonate products; examples can be seen in Figure 4.4.[36,88,94,99,111] These minerals have hydroxide groups, bicarbonate groups and waters of crystallization within the crystal structure. The products of mineral carbonation that we have studied include hydromagnesite, dypingite, and nesquehonite, which have been characterized previously.[36,99]

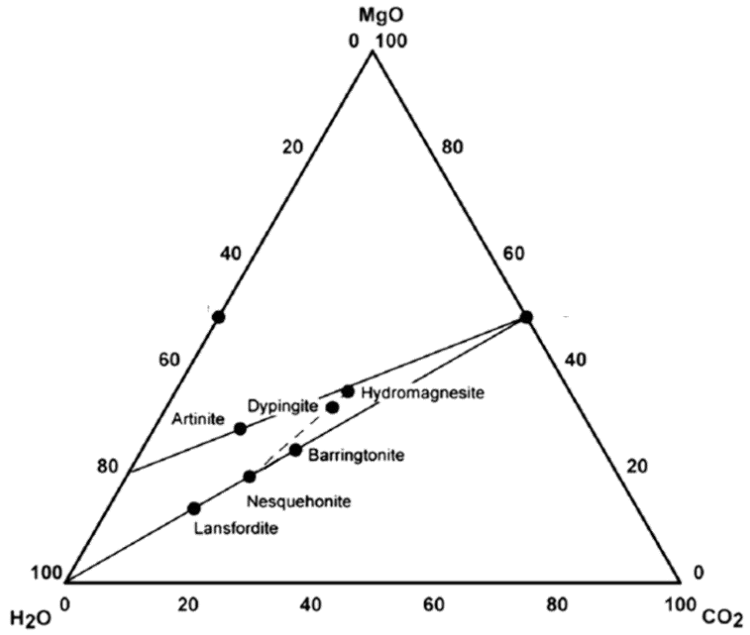

Figure 4.4 Ternary phase diagram for the composition of magnesium containing minerals separated by the amount of MgO, CO_2, and H_2O in the structure.

Figure 4.5 shows representative static ^{13}C NMR spectra of a forsterite and CO_2 reaction monitored with *in situ* ^{13}C NMR at 8.2 T. The reaction was run at conditions of 80 ^{o}C and 95 atm of CO_2 for 24 days (576 hrs).

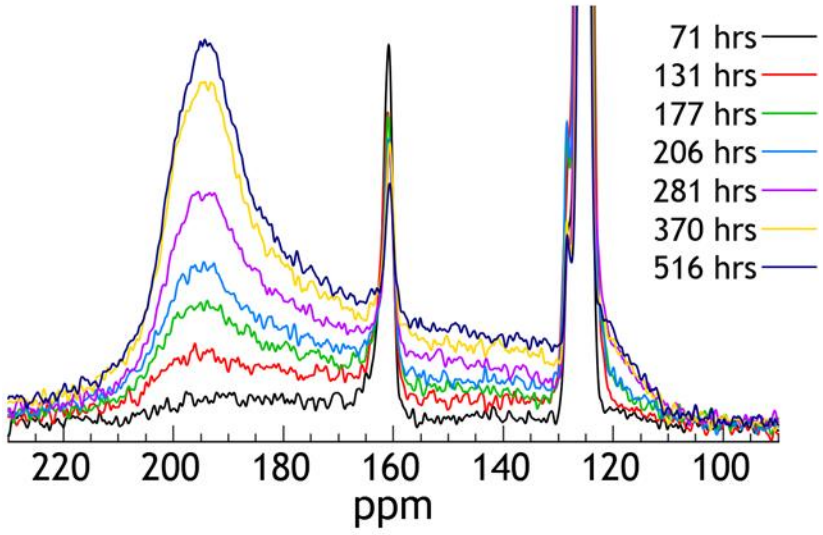

Figure 4.5 ***In situ*** **static ^{13}C NMR at 8.2 T of a forsterite in water reaction with CO_2. Reaction at conditions of 80 ^{o}C and 95 atm CO_2. Each spectrum is at the time point listed in the key.**

After 71 hours (black spectrum), a peak for CO_2 (125 ppm) and a peak for bicarbonate (161 ppm) are apparent in the ^{13}C NMR spectrum. As time progresses, the ^{13}C static CSA powder pattern typical for an axially symmetric carbonate species begins to appear.[36,99,101] At 516 hours (dark blue spectrum), the powder pattern is typical of the lineshape seen for magnesite, which has been previously characterized.[99,112] The CSA pattern seen earlier, as at 131 hours (red spectrum), is representative of a mixture of one or more magnesium carbonate polymorphs,[36,99] confirmed by *ex situ* ^{13}C MAS NMR experiments. Over the duration of the reaction, it is evident that the metastable magnesium carbonates are present at early times, and as time progresses, the amount of magnesite that is precipitated increases.[111]

After the reaction is stopped, *ex situ* ^{13}C MAS NMR was measured to characterize the spatial dependence of the magnesium carbonate precipitation. The sample was removed from the *in situ* reaction vessel, dried, and cut into slices. The ^{13}C MAS NMR spectrum from each slice was

then analyzed to measure the amount of ^{13}C that has precipitated as a mineral product in each layer. As seen in Figure 4.6, the total amount of ^{13}C is higher at the top of the reaction tube[111] and only precipitates in the magnesite polymorph at these depths. This result is similar to a prior study[36,111] and is due to the diffusion of CO_2 into the sample.[111]

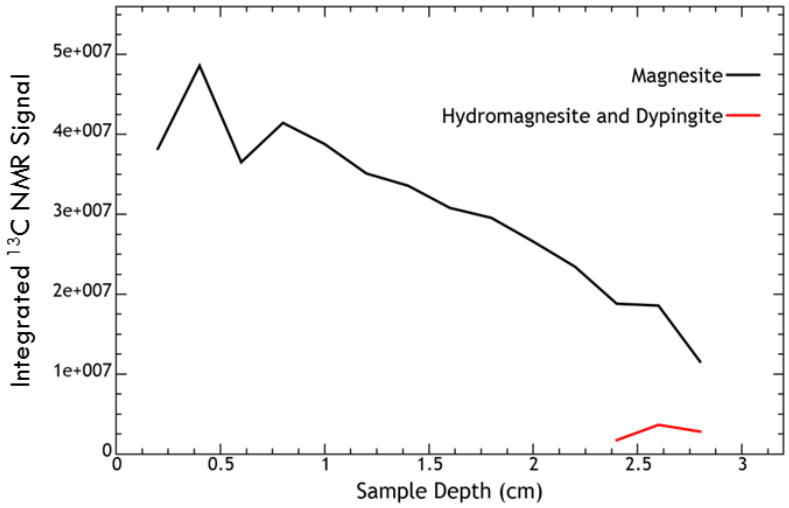

Figure 4.6 ***Ex situ*** **^{13}C MAS NMR of slices from the collected, dried forsterite and CO_2 reaction. The top of the reaction vessel is labelled as 0 cm and the depth goes "down into" the vessel.**

At the bottom of the reaction vessel, it is evident that both magnesite and a combination of hydromagnesite and dypingite are precipitated. Since these metastable minerals are precipitated, the reaction at the bottom of the vessel clearly did not have the requisite conditions to progress to only precipitating magnesite.[111] The progress of reaction depends on many factors including: the time to allow CO_2 to diffuse down the reaction vessel; the pH, that is determined by the $CO_2/HCO_3^-/CO_3^{2-}$ equilibrium, affects the dissolution rate and the minerals that are able to precipitate; and the temperature that changes the kinetics of the reaction.[36,98,111] These factors are difficult to study independently since each feedback into the others. From the *in situ* ^{13}C

NMR data, it is evident that at early times, metastable minerals are precipitated and as the reaction progresses more magnesite is precipitated. This is indicated by the presence of metastable carbonates at the bottom of the reaction vessel which had the least amount of time to react due to CO_2 diffusion that began at the top of the vessel. Therefore, the bottom of the vessel should only need more time for the reaction to progress to observe the precipitation of increasing amounts of magnesite.

4.2 The Effect of Salt on Carbon Mineralization

A key difference between the laboratory study described above (the forsterite, water, and CO_2 reaction system) and carbon sequestration sites is that typically the underground water source is a brine solution. Brine is a solution that contains salt (typically NaCl) in water. It is possible for the ions from the brine solution to affect the chemistry occurring at carbon sequestration sites, and these effects have been studied previously.[113–115] A natural step was to study the reaction of forsterite and CO_2 in the presence of a brine solution; therefore, a 1 M NaCl solution was used as a model of the brine solution in the reacting system.

In situ ^{13}C NMR was recorded for a reaction of forsterite in a brine solution at 80 ^{o}C and 109 atm of CO_2 pressure, seen in Figure 4.7 compared to the forsterite in water reaction from Figure 4.5. By monitoring the formation of magnesium carbonate minerals with time, it is possible to gain information about the effect of NaCl on the reaction progression when compared to the water-only reaction.

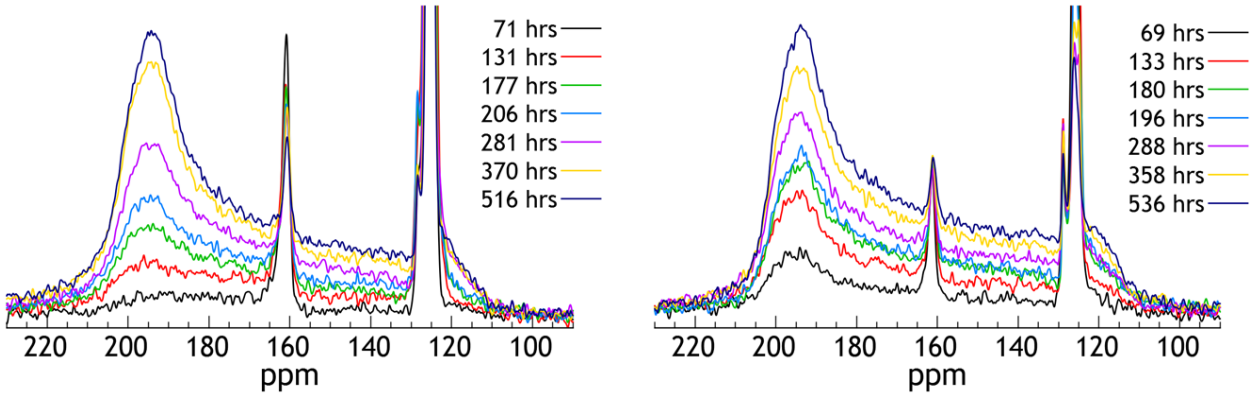

Figure 4.7 ***In situ*** **static ^{13}C NMR spectra at 8.2 T of carbon mineralization reactions. On the left, a forsterite in water reaction with CO_2. On the right, a forsterite in brine solution reaction with CO_2. Each spectrum is at the time point listed in the key.**

As seen in Figure 4.7, the axially-symmetric features of a CSA powder pattern are apparent as early as 69 hours (black spectrum) into the reaction and continue to grow with time. The formation of the magnesite product mineral clearly appears at early times in the brine solution (Figure 4.7 B) as compared to the water-only reaction (Figure 4.7 A). The extent of precipitation of all minerals is also greater at early time points in the reaction with the brine solution. From these results, it is apparent that the NaCl in solution is able to increase the extent of magnesium carbonate precipitation at early times, which will be discussed in the next section. Specifically, the precipitation of the thermodynamic minimum product, magnesite, is enhanced when the reaction occurs in brine.

The *ex situ* MAS NMR was also recorded to see the effect of brine on the spatial distribution of carbonate mineral, shown in Figure 4.8 It is of note that the lower portion of the water-only reaction had evidence of metastable magnesium carbonate minerals while the brine reaction formed solely magnesite throughout the reaction tube. There are some differences in the carbonate distribution, though no large deviation from the water only experiment to draw

conclusions from. This finding again confirms that the presence of NaCl affects the extent of reaction, favoring magnesite over the metastable intermediates with these reaction conditions and lengths. Despite the same amount of time to allow CO_2 to diffuse to the bottom of the reaction vessel, magnesite is able to precipitate in the presence of NaCl.

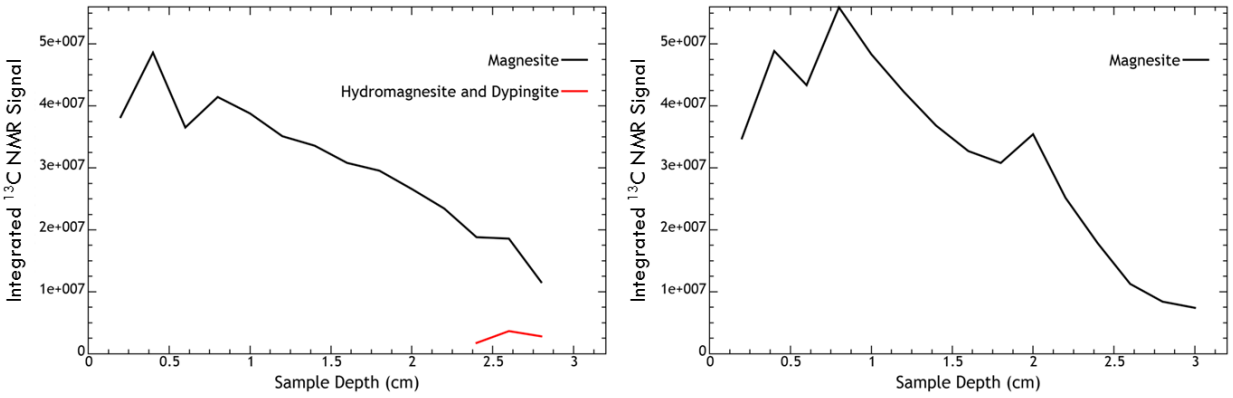

Figure 4.8 ***Ex situ*** **^{13}C MAS NMR of slices from the collected, dried carbon mineralization reactions. On the left, a forsterite in water and CO_2 reaction. On the right, a forsterite in brine solution and CO_2 reaction. The top of the reaction vessel is labelled as 0 cm and the depth goes "down into" the vessel.**

4.3 The Silica-Rich Passivating Layer

The finding that brine solutions increase the kinetics of carbon mineralization reactions as compared to water only solutions has been previously reported.[114] It has been previously reported that a silica-rich passivating layer forms on the outside of particles that react with acidic brine solutions.[113,114,116] There is clear evidence that this layer forms as amorphous silica on the surface of forsterite particles which slows the kinetics of the reaction over time.[113,114,117] When the brine solution is introduced, it is reportedly able to disrupt the formation of this amorphous silica layer which allows the reaction to progress near the initial rate of reaction throughout the reaction time.[114] The ^{13}C NMR results discussed above fit this description of the system in which the reaction with brine solution allows a faster reaction path. This silica layer can be

studied with ^{29}Si NMR to understand its formation as a function of the depth in the reaction vessel.

Amorphous silica is categorized by the bonding environment of the silica sites which differ by the amount of Si-O-Si bonds termed groups "Q1" through "Q4".[118] The other bonds in amorphous silica will be Si-O-H bonds and we can describe the sites by the amount of each site, Si-O-Si:Si-O-H. A Q4 site has 4 Si-O-Si bonds which gives 4:0. A Q3 site has bonds in a 3:1 ratio, a Q2 site in a 2:2, and a Q1 site has a 1:3 ratio. A depiction of these sites can be seen in Figure 4.9. Due to the bonding, the Q4 species are generally located in the middle of an amorphous silica layer and Q1 species will be located on the surface of the amorphous silica layer. The Q2 and Q3 species are often found in between or in the near-surface regions.

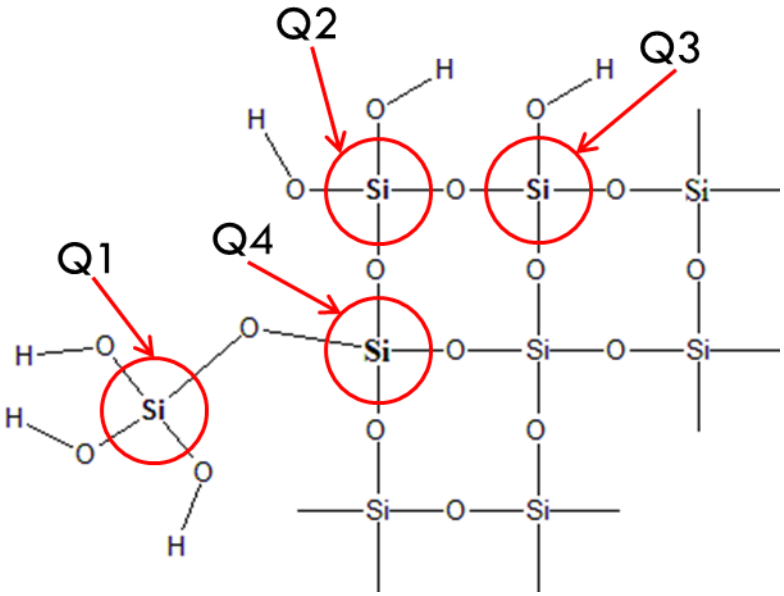

Figure 4.9 Representation of amorphous silica with Q1 through Q4 sites.

After the CO_2-reacted solids in water and brine were cut into slices for *ex situ* NMR, the ^{29}Si MAS NMR and $^{29}Si\{^1H\}$ CPMAS NMR were recorded to examine the silicon coordination environment. Forsterite was the only source of silicon in the system and has a single ^{29}Si site at -62 ppm which gives a narrow resonance (FWHM = 0.44 ppm) due to the crystallinity of the mineral. The ^{29}Si MAS NMR spectrum of forsterite is seen in Figure 4.10.

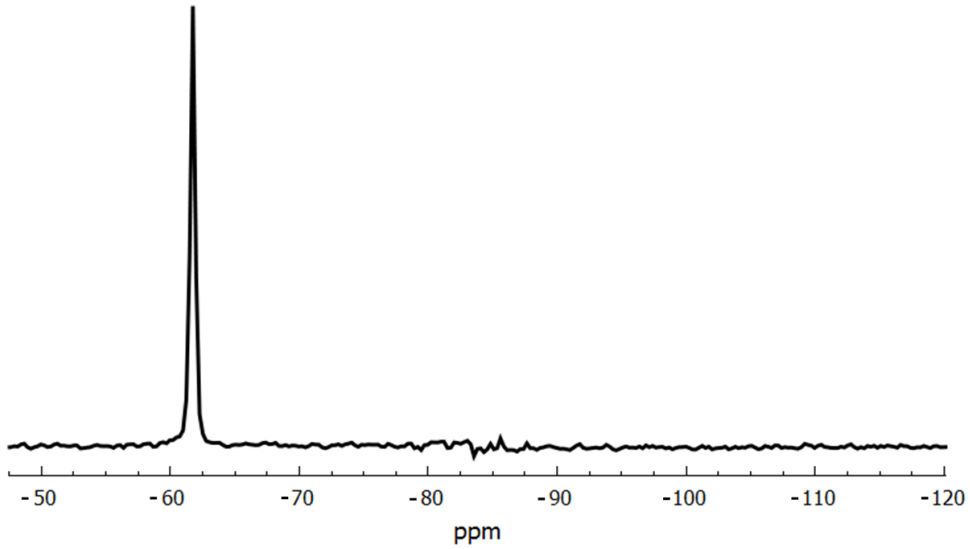

Figure 4.10 ^{29}Si MAS NMR of a forsterite prior to reaction with CO_2.

After reaction, the ^{29}Si MAS NMR was recorded and Figure 4.11 shows a representative slice from both the water and brine reactions. The unreacted forsterite can be seen as the narrow peak at -60 ppm. The broad resonance that appears at -111 ppm is consistent with a Q4 amorphous silica species.[118] Each slice shows only a Q4 species in the direct detect ^{29}Si MAS NMR for both reactions. The Q1, Q2, and Q3 sites are not seen in this directly detected ^{29}Si MAS NMR spectrum. Since each of these sites has at least one Si-O-H bond, they must exist near the surface of the amorphous silica layer. This dictates that the bulk of the volume of the amorphous

silica layer will likely exist as a Q4 site, which would lead to the Q4 being the main site detected in this spectrum. There could also be relaxation effects complicating the detected of the non-observed sites.

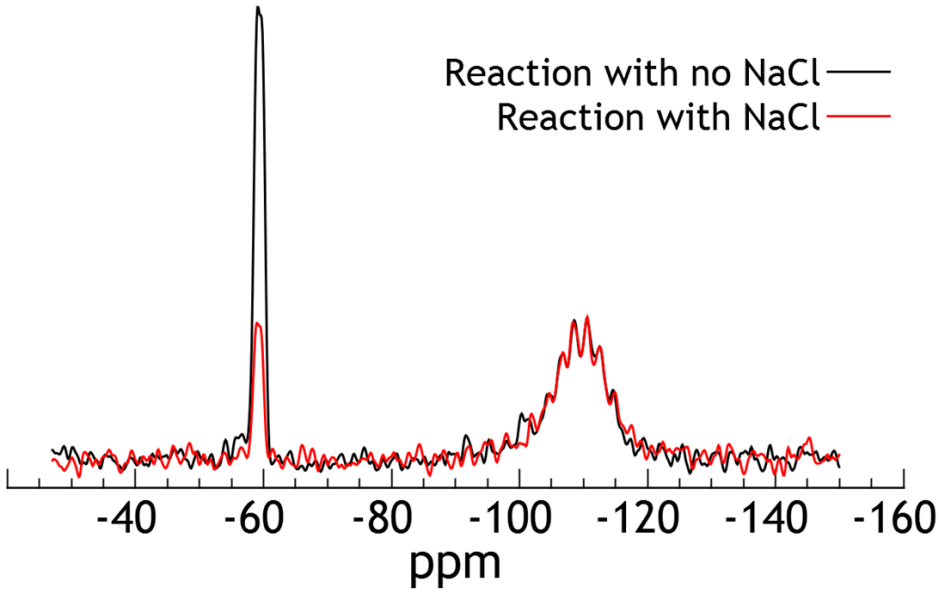

Figure 4.11 ^{29}Si MAS NMR of a representative slice of the carbon mineralization reactions. The black spectrum is the reaction in water. The red spectrum is the reaction in brine.

This result does show that the reaction between CO_2 and forsterite, regardless of the presence of NaCl, forms magnesium carbonate and amorphous silica. No new minerals containing silicon, besides unreacted forsterite, were identified in the reaction vessel.

In order to preferentially observe the surface layers of the amorphous silica layer, ^{29}Si{^{1}H} CPMAS NMR was recorded and shown in Figure 4.12.

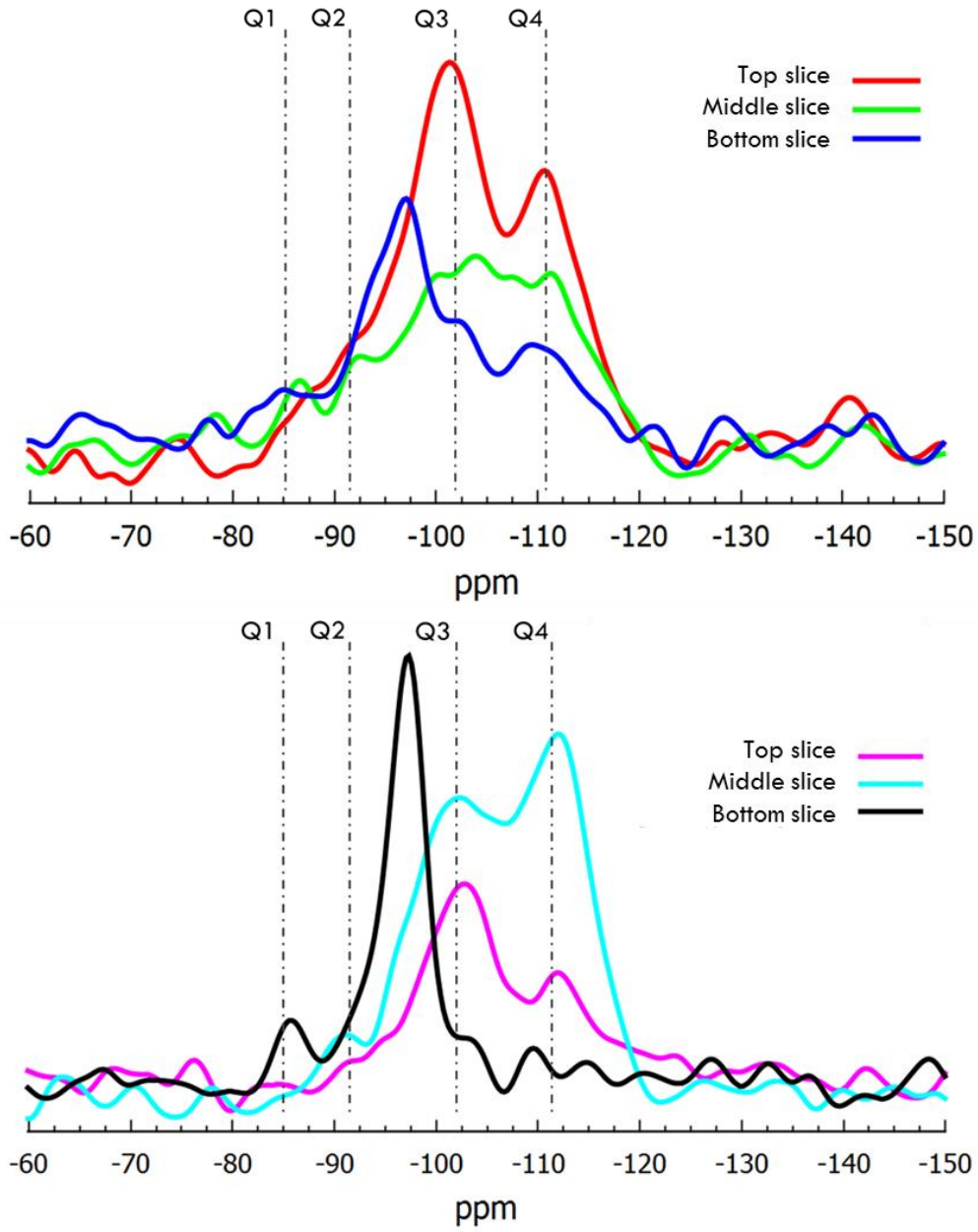

Figure 4.12 $^{29}Si\{^{1}H\}$ CPMAS NMR of a representative slices of the carbon mineralization reactions. The top spectra are from the reaction in water. The bottom spectra are from the reaction in brine. Spinning speed 5 kHz.

In both reactions, the top slices of the reaction vessel have more Q4/Q3 type amorphous silica while the bottom slices of the reaction tend to have more Q2-like sites.[118] As concluded from the

^{13}C NMR discussed in previous sections, the extent of reaction is different in the slices in the reaction vessel. Therefore, the changes in the amorphous silica layer can be correlated with the reaction extent determined from the carbonate precipitation. The top of the reaction vessel had the longest amount of reaction time due to CO_2 diffusion starting at the top of the vessel. The silica layer starts precipitating with mostly OH-bearing silica groups forming increasing amounts of Q4 silica species as the silica layer develops. It is difficult to quantify the amounts of each silica structure because the cross polarization dynamics of each species is different, such that the peak for Q4 is suppressed and the peaks with more closely bound protons are enhanced relative to Q4. This effect is because a short contact time between the carbon and proton spins was chosen so that the most efficient polarization transfer occurred for nearby protons, such as in Q1 through Q3 species. Despite the inability to quantify the amorphous silica layer, the data suggests that the amorphous layer has precipitated over time indicated by the lack of Q4 species at the bottom of the reaction vessel. The CO_2 diffusion from the top of the vessel allows the top slice to react for the entire reaction time (536 hrs). The CO_2 does not reach the bottom slices until further into the reaction time only allowing the amorphous silica layer to form in Q2/Q3 sites.

The peak near -97 ppm does not line up exactly with either a Q2 or Q3 species.[118] The chemical shift of these amorphous silica species are dependent on the Si-O-Si bond angle[119] which could explain the shift. Thus, the silica sites at this isotropic shift have at least one Si-O-H bond which puts these sites near the surface of the silica layer.

The addition of the brine solution to the reaction gives the opportunity to monitor the Na^+ with ^{23}Na NMR. *Ex situ* solid-state ^{23}Na MAS NMR on the collected solids, in Figure 4.13, shows a single resonance that is consistent with solid NaCl at 0 ppm. This indicates that the NaCl does

not form a sodium-bearing carbonate species (between -5 ppm and -40 ppm) during the carbon mineralization reactions. Even though the addition of NaCl does not impact the reaction schemes in terms of stoichiometry, it is evident through NMR studies that the extent of reaction did change due to the use of a brine solution during the carbon mineralization reactions.

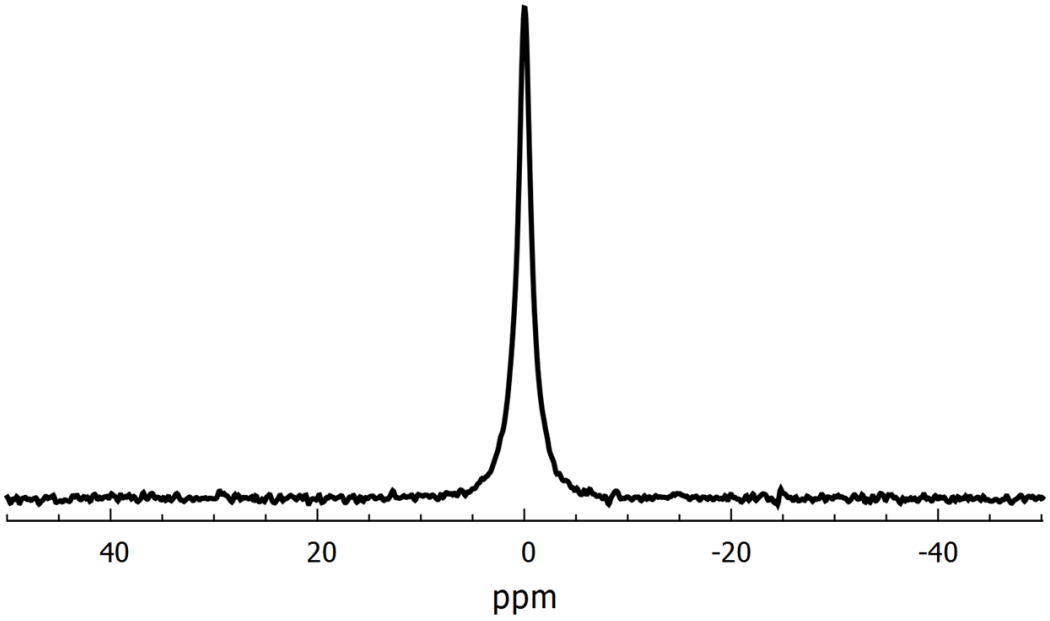

Figure 4.13 ^{23}Na MAS NMR of the forsterite in brine solution reaction with CO_2. FWHM = 1.5 ppm

Carbon mineralization is a method for sequestering CO_2 after capture and is able to be effectively studied with NMR through multiple nuclei. These studies have shown that reactions of CO_2 and forsterite form products such as magnesium carbonate and amorphous silica. It was shown that the CO_2 forsterite reaction progresses faster in the presence of a brine solution, but the product composition is unaffected by this change. ^{13}C MAS NMR was able to show that magnesite is the dominant product of the reaction with the metastable minerals, hydromagnesite and dypingite, forming when the reaction has not had enough time to progress. ^{29}Si MAS and

CPMAS NMR have shown the potential ability to determine the structure of the amorphous silica layer.

4.4 Real Rock Systems: Choosing Systems Wisely

The studies presented above have been conducted on forsterite (Mg_2SiO_4) powder samples, which is the Mg-endmember of olivine [$(Mg,Fe)_2SiO_4$)]. Carbon sequestration sites contain many minerals, in addition to olivine, that have many other structures and constituent elements. Sites for carbon sequestration are envisioned with a layer of caprock, which is a dense rock layer that has little to no permeability. This layer will hold the CO_2-rich brine solution underground to allow time for reaction to occur. The rocks within the reactive formations contain more than just olivine; actually olivine is typically, at most around 10% of basalt's rock composition and there is no olivine in sandstones. The other reactive minerals, such as feldspars (for example $CaAl_2Si_2O_8$), tend to show either less reactivity or slower kinetics than olivine but can be used to react with CO_2 in underground rock formations. There are also porous rocks, like sandstones that are composed of mostly quartz (SiO_2), which the CO_2 rich brine can percolate into the pore space for storage and reaction, if other minerals (like feldspars) are present.

A key difference in the reactive minerals of natural systems is the diversity of divalent cations available to CO_2 for reaction, for example, Mg^{2+}, Ca^{2+}, and Fe^{2+}. An easy example of this is olivine, where forsterite has been a good selection as a representative mineral for NMR studies while the olivine Fe-endmember, fayalite, is not a good candidate since Fe is paramagnetic. Ideally, studies of carbon mineralization would use rock samples from carbon sequestration pilot sites[27–29] to understand the chemistry that occurs in these heterogeneous systems. Therefore,

preliminary studies were done on ideal mineral samples to test the ability of the *in situ* high pressure, high temperature NMR probe to study natural rock systems.

4.4.1 Anorthite ($CaAl_2Si_2O_8$)

Anorthite, $CaAl_2Si_2O_8$, is a feldspar mineral with a reactive Ca^{2+} cation. The reaction of CO_2 and anorthite is chemically quite similar to the reaction with forsterite but is known to have slow rates of reaction, as compared to the forsterite reaction where significant carbonate mineral precipitation occurs within the first 60 hrs. In the forsterite reaction, bicarbonate, from the CO_2 equilibrium, is detectable after a week of reaction, and detectable amounts of carbonate mineral precipitation are seen after 2 weeks of reaction. Based on these reaction durations, the slower reaction of anorthite should still be possible to record with NMR. If *in situ* NMR is capable of studying a pure feldspar mineral, mixtures of feldspar and olivine minerals that mimic sedimentary rocks can be studied; therefore, a reaction was run at 90 ^oC and 85 atm of CO_2 with anorthite and water, and is shown in Figure 4.14.

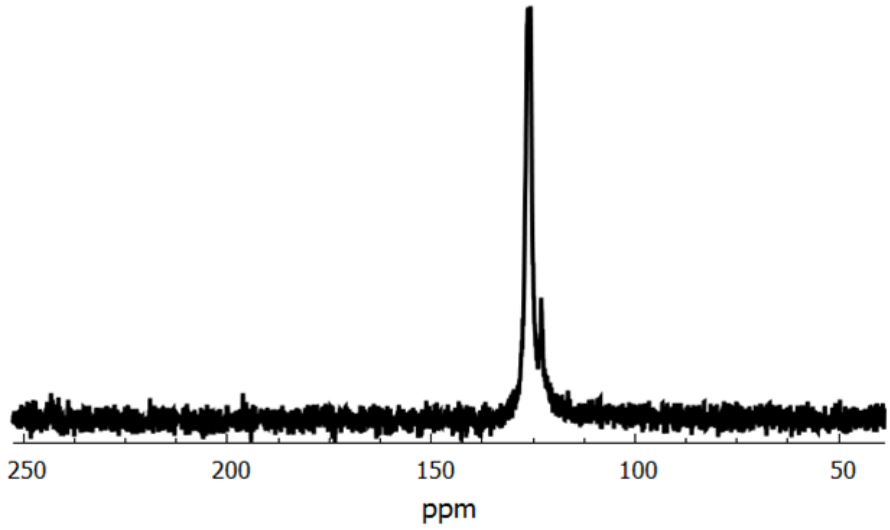

Figure 4.14 ***In situ*** **^{13}C NMR of CO_2 reacting with anorthite in water at 90 ^{o}C and 85 atm of CO_2. Spectrum is after 42 days of reaction.**

After 42 days of reaction, no evidence of bicarbonate or carbonate is detectable in the *in situ* ^{13}C NMR (seen between 160 ppm to 175 ppm). The only resonance present in the ^{13}C NMR for the reaction with anorthite is CO_2 in solution at 125 ppm. Therefore, feldspar minerals are not feasible reactions at these temperatures and pressures on the typical timeline of a 2 to 3 year research project. While anorthite is a good mineral candidate to make the reaction more closely mimic a true sequestration site, it is not easy to study in the laboratory with *in situ* NMR. This result does indicate that while the pH of the solution in this reaction is quite low, leading to dissolution of Ca^{2+} ions, no carbonate ions were present at these pH levels to allow for the formation of calcium carbonate minerals. Furthermore, it is unlikely that any carbonate mineral would precipitate at the (assumed) pH level because the pH needs to be greater than 6 to promote carbonate precipitation.

4.4.2 Peridotite

Iron (Fe^{2+}) is a common cation in sedimentary rocks which causes problems for studies with NMR because it is paramagnetic and therefore causes, among other effects, broadening of the NMR resonances. It is possible to study materials with small concentrations of paramagnetic species, and in some cases this is even a benefit to the NMR measurements due to a decrease in T_1 relaxation times. An example of a rock system that contains Fe^{2+} is peridotite, which contains the mineral olivine [$(Mg,Fe)_2SiO_4$] and pyroxene minerals [$XY(Si,Al)_2O_6$]. In pyroxene, the mineral is characterized by the X and Y cations, where X is typically Ca^{2+}, Na^{+}, Fe^{2+}, or Mg^{2+} and Y is smaller ions such as Al^{3+}, Cr^{3+}, Ti^{4+}, and Fe^{3+}. Peridotite makes up the majority of the Earth's upper mantle, which makes it a common target for sequestration sites. The Fe^{2+} concentration can vary for different peridotite samples, and the sample studied here contained approximately 10% Fe. Preliminary studies were conducted to test the ability of the *in situ* NMR system to observe signal. As seen in Figure 4.15, 1 atm of CO_2 gas has a linewidth of 42.4 Hz. When 50 atm of CO_2 gas is detected in the presence of Fe-containing peridotite, the linewidth changes to 15000 Hz (a 350x larger linewidth). The spectra presented here are plotted on a frequency axis in Hz. The effects on the spectra from the paramagnetic species make referencing the Fe-containing spectra to ppm difficult. The relevant information in these preliminary studies, linewidth, can be ascertained from the spectra in Hz, but it should be noted that the exact Hz values are only able to be referenced to data acquired on an 8.2 T magnet.

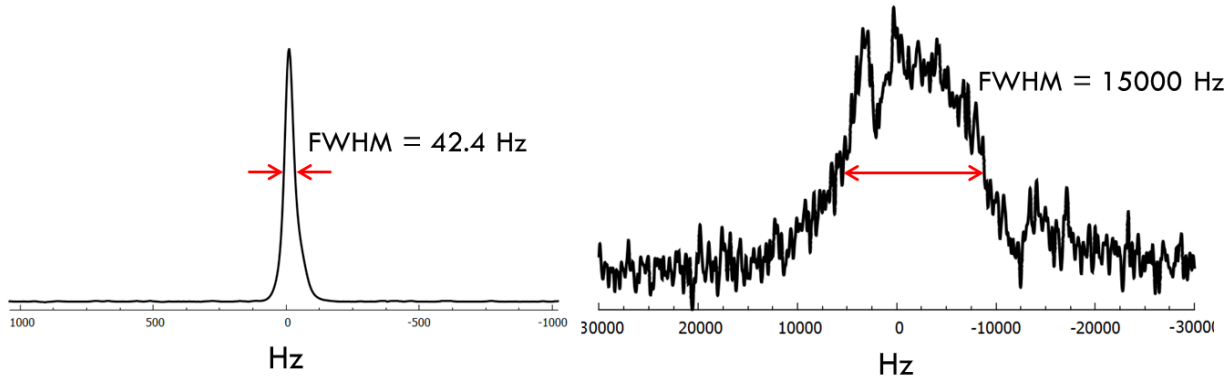

Figure 4.15 ***In situ*** **^{13}C NMR at 8.2 T of CO_2 gas (left) at 1 atm and CO_2 with peridotite (right) at 50 atm.**

This linewidth is only the example of the motionally narrowed CO_2 gas peak in the reaction system; the Fe in the sample will also broaden the solid mineralization product signals that have linewidths around 8000 Hz (in non-Fe-containing samples). These resonances will be broadened as well, likely becoming undetectable. The use of *in situ* NMR prior to carbonate precipitation would be complicated because the resonances for CO_2 and bicarbonate are only separated by 3200 Hz, which would therefore be obscured by a 15,000 Hz wide signal. Therefore, any mineral with a Fe content of 10% is not possible to study with NMR.

4.4.3 Cement Powder

Cement is of interest to carbon sequestration studies because the CO_2 injection sites are typically sealed with cement,[85,116,120,121] and it is another example of an iron-containing substance. The cement along with the caprock is needed to keep the CO_2 at the sequestration site once it is injected. Cement is composed of a mixture of minerals, primarily calcium carbonates, which can dissolve in acidic conditions, much like CO_2 sequestration conditions. The CO_2-rich brine

solution will come into contact with the cement seal at the injection sites and possibly begin to dissolve the cement, leaving it weakened and possibly able to fracture and release the CO_2 back into the atmosphere. A typical Portland cement that could be used to seal carbon sequestration wells was used in this study and was calculated to have a Fe^{2+} content of 2%. A ^{13}C NMR spectrum was recorded with 50 atm of CO_2 pressure over the cement powder, and is shown in Figure 4.16 (as in section 4.4.2, this is plotted in Hz). In this case the CO_2 gas peak was broadened to 1600 Hz. These linewidths would still overlap the resonances for CO_2 and HCO_3^-, which make the *in situ* NMR measurements difficult.

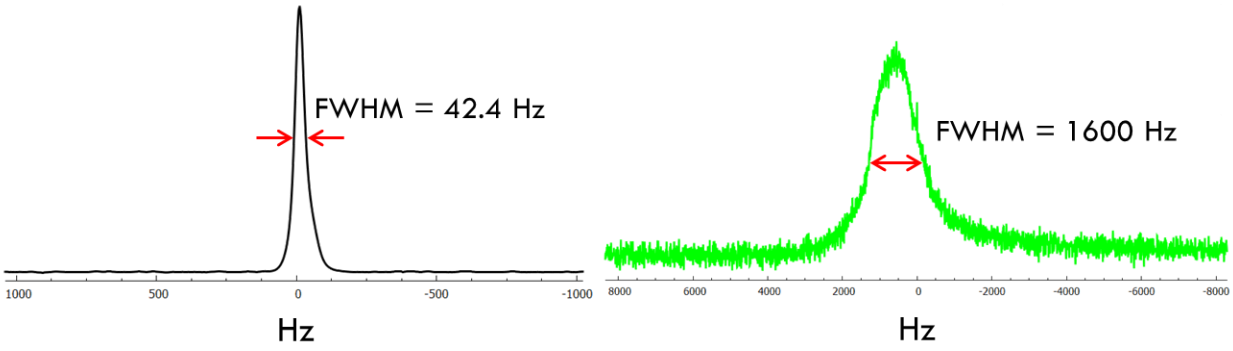

Figure 4.16 ***In situ*** **^{13}C NMR at 8.2 T of CO_2 gas (left) at 1 atm and CO_2 with cement powder (right) at 50 atm.**

These examples are worthwhile to keep in mind, because while it is difficult to use *in situ* ^{13}C NMR in these cases, it is important to know the bounds of the analytical technique.

4.5 Cement Precursors

Cement has typically been used to seal injection wells at sites for carbon sequestration which means that the degradation of cement under acidic conditions needs to be understood.[85,116,120,122,123] Cement from Calera Corporation was observed as a mixture of species, of which calcium carbonate ($CaCO_3$) is the dominant mineral species. Calcium carbonate exists in three polymorphs which can be distinguished by ^{13}C NMR because the chemical shift is extraordinarily sensitive to the local chemical environment. The polymorphs are calcite (168.2 ppm), aragonite (170.5 ppm), and vaterite (170.1 ppm and 169.1 ppm) with their ^{13}C NMR chemical shifts listed in parentheses.[100,124] The process of making cement powder forms a mixture of calcium carbonates with other species. Understanding the composition of the cement mixture, the ratio calcium carbonate polymorphs and the other species present, will give insight to the quality of the cement material.

With this NMR characterization, chemical bonding environments evident in cement materials can be determined by ^{13}C MAS NMR.[100] To understand the ^{13}C spectra, the spectra are discussed in two regions; the "carbonate (CO_3^{2-}) region" (from 168 ppm to 173 ppm) and the "bicarbonate (HCO_3^-) region" (from 161 ppm to 168 ppm). Three different cement samples obtained from Calera Corporation were observed with ^{13}C MAS NMR, be seen in Figure 4.17.

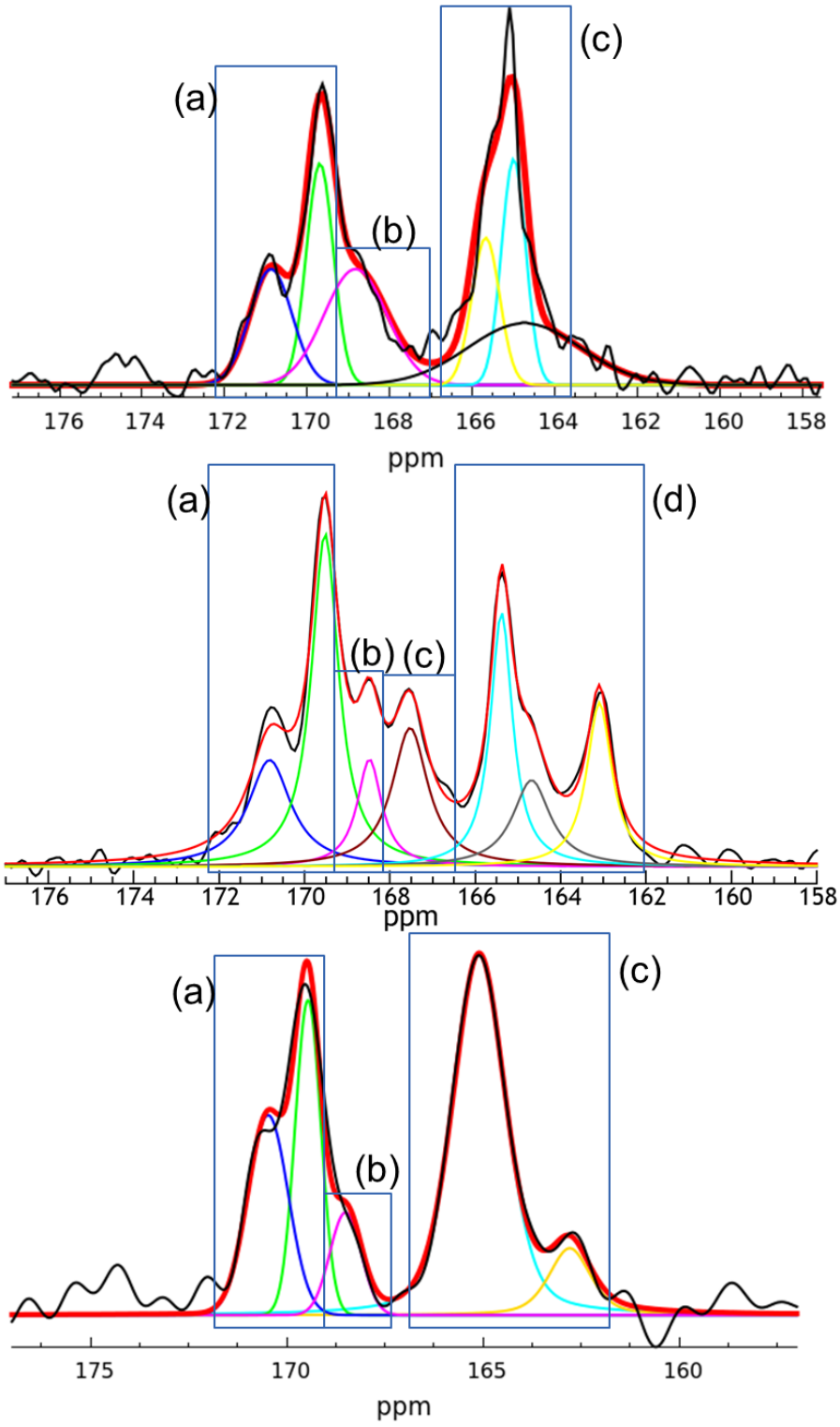

Figure 4.17 $^{13}C\{^{1}H\}$ CPMAS NMR of the cement precursors with a spinning rate of 5 kHz. Sample 1 on top. Sample 2 in the middle. Sample 3 on the bottom. The experimental data is in black and the overall fit is in red. Fits of vaterite are in green and royal blue. Fit of calcite is in purple. Fits of bicarbonate resonances are in light blue, yellow, and black. Na-containing peak is in red.

Figure 4.17 shows vaterite in the box labeled (a) and calcite in the box labeled (b). Box (c) contains the peaks in the bicarbonate region. In sample 2, a new peak appears and has been labeled in box (d), which will be discussed separately. In the carbonate region, every sample shows a mixture of calcite and vaterite, and were therefore compared by a ratio of vaterite:calcite (V:C in the table). Sample 1 has a ratio of 1.5:1, which is a relatively large amount of calcite. Sample 2 has a ratio of 5.1:1, and sample 3 has a ratio of 5.0:1; thus these latter two samples are dominantly composed of the vaterite polymorph. The ^{13}C MAS NMR parameters of the three cement samples are summarized in Table 4.1.

Table 4.1 The 13C NMR chemical shift and linewidth of the cement precursor samples

Species	Sample 1		Sample 2		Sample 3	
	Chemical Shift (ppm)	Width (ppm)	Chemical Shift (ppm)	Width (ppm)	Chemical Shift (ppm)	Width (ppm)
Vaterite	169.7	0.77	169.5	0.77	169.5	0.77
	170.9	1.21	170.8	1.21	170.5	1.21
Calcite	168.8	1.80	168.5	0.70	168.9	0.94
Other			167.5	1.02		
HCO_3^-	165.0	0.69	165.4	0.62	165.1	1.57
	165.7	0.79	164.7	1.06	162.8	1.42
	164.6	3.22*	163.1	0.71		
V:C	1.5:1		5.1:1		5.0:1	

* Denotes peaks that are used for fitting but less certain of their overall spectral quality

There are also intense resonances in the bicarbonate region of the ^{13}C NMR each sample. The qualitative observation of this region is that each sample has differences in these peaks which will need to be characterized more fully to understand the structural differences. Sample 3 has

the broadest bicarbonate species, which indicates disorder in the bicarbonate species or a wider variety of environments, while bicarbonate is narrower in samples 1 and 2.

The ^{23}Na NMR was also recorded because sodium is part of the reactant mixture of the cement powder formation, seen in Figure 4.18. Samples 1 and 3 have sodium in NaCl form, with sample 3 only having trace amounts. Sample 2 has a secondary sodium-containing species that is in the region of the Na chemical shift that is assigned to Na-containing bicarbonate or carbonate species (which overlap in ^{23}Na spectra). This peak has been tentatively assigned to a sodium containing carbonate mineral.

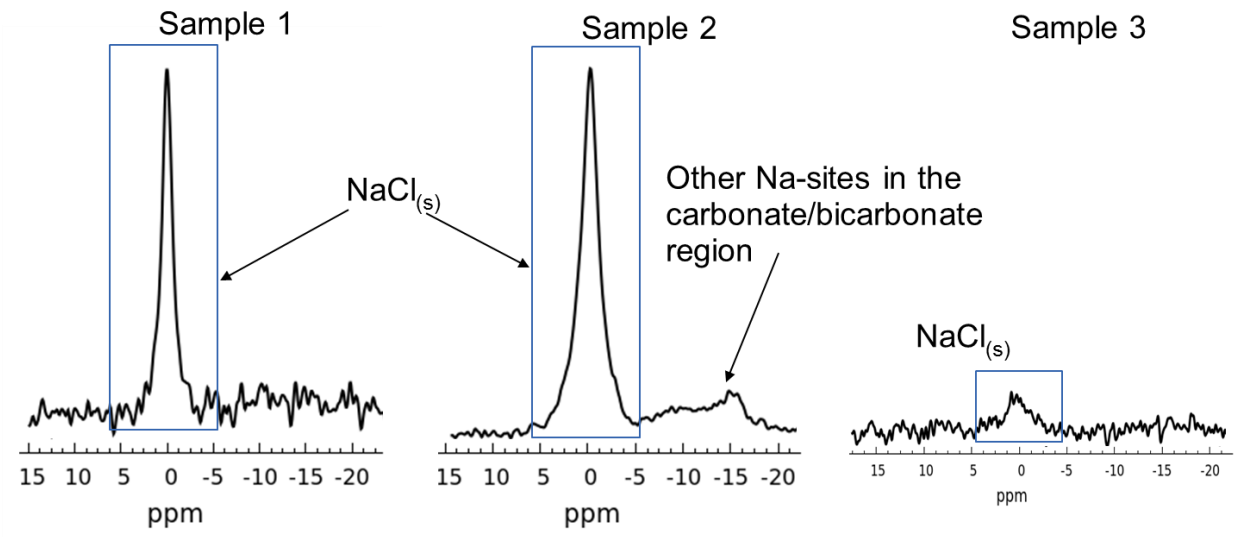

Figure 4.18 ^{23}Na MAS NMR at 7 T spinning at 5 kHz. Sample 1 on the left, sample 2 in the middle, sample 3 on the right.

These data show that the final cement powder product is very dependent on the process and reactants used to make the powder. The polymorph of calcium carbonate, bicarbonate species, and sodium content are all affected by the process. Sodium may be monitored as a possible "reporter" of structure, as either NaCl or as a Na-containing carbon species.

References

(1) Bazzaz, F. *Annu. Rev. Ecol. Syst.* **1990**, *21*, 167.

(2) Bhown, A. S.; Freeman, B. C. *Environ. Sci. Technol.* **2011**, *45*, 8624.

(3) Samanta, A.; Zhao, A.; Shimizu, G. K. H.; Sarkar, P.; Gupta, R. *Ind. Eng. Chem. Res.* **2012**, *51*, 1438.

(4) Choi, S.; Drese, J. H.; Jones, C. W. *ChemSusChem* **2009**, *2*, 796.

(5) Schuiling, R. D.; de Boer, P. L. *Environ. Sci. Eur.* **2013**, *25*.

(6) Jones, C. W. *Annu. Rev. Chem. Biomol. Eng.* **2011**, *2*, 31.

(7) Jun, Y.; Giammar, D. E.; Werth, C. J. *Environ. Sci. Technol.* **2013**, *47*, 3.

(8) Didas, S. A.; Kulkarni, A. R.; Sholl, D. S.; Jones, C. W. *ChemSusChem* **2012**, *5*, 2058.

(9) Hicks, J. C.; Drese, J. H.; Fauth, D. J.; Gray, M. L.; Qi, G.; Jones, C. W. *J. Am. Chem. Soc.* **2008**, *130*, 2902.

(10) Sharma, S.; Azzi, M. *Fuel* **2014**, *121*, 178.

(11) Queen, W. L.; Brown, C. M.; Britt, D. K.; Zajdel, P.; Hudson, M. R.; Yaghi, O. M. *J. Phys. Chem. C* **2011**, *115*, 24915.

(12) Kong, X.; Scott, E.; Ding, W.; Mason, J. A.; Long, J. R.; Reimer, J. A. *J. Am. Chem. Soc.* **2012**, *134*, 14341.

(13) Lin, L.-C.; Kim, J.; Kong, X.; Scott, E.; McDonald, T. M.; Long, J. R.; Reimer, J. A.; Smit, B. *Angew. Commun.* **2013**, *52*, 4410.

(14) Du, N.; Park, H. B.; Robertson, G. P.; Dal-Cin, M. M.; Visser, T.; Scoles, L.; Guiver, M. D. *Nat. Mater.* **2011**, *10*, 372.

(15) Budd, P. M.; Elabas, E. S.; Ghanem, B. S.; Makhseed, S.; McKeown, N. B.; Msayib, K. J.; Tattershall, C. E.; Wang, D. *Adv. Mater.* **2004**, *16*, 456.

(16) Budd, P. M.; Ghanem, B. S.; Makhseed, S.; McKeown, N. B.; Msayib, K. J.; Tattershall, C. E. *Chem. Commun.* **2004**, 230.

(17) Du, N.; Robertson, G. P.; Dal-Cin, M. M.; Scoles, L.; Guiver, M. D. *Polymer* **2012**, *53*, 4367.

(18) Guiver, M. D.; Lee, Y. M. *Science* **2013**, *339*, 284.

(19) Du, N.; Park, B.; Dal-Cin, M. M.; Guiver, M. D. *Energy Environ. Sci.* **2012**, *5*, 7306.

(20) Lin, H.; Freeman, B. D. *J. Mol. Struct.* **2005**, *739*, 57.

(21) Merkel, T. C.; Lin, H.; Wei, X.; Baker, R. *J. Memb. Sci.* **2010**, *359*, 126.

(22) Shao, P.; Dal-Cin, M. M.; Guiver, M. D.; Kumar, A. *J. Memb. Sci.* **2013**, *427*, 451.

(23) Zhang, J.; Webley, P. A.; Xiao, P. *Energy Convers. Manag.* **2008**, *49*, 346.

(24) Bollini, P.; Didas, S. A.; Jones, C. W. *J. Mater. Chem.* **2011**, *21*, 15100.

(25) Li, W.; Choi, S.; Drese, J. H.; Hornbostel, M.; Krishnan, G.; Eisenberger, P. M.; Jones, C. W. *ChemSusChem* **2010**, *3*, 899.

(26) Song, J.; Zhang, D. *Environ. Sci. Technol.* **2013**, *47*, 9.

(27) Fischer, S.; Liebscher, A.; De Lucia, M.; Hecht, L. *Environ. Earth Sci.* **2013**.

(28) Carroll, S. A.; Mcnab, W. W.; Dai, Z.; Torres, S. C. *Environ. Sci. Technol.* **2013**, *47*, 252.

(29) Martens, S.; Kempka, T.; Liebscher, A.; Lu, S.; Myrttinen, A.; Norden, B.; Mo, F.; Group, T. K.; Zimmer, M.; Ku, M. *Environ. Earth Sci.* **2012**, *67*, 323.

(30) Lu, P.; Fu, Q.; Seyfried, W. E.; Hedges, S. W.; Soong, Y.; Jones, K.; Zhu, C. *Appl. Geochemistry* **2013**, *30*, 75.

(31) Harvey, O. R.; Qafoku, N. P.; Brown, C. F.; Cantrell, K. J.; Lee, G.; Amonette, J. E. *Environ. Eng. Sci.* **2013**, *47*, 23.

(32) Kolodziejski, W.; Klinowski, J. *Chem. Rev.* **2002**, *102*, 613.

(33) Massiot, D.; Fayon, F.; Capron, M.; King, I.; Le Calve, S.; Alonso, B.; Durand, J.-O.; Bujoli, B.; Gan, Z.; Hoatson, G. *Magn. Reson. Chem.* **2002**, *40*, 70.

(34) Drese, J. H.; Choi, S.; Lively, R. P.; Koros, W. J.; Fauth, D. J.; Gray, M. L.; Jones, C. W. *Adv. Funct. Mater.* **2009**, *19*, 3821.

(35) Chaikittisilp, W.; Didas, S. A.; Kim, H.; Jones, C. W. *Chem. Mater.* **2013**, *25*, 613.

(36) Surface, J. A.; Skemer, P.; Hayes, S. E.; Conradi, M. S. *Environ. Sci. Technol.* **2013**, *47*, 119.

(37) Yang, Q.; Bown, M.; Ali, A.; Winkler, D.; Puxty, G.; Attalla, M. *Energy Procedia* **2009**, *1*, 955.

(38) Mani, F.; Peruzzini, M.; Stoppioni, P. *Green Chem.* **2006**, *8*, 995.

(39) Moore, J. K.; Guiver, M. D.; Du, N.; Hayes, S. E.; Conradi, M. S. *J. Phys. Chem. C* **2013**, *117*, 22995.

(40) Fukushima, E.; Roeder, S. B. W. *Experimental Pulse NMR: A Nuts and Bolts Approach*; Addison-Wesley Publishing Company, 1981.

(41) Liu, S. Bin; Doverspike, M. A.; Conradi, M. S. *J. Chem. Phys.* **1984**, *81*, 6064.

(42) Ratcliffe, C. I.; Ripmeester, J. A. *J. Phys. Chem.* **1986**, *90*, 1259.

(43) Bayer, H. *Zeitschrift fur Phys.* **1951**, *130*, 227.

(44) Mehring, M. *Principles of High Resolution NMR in Solids*; 2nd ed.; Springer, 1983.

(45) Liu, S.; Conradi, M. S. *Phys. Rev. B* **1984**, *30*, 24.

(46) Ouyang, B.; Conradi, M. S. *Phys. Rev. B* **1991**, *44*, 9295.

(47) Gullion, T.; Conradi, M. S. *Phys. Rev. B* **1985**, *32*, 7076.

(48) Rothwell, W. P.; Waugh, J. S. *J. Chem. Phys.* **1981**, *74*, 2721.

(49) Slichter, C. P. *Principles of Magnetic Resonance*; 3rd ed.; Springer, 1990.

(50) Etesse, P.; Zega, J. A.; Kobayashi, R. *J. Chem. Phys.* **1992**, *97*, 2022.

(51) Abragam, A. *The Principles of Nuclear Magnetism*; Oxford University Press: London, 1973.

(52) Xu, X.; Song, C.; Andresen, J. M.; Miller, B. G.; Scaroni, A. W. *Energy & Fuels* **2002**, *16*, 1463.

(53) Tsuda, T.; Fujiwara, T. *J. Chem. Soc. Chem. Commun.* **1992**, 1659.

(54) Tsuda, T.; Fujiwara, T.; Taketani, Y.; Saegusa, T. *Chem. Lett.* **1992**, *21*, 2161.

(55) Pinto, M. L.; Mafra, L.; Guil, J. M.; Pires, J.; Rocha, J. *Chem. Mater.* **2011**, *23*, 1387.

(56) Khatri, R. A.; Chuang, S. S. C.; Soong, Y.; Gray, M. *Ind. Eng. Chem. Res.* **2005**, *44*, 3702.

(57) Bacsik, Z.; Ahlsten, N.; Ziadi, A.; Zhao, G.; Garcia-Bennett, A. E.; Martín-Matute, B.; Hedin, N. *Langmuir* **2011**, *27*, 11118.

(58) Robinson, K.; McCluskey, A.; Attalla, M. I. *Chemphyschem* **2011**, *12*, 1088.

(59) Danon, A.; Stair, P. C.; Weitz, E. *J. Phys. Chem. C* **2011**, *115*, 11540.

(60) Knofel, C.; Martin, C.; Hornebecq, V.; Llewellyn, P. L. *J. Phys. Chem. C* **2009**, *113*, 21726.

(61) Vaidya, P. D.; Kenig, E. Y. *Chem. Eng. Technol.* **2007**, *30*, 1467.

(62) Ma, X.; Wang, X.; Song, C. *J. Am. Chem. Soc.* **2009**, *131*, 5777.

(63) Da Silva, Eirik, F.; Svendsen, H. F. *Int. J. Greenh. Gas Control* **2007**, *1*, 151.

(64) Reich, H. J. C-13 Chemical Shifts http://www.chem.wisc.edu/areas/reich/handouts/nmr-c13/cdata.htm.

(65) Drage, T. C.; Arenillas, A.; Smith, K. M.; Snape, C. E. *Microporous Mesoporous Mater.* **2008**, *116*, 504.

(66) Huang, S.-J.; Hung, C.; Zheng, A.; Lin, J.; Yang, C.; Chang, Y.; Deng, F.; Liu, S. *J. Phys. Chem. Lett.* **2014**, *5*, 3183.

(67) Li, D.; Furukawa, H.; Deng, H.; Liu, C.; Yaghi, O. M.; Eisenberg, D. S. *Proc. Natl. Acad. Sci. U. S. A.* **2014**, *111*, 191.

(68) Wang, X.; Schwartz, V.; Clark, J. C.; Ma, X.; Overbury, S. H.; Xu, X.; Song, C. *J. Phys. Chem. C* **2009**, *113*, 7260.

(69) Espinal, L.; Green, M. L.; Fischer, D. A.; Delongchamp, D. M.; Jaye, C.; Horn, J. C.; Sakwa-novak, M. A.; Chaikittisilp, W.; Brunelli, N. A.; Jones, C. W. *J. Phys. Chem. Lett.* **2015**, *6*, 148.

(70) Harris, R. K.; Olivieri, A. C. *Prog. NMR Spectrosc.* **1992**, *24*, 435.

(71) Olivieri, A. C.; Frydman, L.; Diaz, L. E. *J. Magn. Reson.* **1987**, *75*, 50.

(72) Hexem, J. G.; Frey, M. H.; Opella, S. J. *J. Chem. Phys.* **1982**, *77*, 3847.

(73) Hexem, J. G.; Frey, M. H.; Opella, S. J. *J. Am. Chem. Soc.* **1981**, *103*, 224.

(74) Naito, A.; Ganapathy, S.; McDowell, C. A. *J. Chem. Physics1* **1981**, *74*, 5393.

(75) Naito, a; Ganapathy, S.; McDowell, C. . *J. Magn. Reson.* **1982**, *48*, 367.

(76) Chaffee, A. L.; Knowles, G. P.; Liang, Z.; Zhang, J.; Xiao, P.; Webley, P. A. *Int. J. Greenh. Gas Control* **2007**, *1*, 11.

(77) Chou, C.-T.; Chen, C.-Y. *Sep. Purif. Technol.* **2004**, *39*, 51.

(78) Ishibashi, M.; Ota, H.; Akutsu, N.; Umeda, S.; Tajika, M.; Izumi, J.; Yasutake, A.; Kabata, T.; Kegeyama, Y. *Energy Convers. Manag.* **1996**, *37*, 929.

(79) Liu, X.; Zhou, L.; Fu, X.; Sun, Y.; Su, W.; Zhou, Y. *Chem. Eng. Sci.* **2007**, *62*, 1101.

(80) Belmabkhout, Y.; Sayari, A. *Energy & Fuels* **2010**, *24*, 5273.

(81) Donaldson, T. L.; Nguyen, Y. N. *Ind. Eng. Chem. Fundam.* **1980**, *19*, 260.

(82) Didas, S. A.; Sakwa-novak, M. A.; Foo, G. S.; Sievers, C.; Jones, C. W. *J. Phys. Chem. Lett.* **2014**, *5*, 4194.

(83) Hiyoshi, N.; Yogo, K.; Yashima, T. *Microporous Mesoporous Mater.* **2005**, *84*, 357.

(84) Zhang, S.; Depaolo, D. J.; Xu, T.; Zheng, L. *Int. J. Greenh. Gas Control* **2013**, *18*, 315.

(85) Huerta, N. J.; Hesse, M. A.; Bryant, S. L.; Strazisar, B. R.; Lopano, C. L. *Environ. Sci. Technol.* **2013**, *47*, 269.

(86) Bénézeth, P.; Saldi, G. D.; Dandurand, J.-L.; Schott, J. *Chem. Geol.* **2011**, *286*, 21.

(87) Zhao, L.; Sang, L.; Chen, J.; Ji, J.; Teng, H. H. *Environ. Sci. Technol.* **2010**, *44*, 406.

(88) Case, D. H.; Wang, F.; Giammar, D. E. *Environ. Eng. Sci.* **2011**, *28*, 881.

(89) Ballirano, P.; De Vito, C.; Mignardi, S.; Ferrini, V. *Chem. Geol.* **2013**, *340*, 59.

(90) Lackner, K. S. *Annu. Rev. Energy Environ.* **2002**, *27*, 193.

(91) Wilson, S. A.; Barker, S. L. L.; Dipple, G. M.; Atudorei, V. *Environ. Sci. Technol.* **2010**, *44*, 9522.

(92) Hövelmann, J.; Putnis, C. V; Ruiz-Agudo, E.; Austrheim, H. *Environ. Sci. Technol.* **2012**, *46*, 5253.

(93) Peters, C. A. *Chem. Geol.* **2009**, *265*, 198.

(94) Hänchen, M.; Prigiobbe, V.; Baciocchi, R.; Mazzotti, M. *Chem. Eng. Sci.* **2008**, *63*, 1012.

(95) King, H. E.; Plümper, O.; Putnis, A. *Environ. Sci. Technol.* **2010**, *44*, 6503.

(96) Shibuya, T.; Yoshizaki, M.; Masaki, Y.; Suzuki, K.; Takai, K.; Russell, M. J. *Chem. Geol.* **2013**, *359*, 1.

(97) Botha, A.; Strydom, C. A. A. *Hydrometallurgy* **2001**, *62*, 174.

(98) Surface, J. A.; Wang, F.; Zhu, Y.; Hayes, S. E.; Giammar, D. E.; Conradi, M. S. *Environ. Sci. Technol.* **2015**, *49*, 1631.

(99) Moore, J. K.; Surface, J. A.; Brenner, A.; Skemer, P.; Conradi, M. S.; Hayes, S. E. *Environ. Sci. Technol.* **2015**, *49*, 657.

(100) Nebel, H.; Neumann, M.; Mayer, C.; Epple, M. *Inorg. Chem.* **2008**, *47*, 7874.

(101) Papenguth, H. W.; Kirkpatrick, R. J.; Montez, B.; Sandberg, P. A. *Am. Mineral.* **1989**, *74*, 1152.

(102) Mason, H. E.; Kozlowski, A.; Phillips, B. L. *Chem. Mater.* **2008**, *20*, 294.

(103) Sevelsted, T. F.; Herfort, D.; Skibsted, J. *Cem. Concr. Res.* **2013**, *52*, 100.

(104) Hoyt, D. W.; Turcu, R. V. F.; Sears, J. A.; Rosso, K. M.; Burton, D.; Felmy, A. R.; Hu, J. Z.; Burton, S. D. *J. Magn. Reson.* **2011**, *212*, 378.

(105) Kwak, J. H.; Hu, J. Z.; Hoyt, D. W.; Sears, J. A.; Wang, C.; Rosso, K. M.; Felmy, A. R. *J. Phys. Chem.* **2010**, *114*, 4126.

(106) Lackner, K. S.; Wendt, C. H.; Butt, D. P.; Joyce, E. L.; Sharp, D. H. *Energy* **1995**, *20*, 1153.

(107) Schaef, H. T.; Windisch, C. F.; McGrail, B. P.; Martin, P. F.; Rosso, K. M. *Geochim. Cosmochim. Acta* **2011**, *75*, 7458.

(108) Yang, Y.; Min, Y.; Jun, Y. *Environ. Sci. Technol.* **2013**, *47*, 150.

(109) King, H. E.; Putnis, C. V. *Geochim. Cosmochim. Acta* **2013**, *109*, 113.

(110) Oelkers, E. H.; Schott, J.; Devidal, J.-L. *Geochim. Cosmochim. Acta* **1994**, *58*, 2011.

(111) Xiong, W.; Giammar, D. *Environ. Sci. Technol. Lett.* **2014**, *1*, 333.

(112) Giammar, D. E.; Bruant, R. G.; Peters, C. A. *Chem. Geol.* **2005**, *217*, 257.

(113) Bearat, H.; McKelvy, M. J.; Chizmeshya, A. V. G.; Gormley, D.; Nunez, R.; Carpenter, R. W.; Squires, K.; Wolf, G. H. *Environ. Sci. Technol.* **2006**, *40*, 4802.

(114) Wang, F.; Giammar, D. E. *Environ. Sci. Technol.* **2013**, *47*, 168.

(115) Wang, S.; Edwards, I. M.; Clarens, A. F.; Engineering, E.; Road, M.; Hall, T. *Environ. Sci. Technol.* **2013**, *47*, 234.

(116) Mason, H. E.; Frane, W. L. Du; Walsh, S. D. C.; Dai, Z.; Charnvanichborikarn, S.; Carroll, S. A. *Environ. Sci. Technol.* **2013**, *47*, 1745.

(117) Daval, D.; Sissmann, O.; Menguy, N.; Saldi, G. D.; Guyot, F.; Martinez, I.; Corvisier, J.; Garcia, B.; Machouk, I.; Knauss, K. G.; Hellmann, R. *Chem. Geol.* **2011**, *284*, 193.

(118) Facchini, L.; Fretigny, C.; Tougne, P.; Legrand, a P. *J. Am. Chem. Soc.* **1992**, *114*, 6412.

(119) Brinker, C. J.; Kirkpatrick, R. J.; Tallant, D. R.; Bunker, B. C.; Montez, B. *J. Non. Cryst. Solids* **1988**, *99*, 418.

(120) Jung, H. B.; Um, W. *Appl. Geochemistry* **2013**, *35*, 161.

(121) Kashef-Haghighi, S.; Ghoshal, S. *Ind. Eng. Chem. Res.* **2013**, 5529.

(122) Um, W.; Jung, H. B.; Martin, P. F.; McGrail, B. P. *Effective Permeability Change in Wellbore Cement with Carbon Dioxide Reaction*; 2011.

(123) Newell, D. L.; Carey, J. W. *Environ. Sci. Technol.* **2013**, *47*, 276.

(124) Nebel, H.; Epple, M. *Zeitschrift fur Anorg. und Allg. Chemie* **2008**, *634*, 1439.